Contents

List of Figures

List of Tables

Chapter 1

Introduction

1.1 Background

The n-body problem is a class of problems in physics that, in a highly general sense, consists of modelling the motion of n objects interacting through some physical force. In classical mechanics the equations of motion for n point particles can be derived from Newton's second law of motion, which states that the rate of change in momentum for an object equals the force acting on it, or from analytical formulations such as Lagrangian and Hamiltonian mechanics, which consider scalar properties of motion like kinetic and potential energies. In the non-relativistic quantum regime, where the wave-like property of matter has to be taken into account, the state of an n-body system is described by a total wave function, where the Hamiltonian operator generates the time evolution of the state as given by Schrödinger's differential equation.

The core of the n-body problem is that neither the classical equations of motion nor the Schrödinger equation are analytically solvable for more than two interacting particles. Consider the case where $n = 3$. Although apparently simple, the configuration space for the three-body problem is six dimensional after separating out the center of mass motion. Three additional constants of motion can be provided by conservation of the total angular momentum, which effectively reduces the problem to that of three coupled second order non-linear differential equations in the classical case and a three dimensional Schrödinger equation in the quantum case.

The quest for a general solution to the classical three-body problem is

renowned. As a recurrent muse to a number of great mathematicians during the past centuries, dating back to Newton himself, the three-body problem has been a catalyst for the development of analysis and the modern theory of dynamical systems [1]. Although there are a number of special cases that have explicit solutions, non-linear dynamical systems often display highly unpredictable behaviour due to sensitive dependencies on initial conditions, i.e., are chaotic. Nowadays, different numerical approaches are used to solve these kinds of problems, but the computational load can be substantial.

In contrast to the classical case, the quantum three-body problem is amenable to qualitative analysis [2] and, in some cases, even to analytic solutions. In the quantum realm of few-body systems the Faddeev and the Faddeev-Yakubovsky equations, which are equivalent formulations of the Schrödinger equation for three- and four-body systems respectively, can, for a few special cases, be solved analytically by iteration [3, 4]. For the three-body scattering problem bound state solutions can exist in cases where all three two-body subsystems have short-ranged interactions, if at least two of these interactions are close to resonance. This is called the Efimov effect.

1.2   The Birth of Efimov Physics

In low energy scattering, particles are said to resonate when during the collision they remain close for an extended period of time, in an almost bound state, before separating. This kind of interaction is characterized by an s-wave scattering length that is much larger than the interaction range of the particles.

In 1970, Vitaly Efimov predicted that resonant two-body forces could give rise to a series of bound energy levels in three-particle systems [5]. When the short-ranged two-body forces approached resonance, he found a universal long-range three-body attraction emerging, giving rise to an infinite number of trimer states with binding energies obeying a discrete scaling law at resonance.

Efimov proposed that attractive three-body interaction appearing in systems with resonant short-ranged interactions and repulsive Coulomb forces could explain the binding of three particle nuclei such as the three nucleon triton ^{3}H and the triple-alpha Hoyle state of ^{12}C [5, 6].

The notion of Efimov physics comprises a range of universal phenomena

that occur in few-body systems exhibiting the Efimov effect. Short-ranged forces commonly occur in nature and few-body effects are expected to appear in a broad range of physical systems. Development in the theory of few-body quantum systems is important, since it could bridge the gap between existing well developed models of treating one- and two-body systems and the statistical methods used to describe many-body systems.

1.3 Theoretical Introduction

A short review concerning some important aspects of quantum mechanical systems and two-body scattering, in particlular the concept of *scattering length*, will follow, in order to set the stage for a discussion of quantum effects in few-body systems in general and Efimov states in three-body systems in particular. A more detailed description of two-body scattering will be given in Chapter 3.

1.3.1 Entering the Quantum Realm

All particles of matter exhibit wave-like properties. The wavelength of a particle with momentum p is given by the de Broglie equation

$$\lambda = \frac{h}{p} = \frac{h}{mv} \tag{1.1}$$

where h is the Planck constant. The wave characteristics of matter grow with increasing de Broglie wavelength. When the wavelength is sufficently large, classical physics no longer applies and the system has reached the quantum regime. From Eq. (1.1) it is evident that this is true for particles that are very small or very slow. In an ultracold quantum gas, the atoms are cooled down to a point where they move so slowly that the increased uncertainty in position for the individual atoms becomes so large that they start to overlap with each other. At this point the atoms can not be viewed as individual particles but as a correlated wave. The de Broglie wavelength of the atoms is then larger than the average interatomic spacing, which is typically about one micron in a low density gas, and their behaviour is fully governed by quantum mechanics. In other words, the transition to the quantum regime occurs when the thermal de Broglie wavelength is on the order of the interparticle spacing. Since the temperature of the gas and the

thermal de Broglie wavelength are related through

$$\lambda = \frac{h}{\sqrt{2\pi m k_B T}},\tag{1.2}$$

in which k_B is the Boltzmann constant, it means that there is a critical temperature for when the quantum effects become dominant. For a dilute atomic gas this critical temperature is in the microkelvin to nanokelvin range.

1.3.2 Two-body Interactions

Atomic interactions are, to a good approximation, pair-wise and short ranged, which means that they interact when they are close to each other. At sufficently low energies, atoms behave like point particles and have quantized orbital angular momenta l. In analogy with atomic orbitals, the quantum numbers $l = 0, 1, 2$, associated with an atom, are referred to as s-waves, p-waves and d-waves, respectively.

After separating out the centre-of-mass, the scattering processes of two particles can be expressed in terms of their relative postion only. The relative motion can be decomposed into that of an incoming plane wave, expanded into a sum of partial waves with definite angular momenta, which scatters off a potential placed at the origin. For low energy scattering, only the first few l-quantum numbers contribute to the scattering process and in the ultracold regime s-wave collisions dominate. Scattering becomes isotropic when the wavelength of the relative motion is much larger than the typical interparticle interaction range r_0, since the wave is then too large to resolve the details of the short-range interaction. In other words, the colliding atoms cannot resolve each other's internal structure given by their electron configurations. This makes scattering in the low energy limit indistinguishable from that of point particles provided that the mean distance between the atoms is much larger than the interaction range, which is the case in a low density atomic vapour. Furthermore, only spherical waves will come close enough to be scattered by the potential. Higher partial waves $(l > 0)$ will not "feel" the potential since they will be reflected by a centrifugal barrier at separations greater than the interaction range. Two-body scattering in this regime is solely governed by a single parameter called the s-wave scattering length a. The s-wave scattering length, referred to as 'the scattering length'

from here on, is defined in the low-energy limit as

$$a = \lim_{k \to 0} -\frac{\tan \delta_0(k)}{k}, \qquad (1.3)$$

where k is the wave number ($k = p/\hbar = \sqrt{2\mu_{2b}E}/\hbar$), E is the kinetic energy of the relative motion, μ_{2b} is the two-body reduced mass and $\delta_0(k)$ is the s-wave phase shift of the outgoing wave. For small k, the phase shift will behave as $\delta(k) \approx -ka + O(k^2)$. If scattering by a hard sphere is considered, the scattering length a is simply the radius of the sphere. In the low energy limit, the scattering properties for an arbitrary potential with positive scattering length is the same as that of a hard sphere with radius a. Alkali atoms, however, often have a scattering length with a magnitude that is much larger than the interaction range. Scattering can therefore occur at separations greater than the interaction range if the magnitude of the scattering length is sufficiently large. Consequently, at large separations the scattering length characterizes the effective interparticle interaction when the energy is very low. Since a positive scattering length corresponds to a negative phase shift, i.e., to the scattered wave being pushed out, the effective interaction will be repulsive (Fig. 1.1a). Conversely, a weakly attractive potential will pull in the wave function, corresponding to a negative scattering length and an effective attractive interaction (Fig. 1.1b). However, as I will discuss below, this simple picture becomes more complex if the attractive potential is deep enough to support a bound state. For an attractive potential that cannot support a bound state the scattering length is negative and the effective interaction at large separations is attractive. On the other hand, if the potential can support one, or more, bound states, it is possible to have both positive and negative scattering lengths, thus corresponding to both effective repulsive and effective attractive interactions. If the depth of the underlying attractive two-body potential is increased when a is positive, a will decrease and the outward push of the wave will lessen as the effective repulsion decreases. If the potential is made more attractive when the scattering length is negative, however, the effective interaction will become more attractive, since the increased positive phase shift will cause the scattered wave to be pulled in further.

In the abscence of an interaction, the phase shift is simply zero and the outgoing scattered wave is in phase with the incoming wave. Any interac-
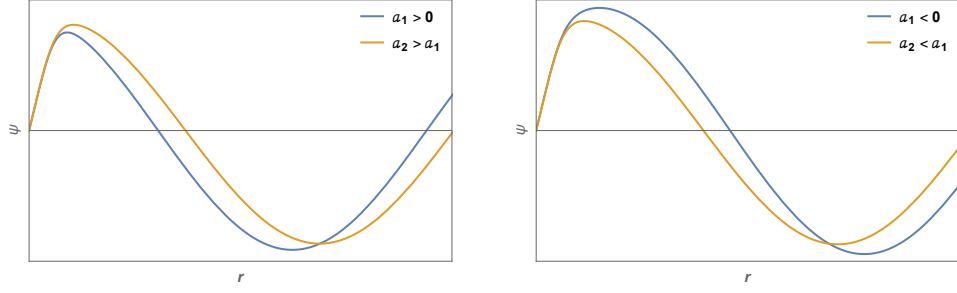
(a) The wave function is pushed outwards when the magnitude of a positive scattering length is increased.

(b) The wave is pulled inwards when the magnitude of a negative scattering length is increased.

Figure 1.1: Illustration of phase shifts causing an effective interaction and how they depend on the sign and magnitude of a.

tion will cause a dephasing between the outgoing and incoming waves. The larger the dephasing is, the larger the effect of the scattering potential on the asymptotic wave will be. The strongest dephasing occurs when δ_0 takes the value $\pi/2$ (mod π), whereupon two-body s-wave resonances are formed and the scattering length, as defined in Eq. (1.3), diverges. At this point a node appears in the inner part of the wavefunction. If the potential depth is increased further, the scattering length becomes $\pm\infty$ and then again decreases until the appearance of another bound state, where it once again diverges. This behaviour is illustrated in Fig. 6.1. The situation when the scattering length diverges is of particular interest in this thesis because Efimov physics arises when the two-body interactions are near resonance. Since the phase shift for the s-wave can be written as $\delta_0 \propto -ka$ in the long wavelength limit ($k \ll r_0^{-1}$), it means that the scattering length a has to become much larger in magnitude than the interaction range r_0 for a two-body interaction to become resonant.

1.3.3   Universality

Particles with large scattering lengths, i.e., $|a| \gg r_0$, in the low-energy regime, have universal properties. The properties are universal in the sense that they depend on the scattering length alone and not on the details of the short-range interaction. Alkali atoms interact via van der Waals potentials of the form $-C_6/r^6$, where the range r_0 typically is on the order of the van

der Waals length, which can be defined by [7]

$$l_{vdW} = \frac{1}{2}\left(\frac{2\mu_{2b}C_6}{\hbar^2}\right)^{1/4}.$$

(1.4)

For a system of two identical bosons with $a > 0$ there is a universal shallow two-body bound state near the scattering threshold, with the binding energy

$$E_D = \frac{\hbar^2}{ma^2}.$$

(1.5)

For $a < 0$ there is no such bound state. Outside the universal range the natural binding energy for two particles should be approximately $\hbar^2/mr_0^2$. The cross section for elastic scattering of two identical bosons in this regime is also universal and so is the mean square radius of the bound molecular state, which are given by

$$\sigma = 8\pi a^2$$

(1.6)

and

$$\langle r^2 \rangle = \frac{a^2}{2},$$

(1.7)

respectively, in zero energy limit. The universal quantities given in Eqs. (1.5) to (1.7) are exact for $a = \pm\infty$ and approximate for $|a| \gg r_0$. The unique dependence on this one length parameter also leads to continuous scaling symmetries in these quantities. If the scattering length is scaled with some real factor λ such that $a \to \lambda a$, the shallow dimer energy will scale as

$$E_D(\lambda a) = \lambda^{-2} E_D(a),$$

(1.8)

while the elastic cross section and the mean square radius scale as

$$\sigma_e(\lambda^{-1}k, \lambda a) = \lambda^2 \sigma_e(k, a)$$

(1.9)

and

$$\langle r^2(\lambda a) \rangle = \lambda^2 \langle r^2(a) \rangle,$$

(1.10)

respectively.

While the scattering length completely governs the low energy two-body

collision problem, it is also the main parameter for describing the interaction of particles at very low collision energies in general.

Similarly to the universal quantities found in the two-body sector, three-body systems can also exhibit universal properties. For particles interacting through short-ranged interactions near resonance, i.e., when the attraction is on the verge on or just barely can support a shallow dimer, corresponding to $|a| = \infty$, an effective long-range three-body attraction emerges, which can form shallow three-body bound states.

To understand how this long-range interaction is formed, consider a collision between the shallow dimer and a third particle in the low energy limit. The third particle will start to "feel" the dimer at a distance close to the magnitude of the two-body scattering length, which is also the size of the dimer. At this point the third particle could tug off any of the particles in the dimer to form a new pair. By flickering back and forth between the two particles, the third particle can mediate an interaction between the two, and even when the interaction is not strong enough to support any bound binary subsystem, it may still support one, or more, trimer states.[1] It is this process of particle exchange that results in the effective three-body interaction that Vitaly Efimov found when he was studying the quantum three-body problem. This effective long-range attraction is universal in the sense that it emerges irrespective of the underlying two-body short-range interactions and, in the resonant limit, it gives rise to an infinite series of bound states, called Efimov trimers.

Two aspects of universality in the three-body sector for three identical bosons are that the size and energy of succesive trimer states in the resonant limit are related by a scale transformation with a universal constant $\lambda = e^{\pi/s_0} \simeq 22.7$, where $s_0 \simeq 1.00624$ is a universal constant of Efimov physics. The continuous scale invariance, which appears in the two-body sector, is therefore not applicable. Instead, the symmetry of the asymptotic Efimov spectrum is characterized by a discrete scale invariance where the size and binding energies each form a geometric progression, where the size of an excited state is larger than the previous state by the factor λ and the binding energies of two consequtive states scale like $E_T^{n+1} = E_T^n \lambda^{-2}$.

---

[1]The binding of three particles, while all three two-body subsystems are unbound, is called Borromean binding. As the name implies, the state falls apart into three free particles if one particle is removed. Similarly to the linking of the Borromean rings, stability of the state is secured by the three when no bound pairs can form [8].
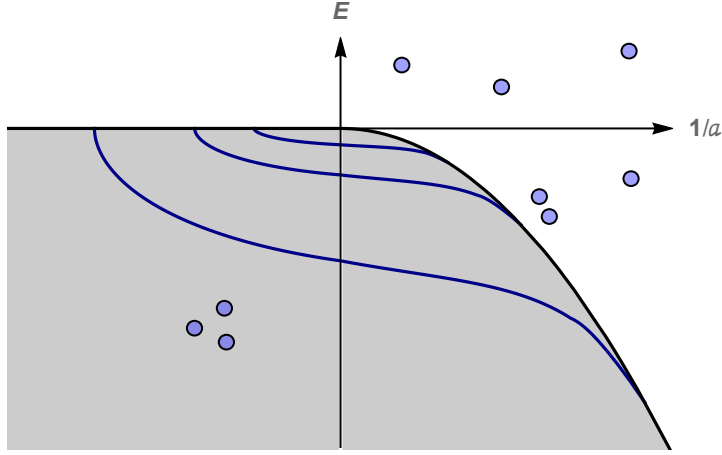
Figure 1.2: The energies of the three first Efimov states are plotted as functions of the inverse scattering length a. Three different regions can be identified in the figure: The three atom continuum is the region above the zero-energy threshold; the atom-dimer region is the region enclosed by the horisontal axis and the atom-dimer threshold (the solid black line); and the trimer region is the region shown in grey, where the Efimov states are represented by the blue lines.

The Efimov scenario is illustrated in Fig. 1.2 where the energies of the three lowest trimers are plotted as functions of $1/a$. Three different regions can be identified in the figure. The region above the zero-energy threshold is the three atom continuum. In grey is the trimer region, where the bound Efimov states are shown schematically by solid blue lines (with a scaling factor set at 1.7 rather than 22.7 for illustrative purposes). On the positive side of $1/a$ the Efimov trimer states merge into the atom-dimer continuum.

The Efimov effect is not limited to systems of identical bosons and can, in fact, appear in a variety of systems, such as in systems of bosonic unequal masses and in three component Fermi-Fermi mixtures. However, the universal scaling constant is system dependent and will then assume a different value.

1.4 Thesis Objective

The main purposes of this thesis is to summarize the theory of Efimov physics and the necessary methodology needed for developing a computer code that calculates the effective long-range three-body potentials, which

later can be used to calculate the Efimov energy spectra and three-body wave functions.

1.5   Outline

The thesis is organized as follows: Chapter 2 serves as an introduction to the reader of some of the main expermental findings in the field of Efimov physics; a brief review of the theory of quantum mechanical scattering is given in Chapter 3 with a focus on low energy and zero energy scattering; in Chapter 4 I present the theory of the three body scattering problem and introduce both non-symmetric and symmetric hyperspherical coordinates; Chapter 5 outlines the numerical method used to develope the computer code; in Chapter 6 I describe the scattering model used to test the validity of the code; and in Chapter 7 I present and analyse the results.

Chapter 2

Experimental Evidence

2.1 Efimov Trimers in Atomic Systems

Ultracold atomic clouds provided the first staging ground for exploring Efimov physics and related few-body phenomena due to the ability to control atom-atom interactions near a Feshbach resonance[1] by means of an external magnetic field. In these extremely dilute gases, with number densities n of the order 10^{11}–10^{14} atoms per cubic centimetre [10], the probability for collisions can reach unity by tuning the s-wave scattering length to the unitary regime $n|a^3| \gg 1$. In experiments with trapped ultracold atomic and molecular gases of alkali atoms with tunable two-body interactions, the existence of Efimov trimers have been inferred from resonantly enhanced loss rates for both atomic three-body recombination processes, when the Efimov state couples to the triatomic threshold ($a < 0$), and in atom-dimer relaxation processes ($a > 0$).

Alkali atomic gases   The first observations of an Efimov resonance was reported[2] in 2006 by the Innsbruck group of Grimm et al. in experiments with a trapped ultracold gas of ^{133}Cs. To create a Bose–Einstein condensate they used the magnetically tunable interaction properties of caesium atoms

---

[1]The physical origin of a Feshbach resonance is the coupling of the incident collision state, i.e., the entrance channel, to a bound molecular state, i.e., the closed channel, when the kinetic energy of the colliding atoms approaches the energy of the interatomic potential of the bound state [9].

[2]The actual experiment was performed in 2002 but it took some years before it was realized that this resonantly enhanced loss rate was caused by the formation of an Efimov trimer.

in their energetically lowest state to vary the s-wave scattering length by applying magnetic fields. However, they were troubled by atoms escaping the trap. Atom loss occurs in three atom collisions when two of the atoms form a tightly bound pair because the kinetic energy release due to the pair formation is high enough for both the pair and the free atom to escape the trap. When three free atoms collide and resonantly couple to an Efimov state a fast decay channel into these deeply bound dimer states plus a free atom is formed. The process of pair formation and atoms escaping the trap is therefore resonantly enhanced by the presence of Efimov trimers and it was these kinds of resonantly enhanced loss rates reported in [11] that bore the first evidence for Efimov quantum states.

Later experiments have strengthened the evidence of these elusive trimers and in 2014 observations of the first excited Efimov state in an ultracold sample of caesium atoms confirmed the theoretically predicted universal scaling properties of two succesive Efimov states [12].

Efimov resonances in homogenous gases composed of a variety of atomic species have been observed, including ^{85}Rb [13], ^{39}K [14], ^{7}Li [15] and in three component Fermi gases of ^{6}Li [16]. Efimov physics have been extended to involve heteronuclear states and resonances have been reported in, for example, heterogenous mixtures of Li-Cs and Li-Rb [17, 18].

Helium trimers   Clusters of helium atoms ^{4}He$_3$ were early on identified as a prime candidate for studying Efimov physics in a natural system because of the unique interaction properties of the diatomic helium potential [19]. The inherent nonpolarizability of helium atoms due to their electron configuration causes an especially weak van der Waals attraction in the helium dimer ^{4}He$_2$, a fact that is manifested by a very shallow potential with a naturally large positive s-wave scattering length supporting only one unusually large state with an extremely low binding energy [20]. Theoretical calculations using the helium potential had predicted the existence of two consecutive Efimov states in the first and second excited state of the helium trimer [21].

The first experimental evidence of the existence of the Efimov state in the helium trimer was reported in 2015 [22]. By using Coulomb explosion imaging of mass-selected clusters by means of matter wave diffraction, the group of Kunitski et al. was able to image the structure of ^{4}He$_3$ and ^{3}He ^{4}He$_2$

clusters, which confirmed the Efimov characteristics of not only the first, but also the second excited ^{4}He trimer.

2.2 Efimov States in Nuclei

The Efimov quantum effect was originally predicted to exist in the nuclei of tritium and in the Hoyle state[3] of ^{12}C because of the resonant character of nucleon-nucleon forces, which give rise to naturally large s-wave scattering lengths with nucleon-nucleon s-wave scattering lengths for the spin-triplet and the spin-singlet channel being 3 and 15 times the range of the nuclear forces [5, 6]. However, these states have not yet been observed experimentally.

2.3 Four-body Recombination Connected to Efimov Trimers

The Efimov scenario is even richer. In connection to an Efimov trimer, a pair of four-body states can form when a fourth atom approaches. In accordance with the theoretical predictions, strong evidence for the existence of a pair of four-body states was provided in 2009 [23].

---

[3]The Hoyle state is the second excited state in ^{12}C, which is formed in two steps in the 3α process where two α-particles first react to form ^{8}Be, which subsequently reacts with a third α-particle to form ^{12}C. This state is a resonance to the $\alpha + {}^8$Be channel, meaning that its energy is close to the breakup threshold and that it almost always decays back into its constituent parts of three α-particles. However, very rarely they instead relax into the stable ground state configuration of ^{12}C.

Chapter 3

Scattering Theory

3.1 Two-body Scattering

A collision between a pair of particles can be described in their centre-of-mass frame as the scattering of a particle with reduced mass μ_{2b} ($\mu_{2b} = m_1 m_2/(m_1 + m_2)$) by the potential $V(\mathbf{r})$. The time-independent Schrödinger equation for the relative motion is then given by

$$\left[-\frac{\hbar^2}{2\mu}\nabla^2 + V(\mathbf{r}) \right]\psi(\mathbf{r}) = \frac{\hbar^2 k^2}{2\mu}\psi(\mathbf{r}), \qquad (3.1)$$

where $\mathbf{r}$ denotes the interparticle separation and ∇^2 the Laplace operator, which in spherical coordinates reads

$$\nabla^2 = \frac{1}{r^2}\frac{\partial}{\partial r}\left(r^2 \frac{\partial}{\partial r}\right) + \frac{1}{r^2 \sin\theta}\frac{\partial}{\partial\theta}\left(\sin\theta\frac{\partial}{\partial\theta}\right) + \frac{1}{r^2 \sin^2\theta}\frac{\partial^2}{\partial\phi^2}. \qquad (3.2)$$

By requiring the potential to be zero at large interparticle separation, the collision can be described as that of an incident plane wave with definite angular momentum that scatters off a potential placed at the origin. The potential will deflect some of the incident waves to form scattered waves, which at large distances will be diverging from a point source in the scattering region. Let r_0 denote the range of the action of the potential and let z denote the direction of the propagation of the incident plane wave. The boundary condition at large separations $r \gg r_0$ then imposes a solution of the following asymptotic form

$$\psi(\mathbf{r}) \xrightarrow{r\to\infty} e^{ikz} + f(k,\theta,\phi)\frac{e^{ikr}}{r}, \tag{3.3}$$

in which the total wave function is written as a superposition of the incident and scattered wave, with a scattering amplitude $f(k,\theta,\phi)$ that depends on the energy of the particle through k, the deflection angle θ between the waves and the azimuthal angle ϕ about the z-axis. For spherically symmetric potentials, i.e., $V(\mathbf{r}) = V(r)$, the Schrödinger equation (3.1) is separable. The incident and scattered wave functions are then conveniently expanded on a basis set of eigenfunctions of $\mathbf{L}^2$ and L_z, where $\mathbf{L}$ is the relative orbital angular momentum operator. These eigenfunctions are the spherical harmonic functions $Y_l^m(\theta,\phi)$, which satisfy

$$\mathbf{L}^2 Y_l^m(\theta,\phi) \equiv -\frac{1}{\sin^2\theta}\left[\sin\theta\frac{\partial}{\partial\theta}\left(\sin\theta\frac{\partial}{\partial\theta}\right) + \frac{\partial^2}{\partial\phi^2}\right]Y_l^m(\theta,\phi) = l(l+1)Y_l^m(\theta,\phi). \tag{3.4}$$

The most general solution to Eq. (3.1) is then of the form

$$\psi(\mathbf{r}) = \sum_{l=0}^{\infty}\sum_{m=-l}^{l} C_{lm}\frac{u_l(r)}{r}Y_l^m(\theta,\phi). \tag{3.5}$$

The separability of $\psi(\mathbf{r})$ effectively reduces the problem to that of solving the radial equation

$$\left[-\frac{d^2}{dr^2} + \frac{l(l+1)}{r^2} + \frac{2\mu}{\hbar^2}V(r) - k^2\right]u_l(r) = 0. \tag{3.6}$$

By requiring the wave function to be finite everywhere it is implied that $u_l(r)$ must vanish at the origin. In the case where $V(r) = 0$, the solutions to the radial equation for positive energies have the form

$$u_l(r) \propto rj_l(kr), \tag{3.7}$$

where $j_l(kr)$ are the spherical Bessel functions. In the case of a non-zero potential the solutions need to be regular at the origin, while at large distances $r \gg r_0$ they have the form

$$u_l(r) = r(a_l j_l(kr) + b_l y_l(kr)), \tag{3.8}$$

where $y_l(kr)$ are the spherical Neumann functions. Asymptotically the solutions Eq. (3.8) behave like

$$u_l(r) \xrightarrow{r\to\infty} \frac{1}{k}\left(a_l \sin(kr - l\frac{\pi}{2}) - b_l \cos(kr - l\frac{\pi}{2})\right). \qquad (3.9)$$

By defining the ratio of the coefficients as

$$\frac{b_l}{a_l} = -\tan\delta_l(k), \qquad (3.10)$$

where $\delta_l(k)$ is an energy dependent phase shift, the normalized asymptotic radial solutions for a non-vanishing potential can be written

$$\begin{aligned}
u_l(r) \xrightarrow{r\to\infty} &\frac{1}{k}\left(\sin(kr - l\frac{\pi}{2} + \delta_l(k))\right) \\
&= \frac{e^{-i\delta_l(k)}}{2ik}\left((-1)^{l+1}e^{-ikr} + e^{2i\delta_l(k)}e^{ikr}\right).
\end{aligned} \qquad (3.11)$$

Since the incident plane wave in Eq. (3.3) is aligned with the z-axis, it is an eigenfunction of L_z with an eigenvalue $m = 0$. The plane wave expansion is thus independent of the azimuthal angle around the z-axis and can therefore be expressed as

$$e^{ikz} = \sum_{l=0}^{\infty}(2l + 1)i^l j_l(kr)P_l(\cos\theta), \qquad (3.12)$$

where $P_l(\cos\theta)$ are the Legendre polynomials. It is evident that this plane wave is a solution to Eq. (3.1) for $V(r) = 0$, and in the asymptotic limit these solutions behave like

$$e^{ikz} \xrightarrow{r\to\infty} \frac{1}{2ikr}\sum_{l=0}^{\infty}(2l + 1)P_l(\cos\theta)\left((-1)^{l+1}e^{-ikr} + e^{ikr}\right). \qquad (3.13)$$

The incident plane wave can thus be resolved into that of incoming (e^{-ikr}) and outgoing (e^{ikr}) spherical waves with a relative phase of 0 for l with odd parity and of π otherwise. Substituting Eq. (3.13) into Eq. (3.3) results in an asymptotic wave function of the form

$$\psi(\mathbf{r}) \xrightarrow{r\to\infty} \frac{1}{2ikr} \sum_{l=0}^{\infty} (2l+1) P_l(\cos\theta) \big((-1)^{l+1} e^{-ikr} + e^{ikr}\big) + f(k,\theta) \frac{e^{ikr}}{r},$$

$$(3.14)$$

where the scattering amplitude $f(k,\theta,\phi) = f(k,\theta)$ because the scattering potential is spherically symmetric. Since the system is rotationally invariant about the z-axis, the scattered wave function must be azimuthally symmetric, i.e., have a magnetic quantum number $m = 0$, wherefore the general solution to Eq. (3.5) becomes

$$\psi(\mathbf{r}) = \sum_{l=0}^{\infty} c_l \frac{u_l(r)}{r} P_l(\cos\theta), \qquad (3.15)$$

in which c_l are unknown coefficients. The asymptotic behaviour of (3.15) is thus

$$\psi(\mathbf{r}) \xrightarrow{r\to\infty} \frac{1}{2ikr} \sum_{l=0}^{\infty} c_l P_l(\cos\theta) e^{-i\delta_l(k)} \big((-1)^{l+1} e^{-ikr} + e^{2i\delta_l(k)} e^{ikr}\big). \quad (3.16)$$

By comparing the asymptotic form of the incoming waves expressed in Eqs. (3.14) and (3.16) it is evident that the coefficents $c_l = (2l+1) e^{i\delta_l(k)}$, and the asymptotic scattered wave is therefore given by

$$\psi(\mathbf{r}) \xrightarrow{r\to\infty} \frac{1}{2ikr} \sum_{l=0}^{\infty} (2l+1) P_l(\cos\theta) \big((-1)^{l+1} e^{-ikr} + e^{2i\delta_l(k)} e^{ikr}\big). \quad (3.17)$$

For elastic scattering the flux of incoming and outgoing waves is conserved. The presence of a scattering potential will modify the plane wave by changing the relative phase of the incoming and outgoing waves by a phase shift $\delta_l(k)$ for each partial wave with angular momentum l. The phase shift $\delta_l(k)$ is thus a measure of the distortion of $u_l(r)$ from the free solution due to the presence of a scattering potential. Depending on whether the potential is attractive or repulsive, the scattered wave will either be pulled in or pushed out, respectively, by the scatterer. The scattering amplitude $f(k,\theta)$ is determined by comparing the outgoing waves in Eqs. (3.14) and (3.17), resluting in

$$f(k, \theta) = \sum_{l=0}^{\infty} (2l + 1) f_l(k) P_l(\cos \theta), \tag{3.18}$$

where the partial amplitude f_l can be expressed in the following ways

$$f_l(k) = \frac{e^{2i\delta_l(k)} - 1}{2ik} = \frac{e^{i\delta_l(k)} \sin \delta_l(k)}{k} = \frac{1}{k \cot \delta_l(k) - ik}. \tag{3.19}$$

The differential and the total cross-sections are determined from the scattering amplitude through

$$\frac{d\sigma}{d\Omega} = |f(k, \theta)|^2, \tag{3.20}$$

and

$$\sigma(k) = \sum_{l=0}^{\infty} \sigma_l(k) = \frac{4\pi}{k^2} \sum_{l=0}^{\infty} (2l + 1) \sin^2 \delta_l(k), \tag{3.21}$$

in which σ_l is the scattering cross-section for each partial wave. So far, we have assumed that the particles are distinguishable and that scattering in the direction θ could be discriminated from that of scattering in the direction $\pi - \theta$. However, for identical particles these collisional processes will lead to the same final state. Interchaning the spatial coordinates of the particles $\mathbf{r}_1 \leftrightarrow \mathbf{r}_2$ corresponds to replacing the relative position vector $\mathbf{r}$ by $-\mathbf{r}$, which in polar coordinates corresponds to replacing (r, θ, ϕ) by $(r, \pi - \theta, \phi + \pi)$. Thus, to accurately describe scattering of identical particles the quantum statistics of the particles must be taken into account to assure that the wave function of the total system has the correct symmetry properties. The wave function given in Eq. (3.3) does, however, not fulfill this requirement. Instead, the correct two-body wave function in the centre-of-mass frame for indistinguishable particles is retrieved by symmetrization (bosons, $\epsilon = 1$) or antisymmetrization (fermions, $\epsilon = -1$), leading to

$$\psi(\mathbf{r}) \xrightarrow{r \to \infty} \frac{e^{ikz} + \epsilon e^{-ikz}}{\sqrt{2}} + \frac{f(k, \theta) + \epsilon f(k, (\pi - \theta))}{\sqrt{2}} \frac{e^{ikr}}{r}. \tag{3.22}$$

In classical mechanics, the differential cross-sections for the two processes described above would simply add up. However, the quantum mechanical

differential cross-section for indistinguishable particles is given by

$$\frac{d\sigma}{d\Omega} = |f(k,\theta) + \epsilon f(k,(\pi-\theta))|^2, \quad \text{for} \quad 0 \le \theta \le \frac{\pi}{2}, \qquad (3.23)$$

where the sum of probability amplitudes is

$$f(k,\theta) \pm f(k,(\pi-\theta)) = \frac{1}{2ik}\sum_{l=0}^{\infty}\left[1 \pm (-1)^l\right](2l+1)P_l(\cos\theta)(e^{2i\delta_l(k)}-1).$$
$$(3.24)$$

Note that the total cross-section is obtained by integrating over half of the solid angle $\Omega = 4\pi$ in the case of identical particles. The expression for the total cross-section for elastic scattering after integration is then

$$\sigma(k) = \frac{8\pi}{k^2}\sum_{l=0}^{\infty}(2l+1)\sin^2\delta_l(k). \qquad (3.25)$$

In the case of bosons, only even values of l, and in the case of fermions, only odd values of l, will contribute to the total cross-section (3.25).

3.2   The Low Energy Limit

At very low energies, i.e., when the angular de Broglie wavelength $\lambda = 1/k$ is much larger than the interparticle interaction range $kr_0 \ll 1$, higher partial waves become unimportant except for potentials that are strong enough to form $l \ne 0$ bound states near the threshold ($E \simeq 0$). This can be understood classically by considering that particles with angular momentum l and energies much lower than the height of the centrifugal barrier, i.e., the angular momentum term in the effective potential $V_{eff} = V(r) + \hbar^2 l(l+1)/2\mu r^2$, will simply be reflected by the barrier and only the lowest partial wave $l = 0$ will be able to come close enough to be scattered by the potential $V(r)$. For short-ranged two-body interactions, i.e., potentials that fall off faster than r^{-2}, the angular momentum term is the potential of the longest range and will thus largely govern the threshold behaviour ($E = 0$) of the radial wave function. Since the potential and the k^2 term can be neglected in the radial equation (3.6) for separations larger than the interaction range $r \gg r_0$, the general solution $R_l = u_l/r$ at threshold is given by

$$R_l(E = 0) = c_1 r^l + c_2 r^{-(l+1)}. \tag{3.26}$$

By joining this solution to the asymptotic solution for $E > 0$, given in Eq. (3.11) one can show that

$$\tan \delta_l(k) \simeq \delta_l(k) = \frac{c_2}{c_1} \frac{k^{2l+1}}{(2l-1)!!(2l+1)!!} = (-a_l k)^{2l+1}, \tag{3.27}$$

in which a_l is the scattering length for the lth partial wave. The arguments above form the basis of the Wigner threshold law [24, 25], which states that at near threshold, the phase shift goes to zero like

$$\delta_l(k) \propto k^{2l+1} \pmod{\pi} \quad \text{when} \quad k \to 0. \tag{3.28}$$

The cross-section for that partial wave then approaches zero like

$$\sigma_{l\neq 0}(k) = \frac{8\pi}{k^2}(2l+1)\sin^2 \delta_l(k) \propto k^{4l} \quad \text{when} \quad k \to 0, \tag{3.29}$$

wherefore s-wave scattering is dominant for short-ranged potentials in the low energy limit. The only non-zero cross-section is the one for the s-wave, which, using Eq. (3.19), is given by

$$\sigma = \sigma_0 = 8\pi \lim_{k \to 0} \left| \frac{1}{k \cot \delta_0 - ik} \right|^2 = 8\pi a^2, \tag{3.30}$$

in the case of identical bosons ($\sigma = 4\pi a^2$ for distinguishable particles) and where a is the s-wave scattering length, previously defined in Eq. (1.3).

3.2.1 Zero-energy Scattering

In the ultracold regime the energy is extremely low and $k \simeq 0$. The radial equation simplifies to

$$-\frac{d^2 u_l(r)}{dr^2} + \frac{2\mu}{\hbar^2} V(r) u_l(r) = 0. \tag{3.31}$$

The asymptotic solution for $l = 0$ ($u = u_0$) is then

$$u(r) \xrightarrow{r \to \infty} \frac{1}{k} \sin\left[k\left(r + \frac{\delta_0}{k}\right)\right] \xrightarrow{k \to 0} \text{constant}(r - a). \tag{3.32}$$

The logarithmic derivative is given by

$$\frac{u'(r)}{u(r)} \xrightarrow{r\to\infty} k\cot\left[k\left(r+\frac{\delta_0}{k}\right)\right] \xrightarrow{k\to 0} \frac{1}{r-a}. \tag{3.33}$$

In the limit $kr \ll 1$, the scattering length is obtained as

$$a = -\lim_{k\to 0}\frac{\tan\delta_0}{k} = \lim_{k,r\to 0,\infty}\left(r - \frac{u(r)}{u'(r)}\right). \tag{3.34}$$

From Eq. (3.32) it is evident that the scattering length is simply the radius at which the tangent to the radial wave intercepts the r-axis. This concept can be illustrated by using a short-ranged attractive model potential given by

$$V(r) = -\frac{c_w\left[1 - \left(1+\frac{r^2}{r_c^2}\right)e^{-\frac{r^2}{r_c^2}}\right]}{r^6}, \tag{3.35}$$

in which r_c and c_w are tuning parameters for the distance to the nadir and the depth of the potential, respectively. The scattering length can be varied by fine-tuning the potential depth, see Fig. 3.2. Starting with an attractive potential with negative scattering length, i.e., with a tangent intercept on the negative side, when increasing the potential depth, the magnitude of the scattering length will increase and as $a \to -\infty$ the radial wave function will become flat. A further increase in potential depth will cause a to change sign $a \to \infty$. The sign shift of a is associated with the forming of a bound state. After the change in sign, a further increase in depth will instead correspond to decreasing a since the radial wave function now crosses the r-axis on the positive side, with the intercept subsequently approaching the origin, see Fig. 3.1. This behaviour is then repeated in the same way until a new bound state is formed, see Fig. 3.3.

Positive scattering lengths thus correspond to repulsive effective interactions, which means that the interaction can appear repulsive even in the case of an underlying attractive two-body interaction.
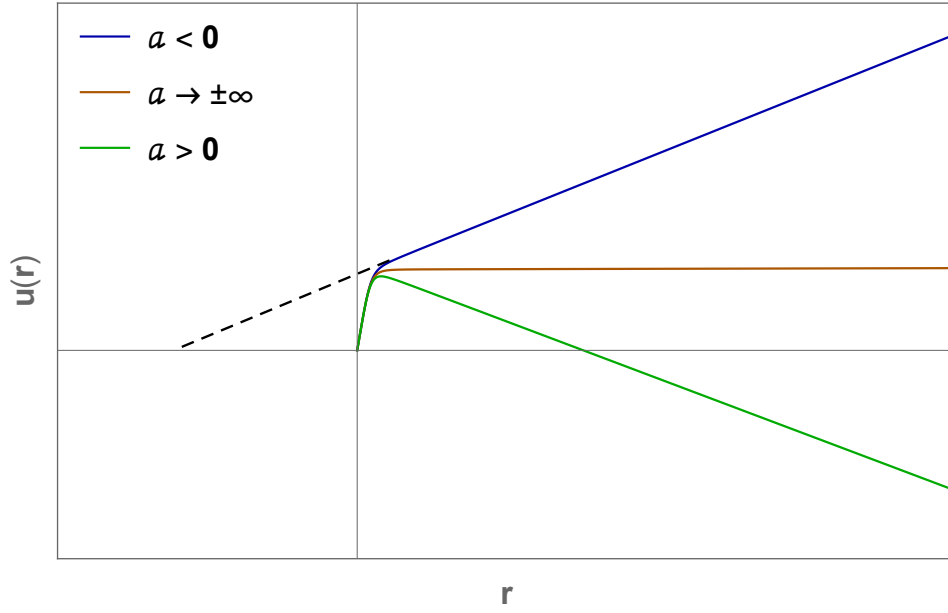
Figure 3.1: Plot of $u(r)$ versus r for the model potential (3.35) at three different depths. The radius at which the tangent intercepts the r-axis gives the value of a.
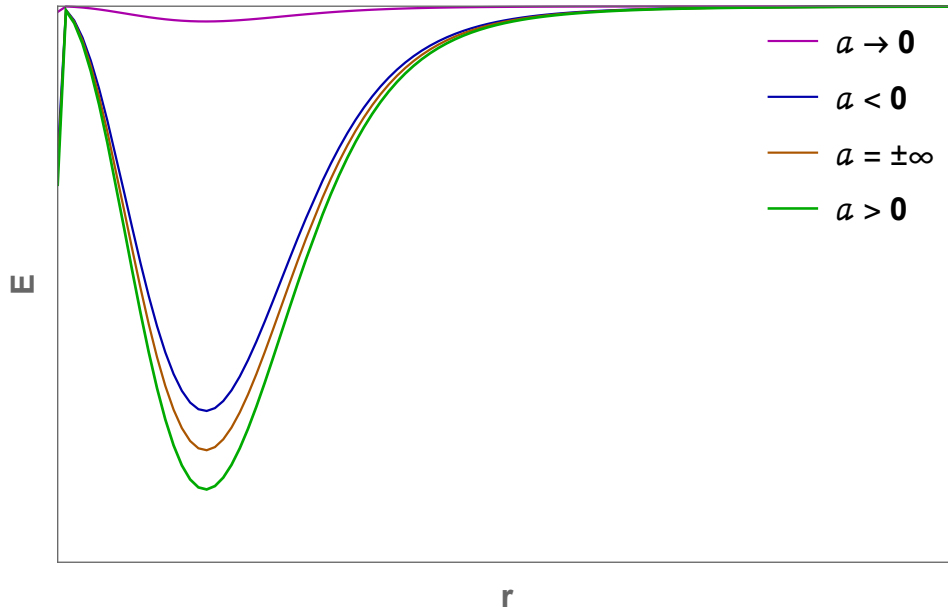
Figure 3.2: The three lowest curves correspond to the potentials used in Fig. 3.1. As the magnitude of a negative a increases, the potential becomes more attractive until it reaches a constant depth at $a = \pm\infty$. After the change in sign, a further increase of a will instead have a repulsive effect on the interaction.
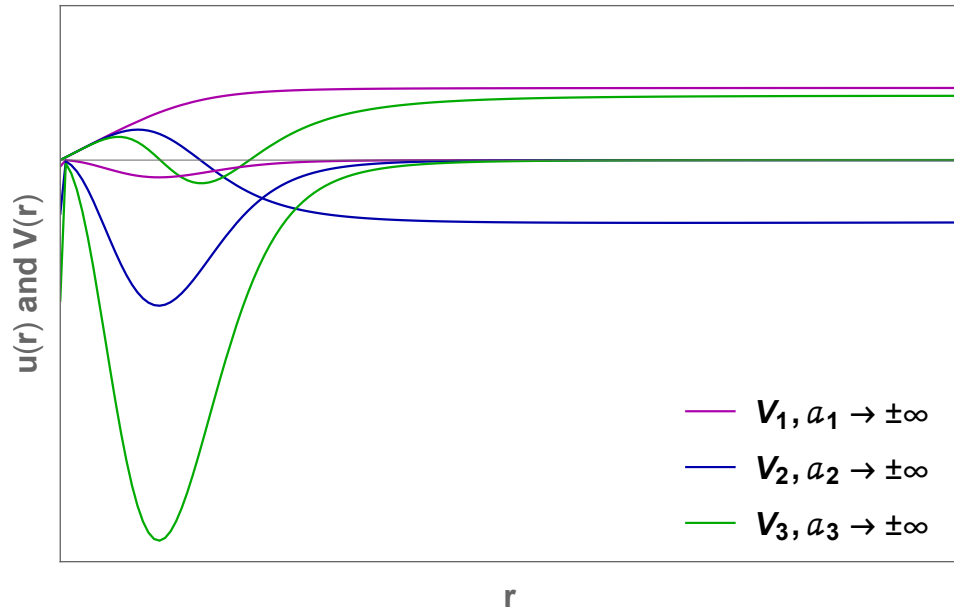
Figure 3.3: Illustration of three potentials and their coorsponding radial wave functions.

Chapter 4

The Three-body Problem

Two-body scattering processes basically concern two different situations, elastic and inelastic collisions. For the three-body problem, solving the three-body Schrödinger equation is more involved. The enhanced complexity is mainly due to the increased number of fragmentation channels in the scattering processes. In addition to the triatomic fragmentation channel (1+1+1), there are three possible atom-dimer fragmenation channels (1+2). This makes the construction of permutation-symmetric wavefunctions highly non-trivial.

There are different routes for solving the three-body problem and they involve either solving the three-body Schrödinger equation or solving the corresponding set of three Faddeev equations. Irrespective of the specific method of choice for solving the three-body system, most approaches start with the same steps. These include separating out the centre-of-mass motion and then defining a set of relative coordinates. A convenient choice for the three-body problem is mass normalized Jacobi coordinates, since this removes the mass factors in the kinetic energy operator. Introducing hyperspherical coordinates in combination with an adiabatic representation is then used to reduce the problem of three colliding atoms to dynamics on a set of coupled adiabatic hyperspherical potentials.

Atomic units[1] (a.u.) will be used in the following chapters.

---

[1] There are four fundamental atomic units – the electron rest mass m_e, the elementary charge e, the reduced Planck's constant $\hbar$, and the Coulomb force constant k_e – whose numerical values are unity by definition, i.e. $m_e = e = \hbar = k_e = 1$. Derived atomic units include dimensions of length and energy, which are expressed in terms of the Bohr radius a_0 and the Hartree E_h.

4.1   Mass Normalized Jacobi Coordinates

The spatial position of three particles in $\mathbb{R}^3$ is fixed by nine coordinates x^i_α, where $i(= 1, 2, 3)$ labels the particles, and $\alpha(= 1, 2, 3)$ their Cartesian space coordinates. Let $\mathbf{x}_i$ and m_i be the position vector and mass of the ith particle in the laboratory frame. If the total mass M, the three particle reduced mass μ, and the normalizing constants d_k $(k = 1, 2, 3)$ are defined by

$$M = \sum_{i=1}^{3} m_i, \tag{4.1}$$

$$\mu^2 = \frac{1}{M} \prod_{i=1}^{3} m_i, \tag{4.2}$$

$$d_k^2 = \frac{m_k}{\mu} \frac{(m_i + m_j)}{M}, \tag{4.3}$$

then a set of mass scaled Jacobi coordinates and the centre-of-mass coordinate can be defined as

$$\mathbf{r}_k = d_k^{-1}(\mathbf{x}_j - \mathbf{x}_i), \tag{4.4}$$

$$\mathbf{R}_k = d_k \left[\mathbf{x}_k - \frac{(m_i \mathbf{x}_i + m_j \mathbf{x}_j)}{m_i + m_j} \right], \tag{4.5}$$

$$\mathbf{X}_{cm} = \frac{1}{M} \sum_{i=1}^{3} m_i \mathbf{x}_i, \tag{4.6}$$

in which the indices i, j, k are cyclic permutations of $(1, 2, 3)$, $\mathbf{r}_k$ is the scaled vector from particle i to j, and $\mathbf{R}_k$ is the scaled vector from the centre-of-mass of the pair ij to particle k, see Fig. 4.1. The kinetic energy operator for the three particles in the laboratory frame, as given by

$$T = -\frac{1}{2} \sum_{i=1}^{3} m_i^{-1} \nabla^2_{\mathbf{x}_i}, \tag{4.7}$$

will then subsequently transform into

$$T = -\frac{1}{2\mu} \left(\nabla^2_{\mathbf{r}_k} + \nabla^2_{\mathbf{R}_k} \right) - \frac{1}{2M} \nabla^2_{\mathbf{X}_{cm}}. \tag{4.8}$$
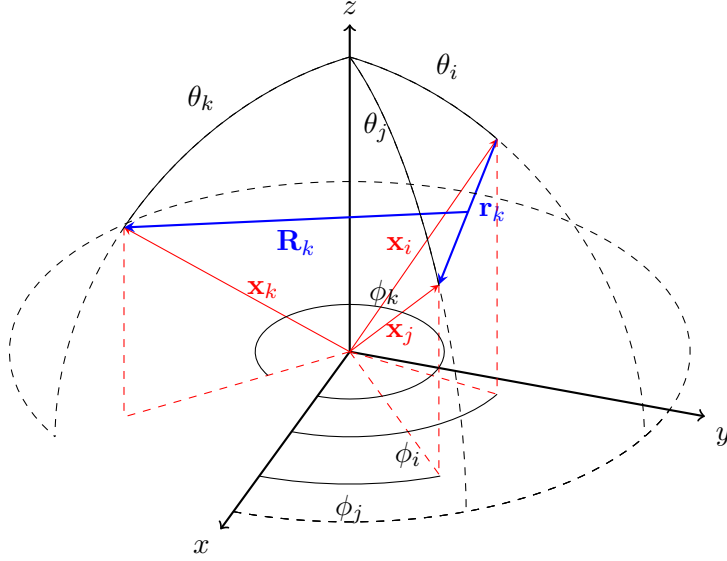
Figure 4.1: Spatial positions of three particles.

Now, since the interaction $V(\mathbf{r}_k, \mathbf{R}_k)$ does not depend on $\mathbf{X}_{cm}$, the centre-of-mass motion decouples from the internal motion in the Schrödinger equation if we write the wavefunction as

$$\Psi(\mathbf{r}_k, \mathbf{R}_k, \mathbf{X}_{cm}) = \varphi(\mathbf{X}_{cm})\psi(\mathbf{r}_k, \mathbf{R}_k), \tag{4.9}$$

so that

$$(H_{cm} + H_{int})\varphi_k(\mathbf{X}_{cm})\psi_n(\mathbf{r}_k, \mathbf{R}_k) = (E_k^{cm} + E_n^{int})\varphi_k(\mathbf{X}_{cm})\psi_n(\mathbf{r}_k, \mathbf{R}_k). \tag{4.10}$$

Henceforth, we will only consider the internal motion part of the Schrödinger equation. To clarify the notations, from now on wavefunctions and energies labelled Ψ and E refer to the internal eigenstates and eigenenergies, which were labelled ψ and E^{int} previously.

There are three possible ways to construct the Jacobi coordinates described above, see Fig. 4.2. Each set transforms into one of the other sets by the exchange of particles. To be able to describe permutations in a system with mass-scaled coordinates it is useful to introduce angles defined by the particle masses [26]. If an even permutation (ijk) of the set (123) is
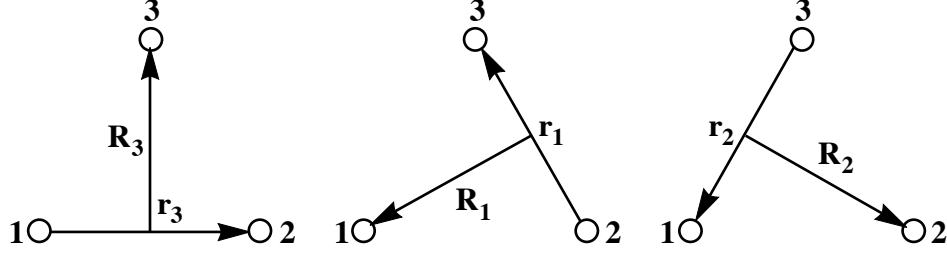
Figure 4.2: Illustration of the three different Jacobi coordinate sets.

considered, then the obtuse angle β_{ij} has the properties

$$\beta_{ij} = -\beta_{ji}, \quad \beta_{ii} = 0, \tag{4.11a}$$

$$\tan \beta_{ij} = -m_k/\mu, \tag{4.11b}$$

$$d_i d_j \sin \beta_{ij} = 1, \tag{4.11c}$$

$$d_i d_j m_k \cos \beta_{ij} = -\mu, \tag{4.11d}$$

$$\beta_{12} + \beta_{23} + \beta_{31} = 2\pi. \tag{4.11e}$$

Orthogonal transformations within the coordinate set are then given by

$$\begin{pmatrix} \mathbf{r}_j \\ \mathbf{R}_j \end{pmatrix} = \begin{pmatrix} \cos \beta_{ij} & \sin \beta_{ij} \\ -\sin \beta_{ij} & \cos \beta_{ij} \end{pmatrix} \begin{pmatrix} \mathbf{r}_i \\ \mathbf{R}_i \end{pmatrix}. \tag{4.12}$$

4.2   The Hyperspherical Method

The next common step in the theoretical framework to describe systems of three particles is to introduce hyperspherical coordinates. The components of the two vectors $\mathbf{r}$ and $\mathbf{R}$ are combined into a single, six-dimensional position vector $\mathbf{q}$. The components of this vector can be regarded as the cartesian components of a point in $\mathbb{R}^6$. The motion of a three particle system is thus equivalent to the motion of a single particle, with the reduced mass μ, in six-dimensional Euclidean space. The polar coordinates of this point particle are given by one hyperradial coordinate ρ, and five hyperangular coordinates, collectively labelled Ω. Three of these angles α, β, γ are usually chosen as the Euler angles that specify the orientation of the body-fixed axis system – i.e. the triangle formed by the three particles – relative to a space-

fixed coordinate frame. These are the external coordinates of the system. The internal coordinates are the hyperradius, which describes the overall size of the system, and the remaining two hyperangles, which describe the shape of the triangle formed by the three particles.

Hyperspherical coordinates are useful for describing fragmentation problems. Fragmentation processes of the system into any one of the possible channels are described by the hyperradius becoming very large ($\rho \to \infty$), while the hyperangles distinguish between the different fragmentation channels. The hyperradius is invariant under both rotations and particle permutations, and for the three-body problem it is defined by

$$\rho = \left(\mathbf{r}^2 + \mathbf{R}^2 \right)^{1/2}, \quad 0 \leq \rho < \infty. \tag{4.13}$$

In contrast to the hyperradius there is no unique way to define the hyperangles and the various definitions are not in general invariant under particle permutations. The most common choises of parametrizing the hypersphere fall into two distinct categories: Delves coordinates, and (democratic) Smith-Whitten coordinates. A brief overview of these coordinates is given in Sections 4.4.1 and 4.4.2 and a more thorough description can be found in Appendices A.1 and A.2.

Independent of the specific choise of hyperangular coordinates, after scaling the total wave function by a factor $\rho^{5/2}$ the three-body Schrödinger equation in terms of general hyperspherical coordinates is written

$$\left(-\frac{1}{2\mu}\frac{\partial^2}{\partial\rho^2} + \frac{\Lambda^2 + \frac{15}{4}}{2\mu\rho^2} + V(\rho, \Omega) \right) \psi(\rho, \Omega) = E\psi(\rho, \Omega), \tag{4.14}$$

where Λ is the grand angular momentum operator, which is an operator in terms of the hyperangles only, and hence take different forms depending on the choice of these angles.

4.3   The Adiabatic Hyperspherical Representation

The first step in solving Eq. (4.14) is to introduce the adiabatic representation. This means expanding the solution $\psi_n(\rho, \Omega)$ into a complete set of orthonormal channel functions $\Phi_\nu(\rho; \Omega)$ that depend parametrically on ρ, with the radial wavefunctions $F_{\nu n}(\rho)$ as expansion coefficients. The hyper-

radius is treated as an adiabatic variable and the channel functions Φ_ν are eigenfunctions to the adiabatic equation

$$H_{ad}\Phi_\nu(\rho;\Omega) = U_\nu(\rho)\Phi_\nu(\rho;\Omega), \qquad (4.15)$$

where the eigenvalues $U_\nu(\rho)$ are the resulting effective potential curves obtained by solving this eigenvalue equation at a number of different hyper-radii, and H_{ad} is the adiabatic Hamiltonian given by

$$H_{ad} = \frac{\Lambda^2 + \frac{15}{4}}{2\mu\rho^2} + V(\rho,\Omega). \qquad (4.16)$$

The adiabatic hyperspherical potentials U_ν contain most of the three-body physics and can be regarded as the three-body equivalent to the Born-Oppenheimer potential in the two-body problem. The zero potential, $V(\rho,\Omega) = 0$, eigenfunctions Φ_ν of Eq. (4.15) for three identical bosons are the Gegenbauer polynomials with eigenvalues

$$U(\rho) = \frac{\lambda(\lambda+4) + \frac{15}{4}}{2\mu\rho^2}, \qquad (4.17)$$

where $\lambda = 0, 4, 6, \ldots$ [27].

The total wave function

$$\psi_n(\rho,\Omega) = \sum_{\nu=0}^{\infty} F_{n\nu}(\rho)\Phi_\nu(\rho;\Omega), \qquad (4.18)$$

can thus be represented in terms of adiabatic states, which, in principle, yields an exact representation of the three-body Schrödinger equation if all couplings are included. The power of this method is that the problem can be reduced to a system of coupled ordinary differential equations for which the major effort lies in solving the adiabatic equation. Substituting Eq. (4.18) into Eq. (4.14) and projecting out $\Phi_{\nu'}$ by multiplying the conjugate transpose $\Phi_\nu^\dagger$ to the left and integrating over the hyperangular coordinates results in an infinite set of coupled differential equations in ρ, which reads

$$\left(-\frac{1}{2\mu}\frac{\partial^2}{\partial\rho^2} + U_\mu(\rho) - \frac{1}{2\mu}Q_{\mu\mu}(\rho)\right)F_{n\mu}(\rho)$$
$$-\frac{1}{2\mu}\left(\sum_{\nu\neq\mu}2P_{\mu\nu}(\rho)\frac{\partial}{\partial\rho} + Q_{\mu\nu}(\rho)\right)F_{n\nu}(\rho) = E_n F_{n\mu}(\rho), \qquad (4.19)$$

where $P_{\mu\nu}$ and $Q_{\mu\nu}$ are the nonadiabatic coupling terms. They involve partial first and second order derivatives of the channel functions with respect to ρ and account for inelastic transitions. The nonadiabatic coupling terms are generated by the ρ dependence on the channel functions and are defined as

$$P_{\mu\nu}(\rho) = \left\langle\!\!\left\langle \Phi_\mu \left| \frac{\partial}{\partial\rho} \right| \Phi_\nu \right\rangle\!\!\right\rangle, \qquad (4.20)$$

and

$$Q_{\mu\nu}(\rho) = \left\langle\!\!\left\langle \Phi_\mu \left| \frac{\partial^2}{\partial\rho^2} \right| \Phi_\nu \right\rangle\!\!\right\rangle, \qquad (4.21)$$

where the double brackets denote integration over the two angular coordinates. The completeness requirement of the channel functions together with the antisymmetric properties of the coupling matrix $P_{\mu\nu}$, i.e., $P_{\mu\nu} = -P_{\nu\mu}$, are used to derive the following relation

$$Q_{\mu\nu} = \frac{dP_{\mu\nu}}{d\rho} + P_{\mu\nu}^2, \qquad (4.22)$$

where the square of the coupling matrix $P_{\mu\nu}$ is given by

$$P_{\mu\nu}^2 = \sum_\sigma P_{\mu\sigma}P_{\sigma\nu} = \sum_\sigma \left\langle\!\!\left\langle \Phi_\mu \left| \frac{\partial\Phi_\sigma}{\partial\rho} \right\rangle\!\!\right\rangle \left\langle\!\!\left\langle \Phi_\sigma \left| \frac{\partial\Phi_\nu}{\partial\rho} \right\rangle\!\!\right\rangle \right.$$
$$= \sum_\sigma -\left\langle\!\!\left\langle \frac{\partial\Phi_\mu}{\partial\rho} \right| \Phi_\sigma \right\rangle\!\!\right\rangle \left\langle\!\!\left\langle \Phi_\sigma \left| \frac{\partial\Phi_\nu}{\partial\rho} \right\rangle\!\!\right\rangle = -\left\langle\!\!\left\langle \frac{\partial\Phi_\mu}{\partial\rho} \left| \frac{\partial\Phi_\nu}{\partial\rho} \right\rangle\!\!\right\rangle. \qquad (4.23)$$

The antisymmetry of $P_{\mu\nu}$ together with $P_{\mu\nu}^2 = P_{\nu\mu}^2$ leads to $P_{\nu\nu} = 0$ and $Q_{\nu\nu} = P_{\nu\nu}^2$. A mathematical description of the nonadiabatic couplings and the operational procedures needed to numerically calculate them are given in Section 4.3.1.

4.3.1   The Hellmann–Feynman Theorem

This subsection concerns the mathematical description of the nonadiabatic coupling matrices. The nonadiabatic coupling terms defined in Eqs. (4.20) and (4.21) can be determined analytically by means of the Hellmann–Feynman (HF) theorem [28, 29]. In this setting, the theorem relates the derivative of the adiabatic potential U_ν with respect to the parametrized hyperradius, with the expectation value of the hyperradial derivative of the adaibatic Hamiltonian. Consider the ν adiabatic eigenstates Φ_ν obtained in Eq. (4.15). Using the identities

$$\langle\!\langle \Phi_\mu | \Phi_\nu \rangle\!\rangle \equiv \delta_{\mu\nu} \tag{4.24}$$

and

$$\frac{\partial}{\partial\rho}\langle\!\langle \Phi_\nu | \Phi_\nu \rangle\!\rangle \equiv 0, \tag{4.25}$$

the diagonal part of the HF theorem is retrieved by projecting Φ_ν out from Eq. (4.15) and differentiating with respect to the hyperradius

$$
\begin{aligned}
\frac{\partial U_\nu}{\partial\rho} &= \frac{\partial}{\partial\rho}\langle\!\langle \Phi_\nu | H_{ad} | \Phi_\nu \rangle\!\rangle \\
&= \langle\!\langle \Phi_\nu \Big| \frac{\partial H_{ad}}{\partial\rho} \Big| \Phi_\nu \rangle\!\rangle + \langle\!\langle \Phi_\nu \Big| H_{ad} \Big| \frac{\partial \Phi_\nu}{\partial\rho} \rangle\!\rangle + \langle\!\langle \frac{\partial \Phi_\nu}{\partial\rho} \Big| H_{ad} \Big| \Phi_\nu \rangle\!\rangle \\
&= \langle\!\langle \Phi_\nu \Big| \frac{\partial H_{ad}}{\partial\rho} \Big| \Phi_\nu \rangle\!\rangle + U_\nu \langle\!\langle \Phi_\nu \Big| \frac{\partial \Phi_\nu}{\partial\rho} \rangle\!\rangle + U_\nu \langle\!\langle \frac{\partial \Phi_\nu}{\partial\rho} \Big| \Phi_\nu \rangle\!\rangle \\
&= \langle\!\langle \Phi_\nu \Big| \frac{\partial H_{ad}}{\partial\rho} \Big| \Phi_\nu \rangle\!\rangle + U_\nu \frac{\partial}{\partial\rho} \langle\!\langle \Phi_\nu | \Phi_\nu \rangle\!\rangle \\
&= \langle\!\langle \Phi_\nu \Big| \frac{\partial H_{ad}}{\partial\rho} \Big| \Phi_\nu \rangle\!\rangle. \tag{4.26}
\end{aligned}
$$

The nondiagonal part is similarly given by

$$
\begin{aligned}
&\frac{\partial U_\nu}{\partial\rho}\langle\!\langle \Phi_\mu \Big| \Phi_\nu \rangle\!\rangle + U_\nu \langle\!\langle \Phi_\mu \Big| \frac{\partial \Phi_\nu}{\partial\rho} \rangle\!\rangle + U_\nu \langle\!\langle \frac{\partial \Phi_\mu}{\partial\rho} \Big| \Phi_\nu \rangle\!\rangle \\
&= \langle\!\langle \Phi_\mu \Big| \frac{\partial H_{ad}}{\partial\rho} \Big| \Phi_\nu \rangle\!\rangle + U_\mu \langle\!\langle \Phi_\mu \Big| \frac{\partial \Phi_\nu}{\partial\rho} \rangle\!\rangle + U_\nu \langle\!\langle \frac{\partial \Phi_\mu}{\partial\rho} \Big| \Phi_\nu \rangle\!\rangle. \tag{4.27}
\end{aligned}
$$

Due to the orthogonality of the channel functions in Eq. (4.24), the first term on the left hand side of this equation vanishes. By removing the last term on both sides we obtain the final expression

$$\left\langle\!\!\left\langle \Phi_\mu \left| \frac{\partial H_{ad}}{\partial \rho} \right| \Phi_\nu \right\rangle\!\!\right\rangle = (U_\nu - U_\mu) \left\langle\!\!\left\langle \Phi_\mu \left| \frac{\partial}{\partial \rho} \right| \Phi_\nu \right\rangle\!\!\right\rangle, \tag{4.28}$$

which results in the following expression of the nonadiabatic coupling terms $P_{\mu\nu}$

$$P_{\mu\nu} = \frac{1}{(U_\nu - U_\mu)} \left\langle\!\!\left\langle \Phi_\mu \left| \frac{\partial H_{ad}}{\partial \rho} \right| \Phi_\nu \right\rangle\!\!\right\rangle. \tag{4.29}$$

If it is assumed that the channel functions can be expressed as a series of basis functions

$$\Phi_\nu = \sum_j C_\nu^j \varphi_j, \tag{4.30}$$

where C_ν^j are expansion coeffients, which characterize the channel functions and the Hamiltonian operator takes the matrical form with elements H_{ij}, then the diagonal elements are obtained from the following matrical expression [30]

$$\frac{\partial U_\nu}{\partial \rho} = \sum_{ij} (C_\nu^i)^\dagger C_\nu^j \frac{\partial H_{ij}}{\partial \rho} \tag{4.31}$$

and the non-diagonal matrix elements are obtained by

$$\left\langle\!\!\left\langle \Phi_\mu \left| \frac{\partial}{\partial \rho} \right| \Phi_\nu \right\rangle\!\!\right\rangle = P_{\mu\nu} = \sum_{ij} (C_\mu^i)^\dagger C_\nu^j \frac{\partial H_{ij}}{\partial \rho}. \tag{4.32}$$

4.3.2   Three-body Effective Potentials

Approximations within the adiabatic treatment include both the hyperspherical Born–Oppenheimer approximation and the strict adiabatic approximation, where the former corresponds to neglecting all nonadiabatic couplings and the latter to neglecting all nondiagonal couplings [27].

The eigenvalues obtained using these two approximations are denoted $E_{\nu n}$. The lowest energy level E_{00}, obtained by solving Eq. (4.14) in the Born–Oppenheimer approximation, is a lower bound to the true ground state energy E_0, while the ground state energy obtained in the adiabatic

approximation is a variational upper bound to E_0.

In the adiabatic approximation the effective potentials are defined as

$$W_\nu(\rho) = U_\nu(\rho) - \frac{1}{2\mu}Q_{\nu\nu}(\rho) = U_\nu(\rho) - \frac{1}{2\mu}P_{\nu\nu}^2(\rho). \qquad (4.33)$$

These potentials are henceforth used to determine the single channel solutions of Eq. (4.19).

The following discussion concerns short-ranged two-body interactions, where $|a| \gg r_0$.

In the asymptotic limit $\rho \gg |a|$ the non-adiabatic couplings $Q_{\nu\nu}$ vanish and there are two possibilities for the asymptotic channels at large hyperradii ρ. The channel indices ν in this region are associated with both two- and three-body configurations since the adiabatic hyperspherical potential curves $U_\nu(\rho)$ asymptotically approach either a two-body bound state energy for the bound channels or the three-body breakup threshold ($U_\nu = 0$) for the three-body continuum channels. By comparison with the eigenvalues for the Gegenbauer polynomials in Eq. (4.17), it is clear that the potentials for the continuum channels have the following asymptotic behaviour

$$W_\nu(\rho) \xrightarrow{\rho \to \infty} \frac{\lambda(\lambda + 4) + \frac{15}{4}}{2\mu\rho^2}. \qquad (4.34)$$

However, the bound channels correspond to the atom-dimer configurations in the asymptotic limit, which means that the potentials for these channels asymptotically behave like

$$W_\nu(\rho) \xrightarrow{\rho \to \infty} E_{\nu l'} + \frac{l(l+1)}{2\mu\rho^2}, \qquad (4.35)$$

in which the bound state energy of the dimer $E_{\nu l'}$ is labelled with the rovibrational quantum numbers ν and l', and where l is the relative angular momentum between the pair and the third atom. For identical bosons symmetry requires that $l = l' = 0, 2, 4, \ldots$.

Efimov physics comes into play when $r_0 \ll \rho \ll |a|$. In this intermediate region, while still being proportional to ρ^{-2}, modifications of W_ν lead to three-body effective potentials that can be both attractive and repulsive.

For systems of three identical bosons with a pair-wise attraction that is strong enough to support two-body bound states, one three-body effective potential curve will converge asymptotically to each two-body bound state.

The one channel of particular interest is the one that leads to the Efimov effect[2]. For $a > 0$ this is the channel that converges asymptotically to the highest vibrationally excited s-wave bound state, i.e., the weakly bound dimer, and for $a < 0$ it is the lowest continuum channel. As the scattering length grows in magnitude for $a > 0$ and $a < 0$ the lowest effective potential will converge to the Efimov potential

$$W_\nu(\rho) = -\frac{s_0^2 + \frac{1}{4}}{2\mu\rho^2}, \qquad (4.36)$$

in which $s_0 \simeq 1.00624$. This potential is attractive, and hence responsible for the Efimov effect, since it produces an infinite number of bound trimers when $|a| = \infty$. For finite scattering lengths a number of Efimov trimers can still form provided that the magnitude of a is large enough. The number of Efimov states N that can be formed at a specific value of a can be derived using the form of the Efimov potential [31]

$$\begin{aligned} N &\simeq \frac{1}{\pi} \int_{r_0}^{|a|} \sqrt{-2\mu\left(W_\nu(\rho) + \frac{\frac{1}{4}}{2\mu\rho}\right)} \, d\rho \\ &= (s_0/\pi)\ln(|a|/r_0). \end{aligned} \qquad (4.37)$$

Thus, for finite scattering lengths the number of bound states supported by the potential increases rather slowly with $|a|$, even though there exists an infinite number of Efimov states at $a = \pm\infty$. Another intriguing property that can be revealed by examining Eq. (4.37) is that a new trimer is formed every time $|a|$ increases with a factor e^{π/s_0}, i.e., as $a \to a\mathrm{e}^{\pi/s_0}$. This geometric scaling of the length scale implies that each consecutively formed trimer is e^{π/s_0} times as large as the former and has a binding energy that is $\mathrm{e}^{2\pi/s_0}$ as small as the previous.

All higher lying potentials are continuum channels and none of them can support bound states, but they are also modified in the region $r_0 \ll \rho \ll |a|$. Instead of simply converging to the eigenvalues of the kinetic energy for $|a| \to \infty$, Efimov physics is manifested here by the repulsive effective potentials converging to

---

[2]Strictly speaking, the Efimov effect is the emergence of an infinite number of weakly bound trimers and only for $|a| = \infty$ is the emergent effective potential infinitely extended, which of course is required for an infinite number of bound states. However, for large but finite $|a|$ a number of bound trimers can still form.

$$W_\nu(\rho) = \frac{s_\nu^2 - \frac{1}{4}}{2\mu\rho^2}, \tag{4.38}$$

where s_ν is a real constant.

4.4 Hyperangular Coordinates

To solve Eq. (4.15) we need to introduce some explicit form of the hyper-angles Ω and express Λ^2 and V in these coordinates. As mentioned in Section 4.2 two different forms of coordinates are commonly used.

4.4.1 Delves Coordinates

Delves coordinates are adapted to collinear atom-diatom collisions and are regular polar coordinates. They where originally developed to treat nuclear three-body problems. Each coordinate set is defined by the Jacobi vectors in Eqs. (4.4) and (4.5), and

$$r_k = \rho \sin \alpha_k, \tag{4.39}$$

$$R_k = \rho \cos \alpha_k, \tag{4.40}$$

where the Delves hyperangle α_k, which correlates to the lengths of these vectors, is defined by

$$\alpha_k = \arctan\left(\frac{r_k}{R_k}\right), \quad 0 \le \alpha_k \le \frac{\pi}{2}. \tag{4.41}$$

This coordinate set corresponds to the reactant arrangement when particle k scatters off the weakly bound particles ij. The other angle in this set is the angle between the two vectors $\mathbf{r}_k$ and $\mathbf{R}_k$. It is given by

$$\cos \theta_k = \frac{\mathbf{r}_k \cdot \mathbf{R}_k}{r_k R_k}, \quad 0 \le \theta \le \pi. \tag{4.42}$$

For simplicity, the indicies labelling each coordinate set will be suppressed from hereon.

The full derivation of the three-body Schrödinger equation written in Delves coordinates is given in Appendix A.1; here we simply state the results. After rescaling the total wave function, $\psi = \rho^{5/2} \sin 2\alpha \Psi$, the Schrödinger

equation can be written

$$\left(-\frac{1}{2\mu}\frac{\partial^2}{\partial\rho^2} + \frac{\Lambda^2 - 1/4}{2\mu\rho^2} + V(\rho, \alpha, \theta)\right)\psi(\rho, \alpha, \theta) = E\psi(\rho, \alpha, \theta), \quad (4.43)$$

in which E is the internal energy and where the squared grand angular momentum operator Λ^2, which contains all angular variables, is given by

$$\Lambda^2 = -\frac{\partial^2}{\partial\alpha^2} - \frac{1}{\sin^2\alpha\cos^2\alpha\sin\theta}\frac{\partial}{\partial\theta}\left(\sin\theta\frac{\partial}{\partial\theta}\right). \quad (4.44)$$

The corresponding volume element is proportional to $\rho^5 \sin^2\alpha \cos^2\alpha \sin\theta \, d\rho \, d\alpha \, d\theta$. To be square-integrable, the rescaled wavefunction for a bound state must obey the boundary conditions

$$\psi(0, \alpha, \theta) = 0, \quad (4.45)$$

$$\psi(\rho, 0, \theta) = \psi(\rho, \frac{\pi}{2}, \theta) = 0, \quad (4.46)$$

$$\left.\frac{\partial\psi}{\partial\theta}\right|_{\theta=0} = \left.\frac{\partial\psi}{\partial\theta}\right|_{\theta=\pi} = 0. \quad (4.47)$$

Numerical difficulties arise with these coordinates when permutation symmetries for three identical particles are considered [32].

In the context of Efimov physics, Delves coordinates are often used for derivations in conjunction with the Faddeev equations. The three-body wave equation is then expressed as a sum of components, which each uses a different set of Jacobi coordinates to express the three atom-dimer configurations. The total wave function is thus given by

$$\Psi = \psi_1(\mathbf{r}_1, \mathbf{R}_1) + \psi_2(\mathbf{r}_2, \mathbf{R}_2) + \psi_3(\mathbf{r}_3, \mathbf{R}_3). \quad (4.48)$$

The component wave functions satisfy the set of coordinate space Faddeev equations

$$(T - E)\psi_i + v_i(\psi_1 + \psi_2 + \psi_3) = 0, \quad (4.49)$$

where $i = 1, 2, 3$ and v_i is the pair-wise interaction between the particles j and k. At very low energies the contribution to the scattering cross-section of partial waves with $l > 0$ is negligible and in general it is enough to only

consider *s*-waves. Thus, if the orbital angular momentum of each subsystem is neglected, then the total three-body wave function in Eq. (4.48) takes the form

$$\Psi = \psi_1(\rho, \alpha_1) + \psi_2(\rho, \alpha_2) + \psi_3(\rho, \alpha_3). \tag{4.50}$$

The Faddeev equations in Eq. (4.49) can be reduced to the three identical equations

$$(T_\rho + T_{\alpha_i} - E)\psi_i(\rho, \alpha_i) + v_i(d_i\rho\sin\alpha_i)(\psi_1(\rho, \alpha_1) + \psi_2(\rho, \alpha_2) + \psi_3(\rho, \alpha_3)) = 0, \tag{4.51}$$

with $i = 1, 2, 3$, and where the kinetic energy operators T_ρ and T_{α_i} are given in Eqs. (A.22) and (A.23) in Appendix A.1. By rotating the second and third equation into the first [33], the Faddeev equation for three identical particles becomes

$$(T_\rho + T_\alpha - E)\psi(\rho, \alpha) + v(\sqrt[4]{\tfrac{4}{3}}\rho\sin\alpha)\left[\psi(\rho, \alpha) + \frac{4}{\sqrt{3}}\int_{|\frac{\pi}{3} - \alpha|}^{\frac{\pi}{2} - |\frac{\pi}{6} - \alpha|}\frac{\sin 2\alpha'}{\sin 2\alpha}\psi(\rho, \alpha')\,d\alpha'\right] = 0, \tag{4.52}$$

where $\alpha = \alpha_1, \alpha_2$ or α_3. The integro-differential Faddeev equation (4.52) can be solved by expanding the wave function ψ in a complete set of hyperangular wave functions

$$\psi(\rho, \alpha) = \sum_n \frac{f_n(\rho)}{\rho^{5/2}}\frac{\Phi_n(\rho; \alpha)}{\sin\alpha\cos\alpha}, \tag{4.53}$$

in which Φ_n are the eigenfunctions to the hyperangular Faddeev equation

$$-\frac{\partial^2 \Phi_n(\rho; \alpha)}{\partial\alpha^2} + \rho^2 v(\sqrt[4]{\tfrac{4}{3}}\rho\sin\alpha)\left[\Phi_n(\rho; \alpha) + \frac{4}{\sqrt{3}}\int_{|\frac{\pi}{3} - \alpha|}^{\frac{\pi}{2} - |\frac{\pi}{6} - \alpha|}\frac{\sin 2\alpha'}{\sin 2\alpha}\Phi(\rho; \alpha')\,d\alpha'\right] = \nu_n(\rho)\Phi(\rho; \alpha). \tag{4.54}$$

The eigenvalues $\nu_n(\rho)$ are adiabatic potentials, which can be related to the effective potentials $U_n(\rho)$ in Eq. (4.15) by

$$U_n(\rho) = \left(\nu_n(\rho) - \frac{1}{4}\right)\frac{1}{2\mu\rho^2}. \tag{4.55}$$

Fedorov and Jensen showed [33] that for $\rho \gg r_0$ the adiabatic potentials

ν_n can be determined analytically through the transcendental equation

$$\sqrt{\nu_n}\cos\left(\sqrt{\nu_n}\frac{\pi}{2}\right) - \frac{8}{\sqrt{3}}\sin\left(\sqrt{\nu_n}\frac{\pi}{6}\right) = \sqrt[4]{\frac{4}{3}}\frac{\rho}{a}\sin\left(\sqrt{\nu_n}\frac{\pi}{2}\right), \qquad (4.56)$$

for different scattering lengths a. In the limit $|a| \to \infty$ the right hand side vanishes and the resulting transcendental equation has the solutions $\sqrt{-\nu_0(0)} = s_0$ and $\sqrt{\nu_n} = s_n$.

4.4.2 Smith-Whitten Coordinates

The motion of three particles can be represented in a symmetric way by using so called democratic coordinates. The main advantage with these kinds of coordinates is that permutation symmetries for three identical particles can be imposed exactly. To define the two hyperangles θ and ϕ I use the mapping procedure described by Johnson [34] to produce a modified set of the coordinates first introduced by Smith and Whitten [35], see Appendix A.2.1. Here I am content with presenting the results. The two hyperangles are defined by

$$\begin{aligned}
r_x &= \rho\cos(\pi/4 - \theta/2)\cos(2\pi - \phi/2), \\
r_y &= -\rho\sin(\pi/4 - \theta/2)\sin(2\pi - \phi/2), \\
r_z &= 0 \\
R_x &= \rho\cos(\pi/4 - \theta/2)\sin(2\pi - \phi/2), \\
R_y &= \rho\sin(\pi/4 - \theta/2)\cos(2\pi - \phi/2), \\
R_z &= 0.
\end{aligned} \qquad (4.57)$$

The hyperangle θ spans the range $[0, \pi/2]$ and, by requiring the wave function to be single valued, the span of ϕ is restricted to the range $[0, 2\pi]$.

The hyperangular coordinates are connected to the geometry of the triangle formed by the three particles, with θ determining its shape and ϕ the particle arrangement at the vertices. The geometrical configuration of the particles when $\theta = 0$ is an equilateral triangle, while at $\theta = \pi/2$ they form a line.

The derivation of the Schrödinger equation in these coordinates is presented in Appendix A.2.2. In order to remove the first order derivative term in the hyperradial coordinate, the Schrödinger equation is expressed in terms

of the rescaled wave function $\psi = \rho^{5/2}\Psi$ as

$$\left(-\frac{1}{2\mu}\frac{\partial^2}{\partial\rho^2} + \frac{\Lambda^2 + \frac{15}{4}}{2\mu\rho^2} + V(\rho,\theta,\phi)\right)\psi(\rho,\theta,\phi) = E\psi(\rho,\theta,\phi), \qquad (4.58)$$

where the corresponding volume element is $\frac{1}{16}\rho^5 \sin 2\theta \sin\beta\, d\rho\, d\theta\, d\phi\, d\alpha\, d\beta\, d\gamma$, with α, β, γ being Euler angles. The squared grand angular momentum operator Λ^2 for $J = 0$ states is given by

$$\Lambda^2 = -\frac{4}{\sin 2\theta}\frac{\partial}{\partial\theta}\sin 2\theta\frac{\partial}{\partial\theta} - \frac{4}{\sin^2\theta}\frac{\partial^2}{\partial\phi^2}. \qquad (4.59)$$

For three identical particles, the hyperradius is written in terms of the interparticle distances r_{ij} as

$$\rho^2 = \frac{r_{12}^2 + r_{23}^2 + r_{31}^2}{\sqrt{3}}, \qquad (4.60)$$

where the interparticle distances are

$$\begin{aligned}
r_{12} &= \sqrt[4]{\tfrac{1}{3}}\rho\left[1 + \sin\theta\cos\phi\right]^{1/2}, \\
r_{23} &= \sqrt[4]{\tfrac{1}{3}}\rho\left[1 + \sin\theta\cos(\phi - 2\pi/3)\right]^{1/2}, \\
r_{31} &= \sqrt[4]{\tfrac{1}{3}}\rho\left[1 + \sin\theta\cos(\phi + 2\pi/3)\right]^{1/2}.
\end{aligned} \qquad (4.61)$$

The particles permutate in a cyclical manner as the hyperangular coordinate ϕ changes from 0 to 2π. The symmetric properties of the wave function depend on the parity of the system and for a general system the symmetry requirement is [36]

$$\Phi_\nu(\rho;\theta,\phi = 0) = \pm\Phi_\nu(\rho;\theta,\phi = 2\pi), \qquad \text{for} \qquad \Pi = \pm 1. \qquad (4.62)$$

For three identical particles the range is reduced to $[0, 2\pi/3]$ and

$$\Phi_\nu(\rho;\theta,\phi = 0) = \pm\Phi_\nu(\rho;\theta,\phi = 2\pi/3), \qquad \text{for} \qquad \Pi = \pm 1. \qquad (4.63)$$

Moreover, by defining the hyperangles in this way, the interaction potential for three indistinguishable particles becomes invariant under reflection about

$\phi = \pi/3$, see Fig. A.1 in Appendix A.2.1. The solutions to the Schrödinger equation are therefore either symmetric (for bosons) or antisymmetric (for fermions) under exchange of any two particles in this restricted domain. The original range of ϕ is thus reduced by a factor 3! for three identical particles and for $J^\pi = 0^+$ symmetry[3] to be fullfilled the ϕ derivative of the wave function must vanish at 0 and $\pi/3$ [37].

To derive boundary conditions for the hyperangle θ it is convenient to write the eigenfunctions of the squared angular momentum as basis functions on the form

$$\Phi_{lm}(\theta, \phi) = g_l(\theta)e^{im\phi}. \tag{4.64}$$

The eigenvalue equation for the squared grand angular momentum operator can then be written

$$\Lambda^2 \Phi_{lm} = U_{lm}\Phi_{lm}. \tag{4.65}$$

For the ϕ term in Eq. (4.59) the eigenvalues are

$$\frac{\partial^2}{\partial\phi^2}e^{im\phi} = -m^2 e^{im\phi}. \tag{4.66}$$

Then for the wave function to be completely symmetric for even parity 0^+ states the ϕ dependence on the basis functions should take the form

$$e^{im2\pi/3} = 1, \tag{4.67}$$

which implies $m = 3n$, where $n = 0, 1, 2, \ldots$. Substituting Eq. (4.64) into Eq. (4.59) leads to

$$-4\left(\frac{1}{\sin 2\theta}\frac{\partial}{\partial\theta}\sin 2\theta\frac{\partial}{\partial\theta} - \frac{m^2}{\sin^2\theta}\right)g_l(\theta) = \lambda_{lm}g_l(\theta). \tag{4.68}$$

The boundary condition for $\theta = 0$ is determined by taking the limit $\theta \to 0$, in which

$$\Lambda^2 \to -4\left(\frac{\partial^2}{\partial\theta^2} + \frac{1}{\theta}\frac{\partial}{\partial\theta} - \frac{m^2}{\theta^2}\right) \tag{4.69}$$

---

[3]For a three-body system, the number and kind of identical particles for each partial wave are denoted J^π, where J is the total angular momentum and π is the parity. For exemple, the bosonic state for three identical particles is therefore denoted 0^+.

and assume that $g_l(\theta) \propto \theta^s$. Then to leading order

$$\Lambda^2 g_l(\theta) = 0, \tag{4.70}$$

where the leading order coefficents imply

$$s(s-1) + s - m^2 = 0 \quad \Rightarrow \quad s = \pm m. \tag{4.71}$$

Requiring Φ_ν to be bounded everywhere on the range means that g_l must not diverge as $\theta \to 0$. Because $g_l(\theta) \propto \theta^m$ in the limit $\theta \to 0$ and since $g_l(0) \neq 0$ in the case $m = 0$, it is implied that for $m = 0$ the θ derivative of the wave function must vanish at $\theta = 0$.

The boundary condition at $\theta = \pi/2$ is determined by setting $\theta = \pi/2 - \varepsilon$ and taking the limit $\varepsilon \to 0^+$. In this limit

$$\Lambda^2 \to -4 \left(\frac{\partial^2}{\partial\varepsilon^2} + \frac{1}{\varepsilon} \frac{\partial}{\partial\varepsilon} - m^2 \right). \tag{4.72}$$

By assuming that the basis function takes the form $g_l(\theta) \propto \varepsilon^s$ as $\theta \to \pi/2$, then to leading order

$$s(s-1) + s = 0 \quad \Rightarrow \quad s = 0. \tag{4.73}$$

Since $s = 0$ the function $g_l(\pi/2)$ approaches some constant in the limit $\theta \to \pi/2$, which implies that the θ derivative of the wave function must vanish at this boundary as well.

Identical particle symmeries can therefore easily be built into the adiabatic equation (4.15) when using these kinds of symmetrized hyperangular coordinates. For three identical particles with 0^+ symmetry the boundary conditions are

$$\frac{\partial \Phi_\nu(\rho; 0, \phi)}{\partial \theta} = \frac{\partial \Phi_\nu(\rho; \frac{\pi}{2}, \phi)}{\partial \theta} = 0, \tag{4.74}$$

$$\frac{\partial \Phi_\nu(\rho; \theta, 0)}{\partial \phi} = \frac{\partial \Phi_\nu(\rho; \theta, \frac{\pi}{3})}{\partial \phi} = 0. \tag{4.75}$$

The eigenvalues of Λ^2 can be derived analytically and are given by

$$U_{lm} = \lambda_{lm}(\lambda_{lm} + 4), \quad \text{where} \quad \lambda_{lm} = 2(l+m). \tag{4.76}$$

Table 4.1 presents the analytically derived eigenvalues at the three first m-values ($m = 0, 3, 6$) together with the eigenvalues ($\tilde{U}_\nu$) obtained by numerically solving Eq. (4.65) by expanding $\Phi_\nu(\rho; \theta, \phi)$ onto a direct product of B-splines[4] in θ and ϕ on a mesh containing $N_\theta = N_\phi = 60$ physical points.

$U_{l,m=0}$	$U_{l,m=3}$	$U_{l,m=6}$	$\tilde{U}_{[\nu]}$	$\lambda_{[lm]}$	Multiplicity
0	60	192	$-0.00000000_{[0]}$	$0_{[00]}$	1
32	140	320	$32.00000001_{[1]}$	$4_{[20]}$	1
96	252	480	$60.00000000_{[2]}$	$6_{[03]}$	1
192	396	672	$95.99999998_{[3]}$	$8_{[40]}$	1
320	572	896	$140.00000000_{[4]}$	$10_{[23]}$	1
480	780	1152	$192.00000001_{[5,6]}$	$12_{[06]}$	2
672	1020	1440	$192.00000001_{[5,6]}$	$12_{[60]}$	
			$252.00000000_{[7]}$	$14_{[43]}$	1

Table 4.1: Analytically derived eigenvalues together with numerically calculated eigenvalues for three identical bosons.

---

[4]B-splines of order $k = 6$ were used for both dimensions, which corresponds to local polynomials of degree 5, see Appendix B.

Chapter 5

Numerical Approach

To find numerical solutions of Eq. (4.15), I have used the B-spline collocation method, with spatial discretization at Gauss points in each subinterval of the mesh and integration using the Gauss-Legendre quadrature rule. The outline of this method is described in the following sections.

Section 5.1 contains a hands-on mapping scheme for setting up the two-dimensional Hamiltonian and overlap matrices. Two key features of these matrices are that they are sparse and banded[1], which means that most of the entries in the two matrices are zero. This is beneficial since Gaussian elemination can be perfomed in fewer operations than normal and there are several numerical routines specifically designed to treat these kinds of matrices when solving generalized eigenvalue problems.

The structure of these matrices and how different mappings affect their bandwidth, and hence the numerical efficiency, has been discussed in detail by Esry [38].

5.1   Basis Splines Expansion

The first step in solving the adiabatic equation is to expand the solution, i.e., the channel functions Φ_ν, in a suitable basis. For this I use B-splines. These basis functions are piecewise polynomial functions, which are defined using the *Cox-de Boor recursion formula*, see Appendix B.

---

[1] A matrix is considered sparse if its sparsity ratio $\left(= 1 - \frac{\#\text{non-zero entries}}{\#\text{entries}} \right)$ is close to one. Additionally, if all non-zero entries are confined to a diagonal band located about the main diagonal and its bandwidth – i.e., the maximum distance of non-zero elements from the main diagonal – is small, then it is called banded.

A base function in two dimensions can be generated from one-dimensional B-splines. If φ_{1l}, $l = 1, \ldots, L$ is a basis for representing the functional dependency on θ and φ_{2m}, $m = 1, \ldots, M$ is a basis for ϕ, then the tensor product of the two base functions is defined by

$$\varphi_{lm}(\theta, \phi) = \varphi_{1l}(\theta)\varphi_{2m}(\phi). \tag{5.1}$$

A two-dimensional basis can thus be built as a product of one-dimensional B-splines. The channel functions are then represented as an expansion in this basis through

$$\Phi_\nu(\rho; \theta, \phi) = \sum_{l,m}^{L,M} c_{lm}(\rho)\varphi_{lm}(\theta, \phi), \tag{5.2}$$

where c_{lm} are the sought expansion coefficients, which characterize our solution. If we use B-splines of order k, defined as piecewise polynomials of order $(k-1)$ and define a mesh containing N_θ physical points in the θ-direction and N_ϕ physical points in the ϕ-direction, then we need to construct two knot point sequences, where k ghost points are put in the first and last physical point on each grid, see Appendix B.

Boundary conditions are easily enforced by placing the ghost-points at the end-points of the two grids. Since only the first and last B-spline is non-zero at its respective boundary, implementing the boundary condition with the requirement that the solution must vanish at that boundary simply means that you remove that non-zero B-spline from the expansion. Similarly, only the first two or the last two B-splines have non-zero first derivatives at the boundaries. Thus, to implement the requirement that the derivative of the solution must vanish at a boundary one replaces the B-spline in that place in the expansion with the sum of the two first B-splines if the first physical point is considered or the two last B-splines if the last point is considered.

For a second order partial differential equation the B-splines must be twice differentiable everywhere on the knot sequence and have continuous second order derivatives. With the B-spline definitions given in Appendix B, the above requirements are fullfilled for B-splines of order $k \geq 4$.

The upper limits of the sum in Eq. (5.2) are determined from the order of the B-splines and the number of mesh points for each coordinate through

$L = N_\theta + k - 2$ and $M = N_\phi + k - 2$, if no boundary conditions are placed on the coordinates. However, since for each boundary condition, we get an additional equation and reduce the number of B-splines in that dimension by one, the limits L and M are given by

$$L = N_\theta + k - 2 - c_L, \tag{5.3}$$

$$M = N_\phi + k - 2 - c_M, \tag{5.4}$$

where $c_{L/M}$ denotes the number of boundary conditions for the coordinate in question.

Thereafter we choose collocation at the knot points and require that Eq. (5.2) is a solution to Eq. (4.15) at those points. Since only $(k-1)^2$ B-splines are non-zero at the knot points, it means that each equation involves $(k-1)^2$ B-splines

$$\Phi_\nu(\rho; \theta_i, \phi_j) = \sum_{l=i-k+1}^{i-1} \sum_{m=j-k+1}^{j-1} c_{lm}(\rho)\varphi_{lm}(\theta_i, \phi_j), \tag{5.5}$$

in which $i = k, \ldots, L + k$ and $j = k, \ldots, M + k$.

The next step is to substitute the solution in Eq. (5.2) into the adiabatic equation (4.15) and projecting out $\varphi_{l'm'}(\theta, \phi)$. If the two indicies l and m are mapped into a single index i, where

$$\begin{aligned} i &= (l-1)M + m \quad \text{or} \\ i &= (m-1)L + l, \end{aligned} \tag{5.6}$$

then the matrix equation can be written

$$\mathbf{H}_{ad}\mathbf{c} = U\mathbf{B}\mathbf{c}, \tag{5.7}$$

where the elements of the adiabatic Hamiltonian matrix $\mathbf{H}_{ad}$ are defined by

$$H_{ad_{i'i}} = \iint \varphi_{l'm'}(\theta, \phi)H_{ad}(\rho; \theta, \phi)\varphi_{lm}(\theta, \phi)\, d\theta\, d\phi, \tag{5.8}$$

and where the overlap matrix elements are defined by

$$B_{i'i} = \iint \varphi_{l'm'}(\theta, \phi)\varphi_{lm}(\theta, \phi)\, d\theta\, d\phi. \tag{5.9}$$

The potential term in the adiabatic Hamiltonian cannot be separated into a product of two one-dimensional integrals and must therefore be integrated in two angular dimensions.

5.2   Gauss-Legendre Quadrature

In this work, all integrals have been calculated with Gaussian quadrature. Quadrature rules are used for numerically approximating the definite integral of a function. An n-point Gaussian quadrature rule is constructed to exactly[2] integrate polynomials of degree $2n-1$ or less if the abscissas x_i and weights w_i for $i = 1, \ldots, n$ are appropriately chosen.

If the integrand $f(x, y)$ is well approximated by the monomials $x^i y^j$ of degree $i = 2n - 1$, $j = 2m - 1$ or less, then the Gauss-Legendre quadrature rule for integration on an arbitrary interval is formulated by first changing the variables

$$
\begin{aligned}
u &= \frac{x - a}{b - a} - \frac{b - x}{b - a} \to x = u\frac{b - a}{2} + \frac{a + b}{2}, \, dx = \frac{b - a}{2} \, du, \\
v &= \frac{y - c}{d - c} - \frac{d - y}{d - c} \to y = v\frac{d - c}{2} + \frac{c + d}{2}, \, dy = \frac{d - c}{2} \, dv,
\end{aligned}
\tag{5.10}
$$

and then writing the integral as

$$
\begin{aligned}
\int_a^b \int_c^d f(x, y) \, dx \, dy &= \frac{b - a}{2} \cdot \frac{d - c}{2} \int_{-1}^1 \int_{-1}^1 f\left(u\frac{b - a}{2} + \frac{a + b}{2}, v\frac{d - c}{2} + \frac{c + d}{2}\right) du \, dv, \\
&\approx \frac{b - a}{2} \cdot \frac{d - c}{2} \sum_{i=1}^n \sum_{j=1}^m w_i \tilde{w}_j f\left(u_i\frac{b - a}{2} + \frac{a + b}{2}, v_j\frac{d - c}{2} + \frac{c + d}{2}\right)
\end{aligned}
\tag{5.11}
$$

where $u_i(v_j)$ and $w_i(\tilde{w}_j)$ are Gaussian quadrature points and weights of order $n(m)$ in the $u(v)$ direction. Weights and abscissas for different Gaussian quadrature rules can be found online, for example in [39].

In the following example, I use the overlap matrix to illustrate how integration in each subinterval of the mesh can be set up. Note that when calculating matrix elements we only need to integrate over the knot points where the B-splines $(\varphi_{l'm'}(\theta, \phi)\varphi_{lm}(\theta, \phi))$ are non-zero. On the knot sequence t_l,

---

[2]To within machine precision.

the B-splines $\varphi_{1l'}$ and φ_{1l} are non-zero on the interval $[t_{\max(l',l)}, t_{\min(l',l)+k}]$, so the integration can be divided into several segments, with integration in each subinterval of the mesh. If t_l and t_m are our two knot point sequences and k is the order of the B-splines, then the overlap matrix elements are obtained by

$$
\begin{aligned}
B_{i'i} &= \int_{t_{\max(l',l)}}^{t_{\min(l',l)+k}} \int_{t_{\max(m',m)}}^{t_{\min(m',m)+k}} \varphi_{l'm'}(\theta,\phi)\varphi_{lm}(\theta,\phi)\, d\theta\, d\phi \\
&= \sum_{n=\max(l',l)}^{\min(l',l)+k-1} \sum_{p=\max(m',m)}^{\min(m',m)+k-1} \int_{t_n}^{t_{n+1}} \int_{t_p}^{t_{p+1}} \varphi_{l'm'}(\theta,\phi)\varphi_{lm}(\theta,\phi) d\theta\, d\phi,
\end{aligned}
\tag{5.12}
$$

in which

$$
\begin{aligned}
&\int_{t_n}^{t_{n+1}} \int_{t_p}^{t_{p+1}} \varphi_{l'm'}(\theta,\phi)\varphi_{lm}(\theta,\phi) d\theta\, d\phi \\
&= \left[\theta_n = \frac{t_n + t_{n+1}}{2} + u_n \frac{t_n + t_{n+1}}{2}, \ \phi_p = \frac{t_p + t_{p+1}}{2} + u_p \frac{t_p + t_{p+1}}{2}\right] \\
&\approx \frac{t_n + t_{n+1}}{2} \cdot \frac{t_p + t_{p+1}}{2} \sum_{n=1}^{k} \sum_{p=1}^{k} w_n w_p \varphi_{l'm'}(\theta_n, \phi_p)\varphi_{lm}(\theta_n, \phi_n).
\end{aligned}
\tag{5.13}
$$

Since the B-splines are piecewise polynomial functions of order $(k-1)$, it is in principle possible to evaluate the overlap matrix elements and the kinetic terms in the adiabatic Hamiltonian exactly, i.e., to within machine precision, using Gauss-Legendre quadrature. These terms can also be separated into a product of one-dimensional integrals, which is advantageous since the computational cost of numerical integration grows exponentially with the dimension of the problem.

However, the potential term cannot be separated into a product of one-dimensional integrals, wherefore integration in two dimensions is required for this term. Another issue with the potential is that it is not generally a polynomial, so for the calculation to converge, we need a fine enough mesh.

To calculate the sought eigenvalues and corresponding eigenvectors, i.e., the effective three-body potential curves and the unknown coefficents, I have used the Lapack routine *dsygvd*. To show convergence to the analytical results presented in Table 4.1, I numerically calculated the first three eigenval-

ues $\tilde{U}_\nu$ obtained by solving Eq. (4.65) using the B-spline collocation method with an increasing number of mesh points $N_\theta = N_\phi$. The results are presented in Table 5.1. Convergence of all three eigenvalues have been reached at $N_\theta = 15$, since there is no further improvement of the calculated values when the mesh size is increased to $N_\theta = 25$ in each direction.

N_θ	$\tilde{U}_0$	$\tilde{U}_1$	$\tilde{U}_2$	Array(s)	dsygvd(s)
5	0.000 000 000 0043	32.000 000 071 3239	60.000 002 030 9903	0.05	0.00
15	−0.000 000 000 0259	32.000 000 000 1938	59.999 999 999 9500	0.82	0.05
25	0.000 000 000 1771	32.000 000 000 3968	60.000 000 000 1787	2.71	0.65

Table 5.1: The three lowest numerical eigenvalues $\tilde{U}_n$ calculated with an increasing number of B-splines in each hyperangular coordinate. All three eigenvalues have converged at $N_\theta = 15$. The analytical eigenvalues are $U_{00} = 0$, $U_{20} = 32$ and $U_{03} = 60$, see Table 4.1.

Chapter 6

Scattering Model

A system of three identical bosons with $J = 0$ and masses $m = m(^{87}\text{Rb})$ has been considered in this work. We have assumed that the interactions $V(\rho, \theta, \psi)$ can be written as a sum of pairwise two-body potentials

$$V(\rho, \theta, \psi) = v(r_{12}) + v(r_{23}) + v(r_{31}). \tag{6.1}$$

Since a general feature of the Efimov effect is that it is insensitive to the details of the short-ranged interatomic interactions and that it, to a good approximation, only depends on the scattering length and the interaction range it allows for the use of model potentials, where the scattering length and the number of two-body bound states can be controlled. The two-body potential used here is

$$v(r) = -d \cosh^{-2}(r/r_0), \tag{6.2}$$

where d controls the depth and r_0 the range of the potential. This potential is particularly useful since the eigenfunctions and energies are known analytically [24]. The scattering length can be calculated at different d numerically as described in Section 3.2.1, or can be expressed analytically as a function of d through

$$a = \lim_{k \to 0} \frac{1}{ik} \frac{S(k) - 1}{S(k) + 1} \tag{6.3}$$

in which $S(k)$ is the diagonal S-matrix element given by

$$S(k) = 2^\varepsilon \frac{{}_2F_1(-s, s+1, 1-\varepsilon; \frac{1}{2})}{{}_2F_1(\varepsilon - s, \varepsilon + s + 1, 1 + \varepsilon; \frac{1}{2})}, \tag{6.4}$$

where ${}_2F_1$ is the hypergeometrical function, $\varepsilon = ikr_0$, $k = \sqrt{mE_{2b}}$, $s = \frac{1}{2}(-1 + \sqrt{1 - 4mdr_0^2})$. The two-body s-wave eigenenergies are given by

$$E_{2b} = -\frac{\left(-(1+2n) + \sqrt{1 - 4mdr_0^2}\right)^2}{4mr_0^2}. \tag{6.5}$$

The binding energy for the shallow dimer for $a > 0$ is universal and can be well approximated by equation (1.5) if the scattering length is sufficiently large.

The scattering length is plotted as a function of the potential depth in Fig. 6.1 using the range $r_0 = 55$ a.u. and the mass of ^{87}Rb, which is precisely the same results as in [27]. By changing the depth d, the potential can be tuned to support a different number of two-body bound s-wave states. The formation of a two-body bound state can be recognized by the scattering length going through a pole. Three such poles can be seen in Fig. 6.1, labelled I, II and III. At each pole a new bound state is formed. The first weakly bound dimer is formed as a passes through I from the left. Then, as a approaches II the first bound state becomes deeply bound and a second bound state is formed as a goes through II and again becomes positive. A third bound state is formed in the same manner as a passes over III to the positive side.

The two-body potential surfaces $V(\rho, \theta, \phi)$ for two different hyperradii ρ are shown in Fig. 6.2. The potential surface can be seen to change more rapidly near the hyperangular configurations $(\theta, \phi) = (\pi/2, \phi)$ for larger ρ.

Figure 6.1: The two-body scattering length as a function of the potential depth d. Three poles can be recognized in the figure, labelled I, II and III. For values of d that lie between the poles I and II, the potential is deep enough to support a single s-wave bound state.

(a) The potential surface for $\rho = r_0$.   **(b)** The potential surface for $\rho = 3r_0$.
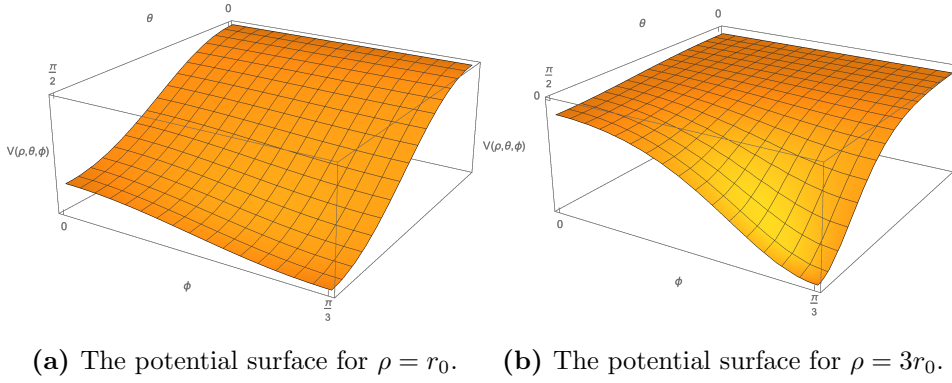
Figure 6.2: Illustration of the two-body potential surfaces at two different hyper-radii ρ. The potential surface change more rapidly at the hyperangular configuration $(\theta, \phi) = (\pi/2, \phi)$ for larger ρ.
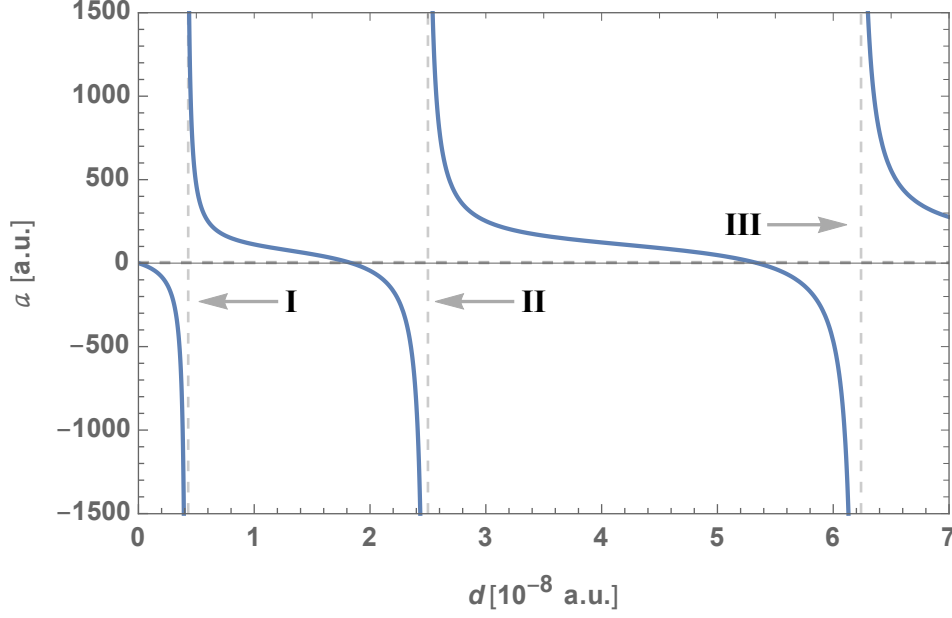
Chapter 7

Results and Discussion

The results presented here concern the three-body effective potential curves obtained by solving Eq. (4.15) within the strict adiabatic treatment, see Section 4.3.2. Signatures of the Efimov effect can be revealed in the structure of these adiabatic hyperspherical potentials, with the Efimov channel corresponding to the one emergent attractive potential converging to (4.36) in the region $r_0 \ll \rho \ll |a|$.

The adiabatic potential curves were obtained by numerically solving Eq. (4.15) in two-dimensional hyperangular space at fixed hyperradii using the method outlined in Chapter 5. The two-body scattering model described in Chapter 6 was used with the interaction range fixed at $r_0 = 55$ a.u. and with masses corresponding to the bosonic rubidium isotope $m = m(^{87}\mathrm{Rb})$.

We expect the potential curves to converge towards (4.36) for $|a| \to \infty$. This behaviour is more easily recognized if the potentials are multiplied by $2\mu\rho^2$ and plotted as

$$\xi(\rho) = 2\mu\rho^2 W_\nu(\rho) + \frac{1}{4}, \tag{7.1}$$

since these curves should approach the universal value $-s_0^2 (\simeq -1.0125$ for $J = 0^+$ states) for the lowest effective potential. This scenario is restricted to the range $r_0 \ll \rho \ll |a|$ and we only expect to find a potential $\xi(\rho)$ that is infinitely extended towards this universal value in the resonant regime when the magnitude of the scattering length is infinite. In this regime, the solution $\xi_\infty(\rho/|a|) = -s_0^2$ gives rise to an effective attractive potential, which is proportional to ρ^{-2}. This effective attractive potential is substituted into the hyperradial equation (4.19), where it in turn results in an infinite number

of bound trimer states.

We start by exploring Efimov's original scenario for two effective potentials calculated with two-body interactions very close to the resonant regime $a \approx \pm\infty$. The values of the potential depths d were tuned near the pole labelled I in Fig. 6.1, so that the two-body potential was just short of, or could just barely, support a single two-body bound state. To confirm the validity of the code the convergence of the adiabatic eigenvalues was tested over a broad range of hyperradii ρ using an increasing number of B-splines in each hypersperical dimension.

In Table 7.1 we present a systematic analysis of the numerical potential values $\xi(\rho)$ for the two cases where the scattering length was tuned to $a_1 \rightarrow -\infty$ and $a_2 \rightarrow \infty$. The adiabatic eigenvalues were calculated at ten different hyperradial points using 40, 60, 80 and 100 B-splines in each coordinate dimension. The convergence of our numerical potentials for values of ρ up to $\rho_{max} = 2 \times 10^4$ a.u. is indictated by the fact that the numerical values for the three-body effective potential energies are virtually unaffected by increasing the number of B-splines past $N_\theta = 80$. We also observe numerical convergence towards the universal constant $-s_0^2$ for $\rho \approx 1.5 \times 10^4$ a.u.

In Fig. 7.1 we show the results obtained over the full hyperradial range up to 2×10^4 a.u., where the numerically calculated three-body effective potentials $\xi(\rho)$ are plotted as functions of ρ. Note the logarithmic scale on the hyperradial axis. The curves can here be seen to converge towards the characteristic universal value $-s_0^2$ for $\rho \gg r_0$.

For all results presented in this chapter we were able to achieve convergence using a uniformly spaced mesh for hyperradii out to $\rho \approx 5 \times 10^3$ a.u. However, at larger hyperradii the two-body potential surface $V(\rho, \theta, \phi)$ changes much more rapidly near the coalescence points, i.e., at the hyperangular configurations $(\theta, \phi) = (\pi/2, \phi)$, $(\pi/2, \phi - 2\pi/3)$ and $(\pi/2, \phi - 2\pi/3)$. In Fig. 6.2 the two-body potential surfaces are plotted at two different hyperradii to illustrate how the size of the system changes the numerical complexity. To account for the increased numerical difficulties with increasing system size, the grid was more densely packed near the boundary $(\theta, \phi) = (\pi/2, \pi/3)$ for $\rho > 5 \times 10^3$ a.u. By doing this, we were able to achieve convergence out to $\rho \approx 2 \times 10^4$ a.u. and we can probably get convergence out to even larger ρ by further improving the knot point distribution on the grid.

Next, we consider the near-resonant scenario for finite a. For short-

a (a.u.)	N_θ	$\xi(\rho = 10$ a.u.$)$	$\xi(100$ a.u.$)$	$\xi(1000$ a.u.$)$	$\xi(5000$ a.u.$)$	$\xi(10000$ a.u.$)$
a_1	40	3.77527814	-2.60368386	-1.13917612	-1.03381510	-1.01875934
a_1	60	3.77527815	-2.60368387	-1.13917795	-1.03402416	-1.01912287
a_1	80	3.77527829	-2.60368372	-1.13917758	-1.03402814	-1.01913548
a_1	100	3.77530687	-2.60367682	-1.13917744	-1.03405123	-1.01907622
a_2	40	3.77526187	-2.60416379	-1.14059416	-1.04035561	-1.03170806
a_2	60	3.77526187	-2.60416379	-1.14058505	-1.04056429	-1.03207319
a_2	80	3.77526202	-2.60416364	-1.14059531	-1.04056828	-1.03208588
a_2	100	3.77526910	-2.60416170	-1.14059544	-1.04056460	-1.03224690

a (a.u.)	N_θ	$\xi(14900$ a.u.$)$	$\xi(15000$ a.u.$)$	$\xi(16000$ a.u.$)$	$\xi(18000$ a.u.$)$	$\xi(20000$ a.u.$)$
a_1	40	-1.01212794	-1.01201907	-1.01096344	-1.00898721	-1.00713887
a_1	60	-1.01250002	-1.01239205	-1.01134995	-1.00943386	-1.00768456
a_1	80	-1.01251258	-1.01240463	-1.01136253	-1.00944703	-1.00770029
a_1	100	-1.01252039	-1.01240591	-1.01136323	-1.00944484	-1.00769736
a_2	40	-1.03136024	-1.03137963	-1.03160655	-1.03219548	-1.03291215
a_2	60	-1.03173469	-1.03175499	-1.03199569	-1.03264544	-1.03346237
a_2	80	-1.03174732	-1.03176769	-1.03200835	-1.03265878	-1.03347809
a_2	100	-1.03174824	-1.03176640	-1.03200773	-1.03265632	-1.03347886

Table 7.1: Three-body effective potential energy values $\xi(\rho)$ at different hyperradii for $a_1 = -2702020$ a.u. and $a_1 = 1966590$ a.u. The potential for $a < 0$ has converged, while the potential for $a > 0$ tends to converge to the universal value $-s_0^2 \simeq -1.01251$ at hyperradii close to $\rho = 15000$ a.u.

ranged two-body potentials where the magnitude of the scattering length is large but finite we expect that the effective potentials $W_\nu(\rho)$ are to some extent affected by Efimov physics in the range $r_0 \ll \rho \ll |a|$ and that the lowest effective potentials obtained with a larger magnitude of a exhibit closer resemblence with the true Efimov potential given in Eq. (7.1). However, in the asymptotic limit $\rho \to \infty$, when $\rho \ll |a|$ is not fulfilled, we anticipate that the behaviour of $W_\nu(\rho)$ depends on the sign of a, since it indicates whether or not the two-body interaction is strong enough to support a binary state and henceforth indicates the associated break-up channel. For $a > 0$ the effective potentials $W_\nu(\rho)$ are expected to converge asymptotically to the energy of the weakly bound dimer (4.35). For $a < 0$ we instead expect that the effective potentials $W_\nu(\rho)$ asymptotically approach (4.34), i.e., the eigenvalues of the kinetic energy, which for the lowest potential $\xi(\rho)$ corresponds to $\lambda(\lambda + 4) + 4$ with $\lambda = 0$.

In Fig. 7.2 the potential curves for $a > 0$, asymptotically associated with the weakly bound dimer channel $\nu = 0$, are plotted as functions of the
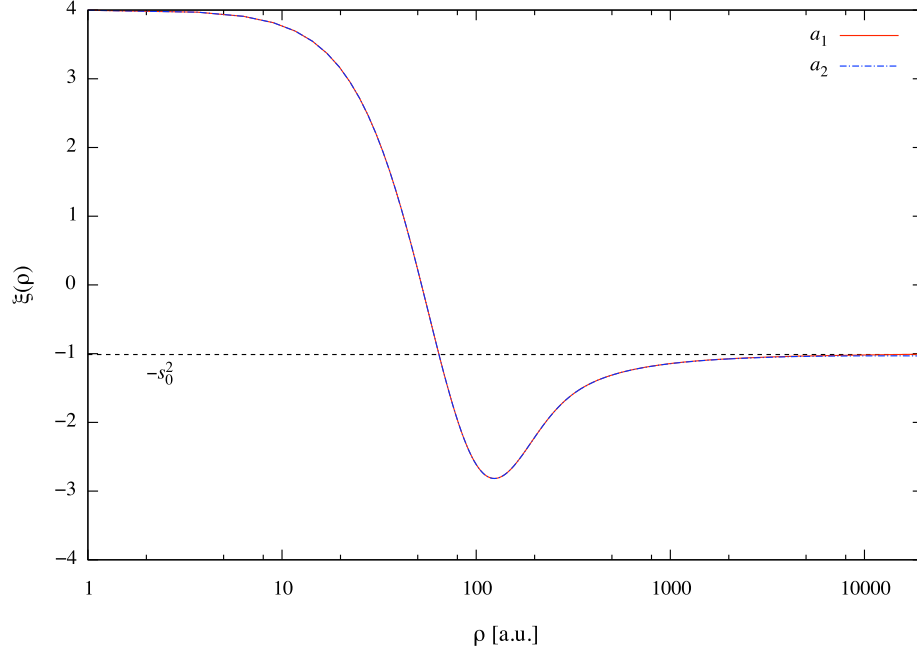
Figure 7.1: The lowest three-body effective potential curves $\xi(\rho)$ are plotted as functions of ρ for $a_1 = -2702020$ a.u. and $a_1 = 1966590$ a.u. over the full range of hyperradii for which the numerically calculated potentials converged.

hyperradius ρ for four different values of a. The results presented in this figure were obtained using values of d that approached pole I from the right, thus supporting a single two-body bound state. The Efimov-like character of the three-body effective potentials is manifested by the flattening behaviour of the curves over an extended region in the intermediate range $r_0 \ll \rho \ll |a|$, which tend to converge towards the universal value $-s_0^2$ (indicated in the figure by the horizontal dashed line), as the magnitude of the scattering length is gradually increased. The asymptotic convergence of the effective potentials $W_\nu(\rho)$ to the channel of one weakly bound dimer and a free atom can in this figure be recognized by $\xi(\rho)$ displaying a parabolic dependence on ρ in the asymptotic limit for each state. We highlight this behaviour for the two effective potentials obtained with the smallest values of a in Fig. 7.3 by including the two asymptotic forms $\xi_+ = 2\mu\rho^2 E_{2b} + 1/4$, calculated from the two-body energy E_{2b} given in Eq. (6.5).

In Fig. 7.4 the potential curves for $a < 0$, asymptotically associated with the lowest continuum channel, are plotted as functions of the hyperradius
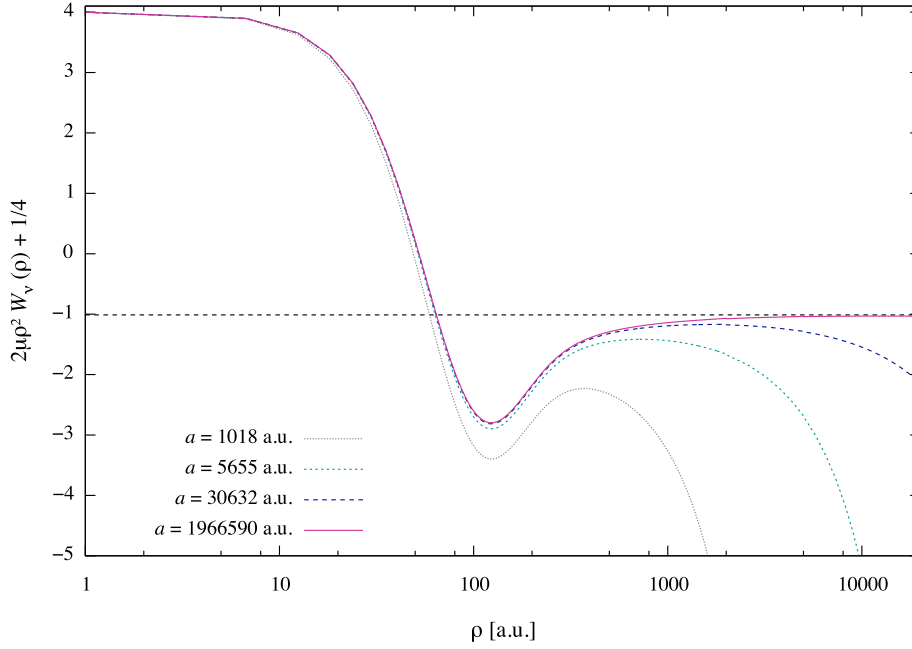
Figure 7.2: Three-body effective potentials for $a > 0$. The horizontal dashed line is the universal value $-s_0^2$, which the Efimov potential takes on for $\rho \gg r_0$.

ρ again for four different values of a. These three-body effective potentials also exhibit Efimov-like characteristics in the range $r_0 \ll \rho \ll |a|$, which can be discerned from the tendency of the potential curves to converge to $-s_0^2$ as the magnitude of a increases, while they return to the kinetic energy in the asymptotic limit.

To further investigate the validity of the code we now compare our numerically calculated three-body effective potentials $\xi(\rho)$ for a number of finite a states with the lowest energy eigenvalues $\nu_n(\rho)$ of the adiabatic hyperangular Faddeev equation for $a > 0$ and $a < 0$. These eigenvalues can be derived analytically in the limit of large $|a|$ over the full hyperradial range and are determined by solving the transcendental equation (4.56). The adiabatic eigenvalues $\nu_n(\rho)$ of Eq. (4.54) are related to the three-body effective potentials calculated in this work through Eq. (4.55).

In Fig. 7.5 we present the lowest eigenvalues $\nu_0(\rho/|a|)$ calculated from Eq. (4.56) for $a > 0$ and $a < 0$. For both positive and negative a, the adiabatic states converge to the universal value $\nu_0(0) = -s_0^2$ in the region where $\rho/|a|$ is small. For large $\rho/|a|$, however, we observe that $\nu_0(\rho/|a|)$ for
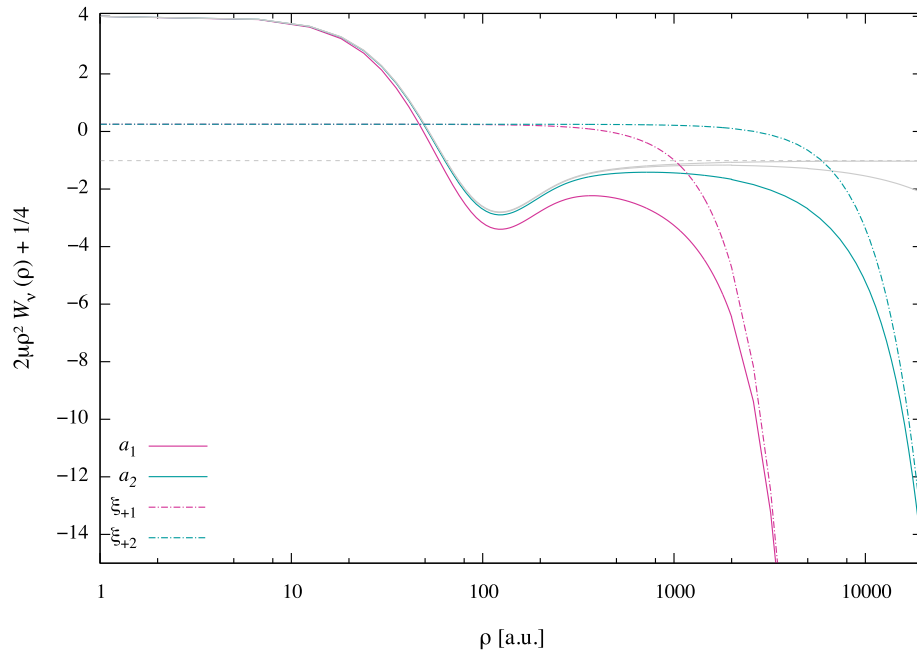
Figure 7.3: Three-body effective potentials for $a_1 = 1018$ a.u. and $a_2 = 5655$ a.u. are highlighted and shown together with their analytical asymptotic forms ξ_{+1} and ξ_{+2}. The grey horizontal dashed line is the universal value $-s_0^2$.
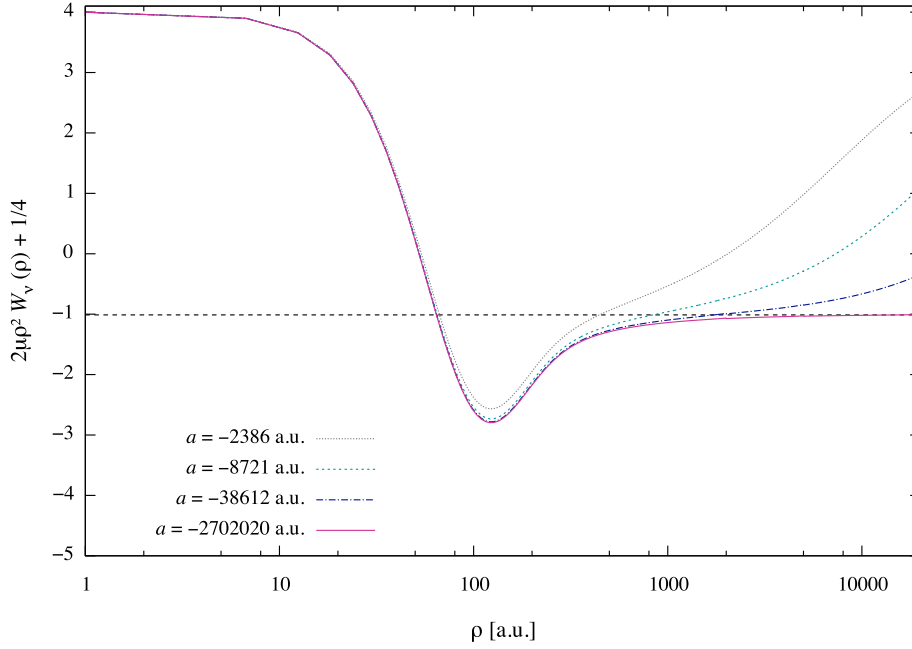
Figure 7.4: Three-body effective potentials for $a < 0$. The horizontal dashed line is the universal value $-s_0^2$.

$a > 0$ takes on a parabolic asymptotic form, which corresponds to a state with one diatomic molecule and one free atom, whereas for $a < 0$ the state can be seen to approach $\nu_0 = 4$, thus corresponding to the lowest kinetic energy eigenvalue for three free atoms.

In Fig. 7.6 we show the numerical three-body effective potentials $\xi(\rho)$ plotted as functions of $\rho/|a|$ for four different a in comparison with the analytical eigenvalues $\nu_0(\rho/|a|)$. The calculations were performed using an increasingly refined mesh and a hyperradial grid with 250 points. Each potential was obtained using an equal number of B-splines in each hyperangular coordinate ($N_\theta = N_\phi$). The effective potentials in the upper two panels are shown for (a) $a = -2385$ a.u. and (b) $a = -8720$ a.u., together with the analytically derived eigenvalues $\nu_0(\rho/|a|)$ of Eq. (4.54) for $a < 0$ (the dashed black lines in the upper panels). The hyperradial range, for which the numerical potentials converge to the analytical potential, can be seen to increase as a function of mesh resolution. For the state where the magnitude of a is smaller, we observe that the hyperradial range, over which the numerical potentials converge towards the analytical values, is larger.
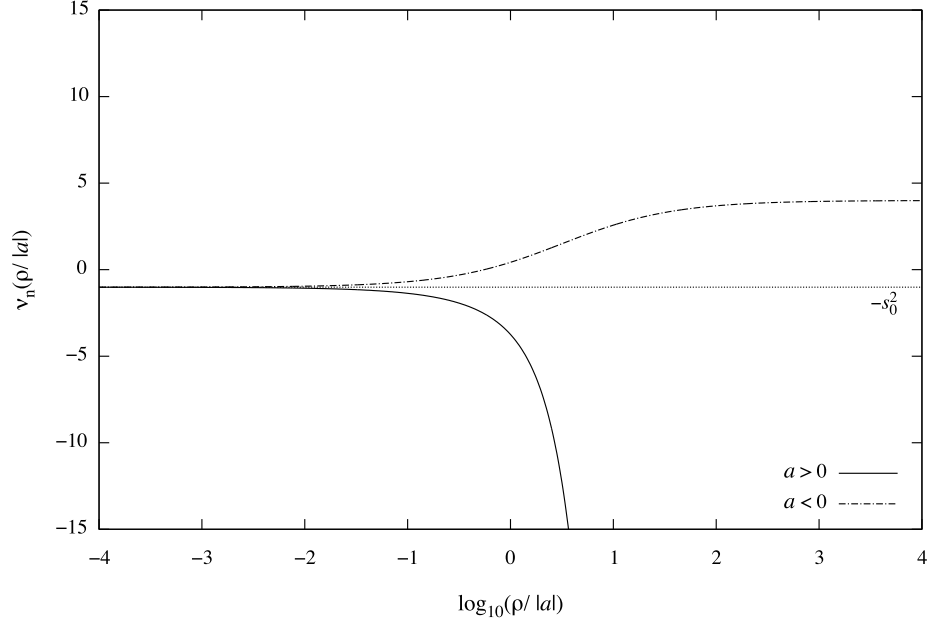
Figure 7.5: Eigenvalues $\nu_0(\rho/|a|)$ of the hyperangular Faddeev equation (4.54), for $a > 0$ (the solid line) and $a < 0$ (the dash-dotted line).

For the potentials calculated using the mesh with a total of 40^2 B-splines, convergence out to $\rho/|a| \approx 40$ and 8 can be seen in (a) and (b), respectively.

The calculations for positive a are shown in the lower two panels in Fig. 7.6, together with the analytically derived eigenvalues $\nu_0(\rho/|a|)$ for $a > 0$ (the solid black lines in the lower panels). Panel (c) contains the three-body effective potentials $\xi(\rho)$ for $a = 1018$ a.u. Here we observe that the convergent behaviour of $\xi(\rho)$ deviates from the effective potential $\nu_0(\rho/|a|)$. The slightly different form in the parabolic divergency of the curves is due to a discrepancy between the exact two-body energy E_{2b}, which is given in Eq. (6.5), and the energy of the universal shallow dimer $-E_D = -1/ma^2$. To illustrate this more clearly we have in Fig. 7.7 written the adiabatic potentials $\nu_n(\rho)$ on the form

$$\widetilde{W}_n(\rho) = \frac{\nu_n(\rho) - 1/4}{2\mu\rho^2}, \tag{7.2}$$

and plotted the three-body effective Faddeev potential $\widetilde{W}_0(\rho)$, together with the numerically calculated three-body effective potentials $W_0(\rho)$, as func-

tions of ρ/a. The numerical potentials can be seen to converge to the exact energy of the binary subsystem (a dashed black line marked E_{2b} in the figure), while the Faddeev potential approaches the approximate energy of the universal dimer (a dashed black line marked $-E_D$ in the figure). Since the binding energy of the universal dimer is exact in the resonant limit $a \to \infty$, we expect that the discrepancy between the analytic and the numerical curves is reduced if a is increased. In panel (d) in Fig. 7.6 we show that the potential curves for $a = 5655$ a.u. are converging, as the number of B-splines is increased, to a parabolically divergent curve more similar to $\nu_0(\rho/|a|)$. The corresponding effective potentials $W_0(\rho)$ and $\widetilde{W}_0(\rho)$ are shown as functions of ρ/a in Fig. 7.8, where we observe that the gap between the two curves in the asymptotic region is significantly smaller than the gap shown in Fig. 7.7.

By comparing the left and right panels in Fig. 7.6 it appears that the hyperradial range for convergence generally is larger for the states with smaller $|a|$. We suspect that this discrepancy is due to the knot point placement, but this has not been verified yet.

In the following we will look closer into the structure of the Efimov-like effective potentials $W_\nu(\rho)$ for cases where a is finite and when $a \to \pm\infty$. From Eq. (4.37) it is possible to predict the number of Efimov trimers that can be formed for each potential setting. With the current interaction range the magnitude of the scattering length needs to be larger than ~ 1250 a.u. to anticipate at least one Efimov state. For illustrative purposes, however, we show two cases where $|a| \sim 200$ a.u., since these exemples in a clear way show the Efimov-like features of the potentials.

The adiabatic potential curves shown in Fig. 7.9 were numerically calculated with a potential strong enough to support a single s-wave bound state and the potential depth d was tuned to yield a scattering length of $a = 252$ a.u. The adiabatic potential curves $W_\nu(\rho)$ with $\nu = 0 - 4$ are plotted as functions of the hyperradius ρ/a, where the Efimov channel is the lowest potential curve with channel index $\nu = 0$, which in the asymptotic region $\rho/a \gtrsim 1$ converges to the two-body s-wave binding energy. All higher lying channels $\nu > 1$ are repulsive everywhere and correspond to three-body continuum channels. As the potential depth parameter d is moved towards pole I from the right and $a \to \infty$ the energy of the two-body bound state vanishes and the Efimov channel becomes a purley attractive ρ^{-2} potential
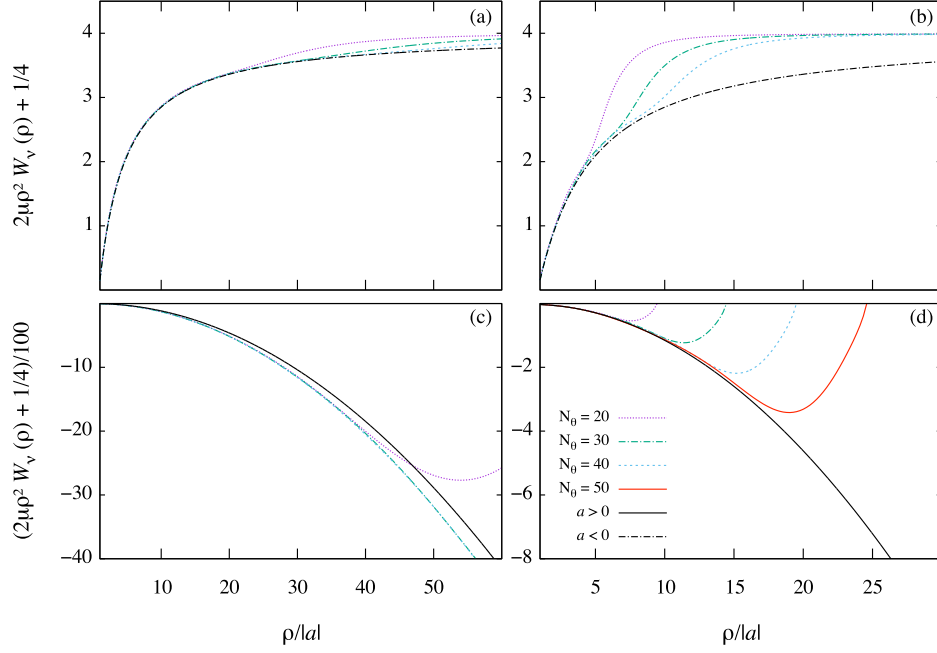
Figure 7.6: Three-body effective potentials $\xi(\rho)$, calculated using an increasing number of B-splines, are plotted as functions of $\rho/|a|$. In the upper two panels we show the potentials for (a) $a = -2385$ a.u. and (b) $a = -8720$ a.u., together with the analytic eigenvalues $\nu_0(\rho/|a|)$ of Eq. (4.54) for $a < 0$ (the black dash-dotted lines). In the lower two panels we show the potentials for (c) $a = 1018$ a.u. and (d) $a = 5655$ a.u. together with $\nu_0(\rho/|a|)$ for $a > 0$ (the black solid lines). The numerically calculated potentials shown in panel (d) appear to approximately converge to $\nu_0(\rho/|a|)$, while the potentials for $a = 1018$ a.u. in panel (c) can be seen to converge to a slightly different form than $\nu_0(\rho/|a|)$.

Figure 7.7: Three-body effective potentials $W_0(\rho)$ and $\widetilde{W}_0(\rho)$ for $a = 1018$ a.u. are plotted as functions of ρ/a. The numerically calculated potentials $W_0(\rho)$ can be seen to converge asymptotically to the exact two-body bound energy E_{2b}, while the analytically derived potential $\widetilde{W}_0(\rho)$ approaches the approximate energy of the universal dimer $-E_D$.
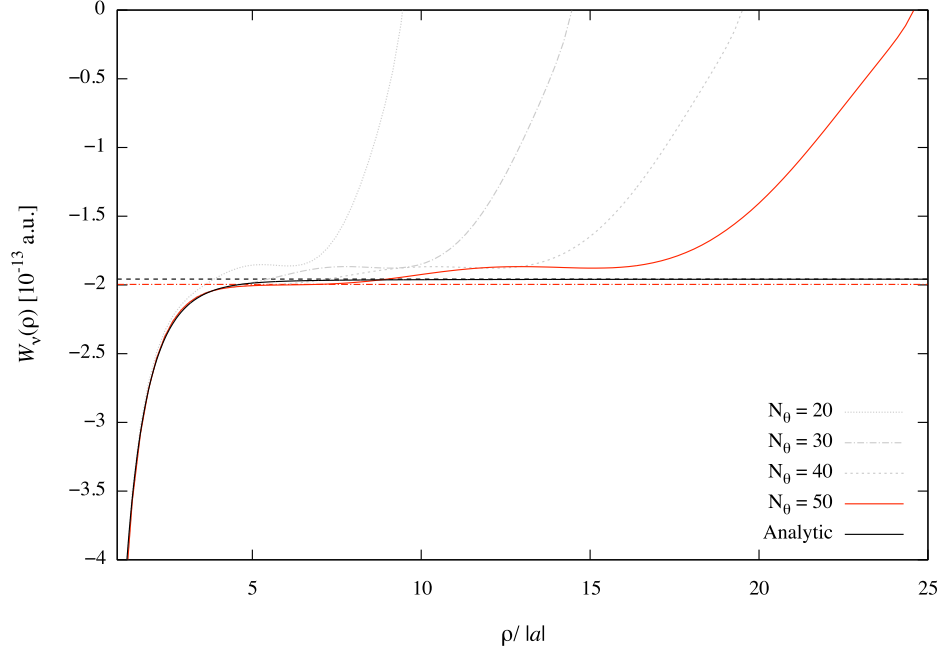
Figure 7.8: Three-body effective potentials $W_0(\rho)$ and $\widetilde{W}_0(\rho)$ for $a = 5655$ a.u.
are plotted as functions of ρ/a. The numerical potential $W_0(\rho)$ calculated with
$N_\theta = 50$ is highlighted in red and can be seen to converge asymptotically to the
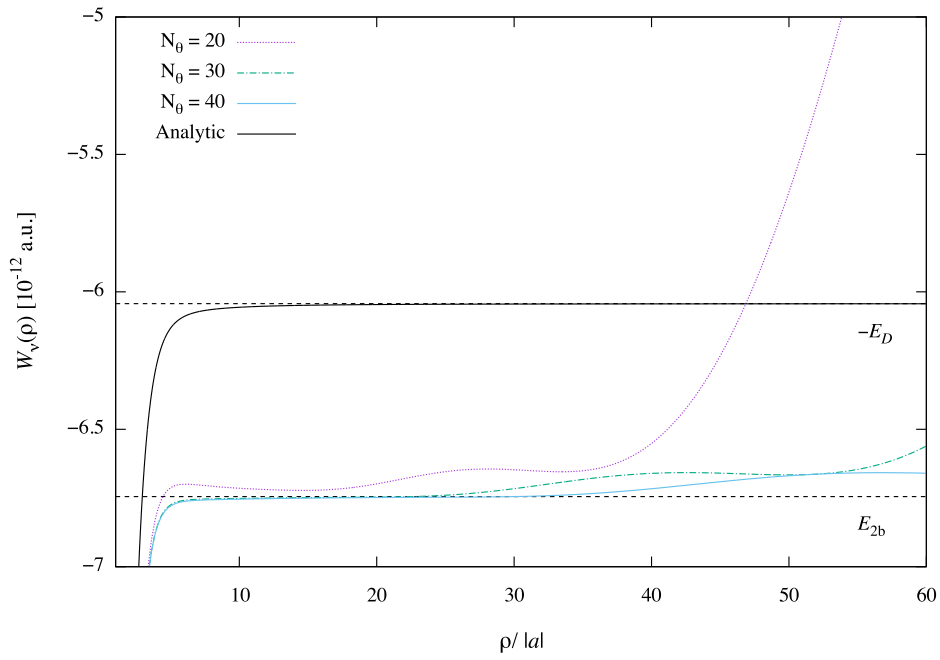exact two-body bound energy E_{2b} (the dash-dotted red line), while the effective
potential $\widetilde{W}_0(\rho)$ approaches the approximate energy of the universal dimer $-E_D$
(the dashed black line).

for $\rho > r_0$.

Similarly, in Fig. 7.10 the adiabatic potential curves for $a < 0$ with
$\nu = 0 - 4$ is shown. The potential depth d was in this case tuned to yield a
scattering length of $a = -224$ a.u. The lowest potential curve with channel
index $\nu = 0$, which asymptotically converges to the three-body continuum,
corresponds to the Efimov channel. In this case, the three-body interaction
has a potential barrier with a maximum located at $\rho/|a| \approx 2$, while in the
intermediate range $r_0 \lesssim \rho \lesssim a$ the potential is attractive. A magnification
of the barrier region is shown in the inset in Fig. 7.10.

In Fig. 7.11 we show the effective potentials calculated with increasing
values of d starting from the left-hand side ($a < 0$) and ending on the right-
hand side ($a > 0$) of pole I. The potentials calculated for $a < 0$ are here
shown in blue, while the ones calculated for $a > 0$ are shown in red.
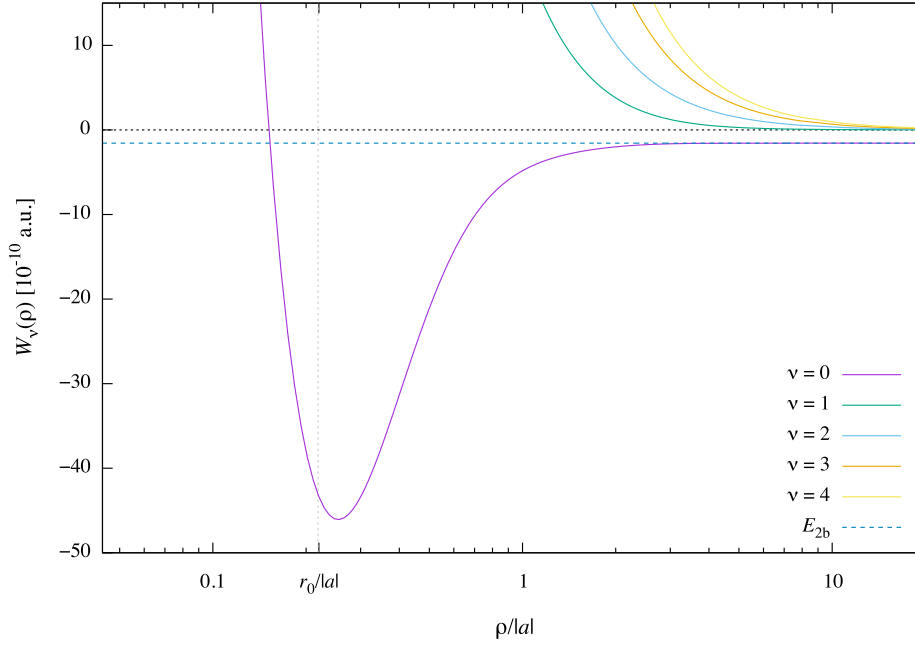
Figure 7.9: Three-body effective potentials for $a = 252$ a.u. The horizontal blue dashed line is the energy of the dimer.

A common feature for all Efimov-like effective potentials with negative scattering lengths is the kind of centrifugal barrier [40], with a long-range maximum, which we observed earlier in Fig. 7.10. For the three-body wave function incident from $\rho \to \infty$ to get to the region $\rho < |a|$, it must tunnel through this barrier. The presence of a centrifugal barrier indicates that it is possible to have a trimer shape resonance at $E > 0$ for certain negative values of a. A shape resonance is a long-lived metastable state in which the three-body system is trapped in the region $\rho < |a|$ due to the shape of the potential barrier. If the three-body wave tunnels through the barrier and the formed metastable state allows for the three atoms to be close to each other for an extended period of time before they fly apart, there is an increased probability that the system will relax into a deeply bound dimer and a free atom, with the free atom carrying away the excess kinetic energy. When the energy of the incident trimer matches a resonance, there is an enhanced barrier penetrability to form an Efimov resonance, which will cause an increased probability of the formation of deeply bound dimer states and high energy free atoms. Thus, in collision experiments with a

Figure 7.10: Three-body effective potentials for $a = -224$ a.u. The potential $\nu = 0$ has a potential barrier with a maximum located at $\rho/|a| \approx 2$ (shown magnified in the inset).

trapped gas of ultracold atoms with tunable interactions, this recombination mechanism can cause resonantly enhanced atom losses at certain values of a due to a sudden increase in the 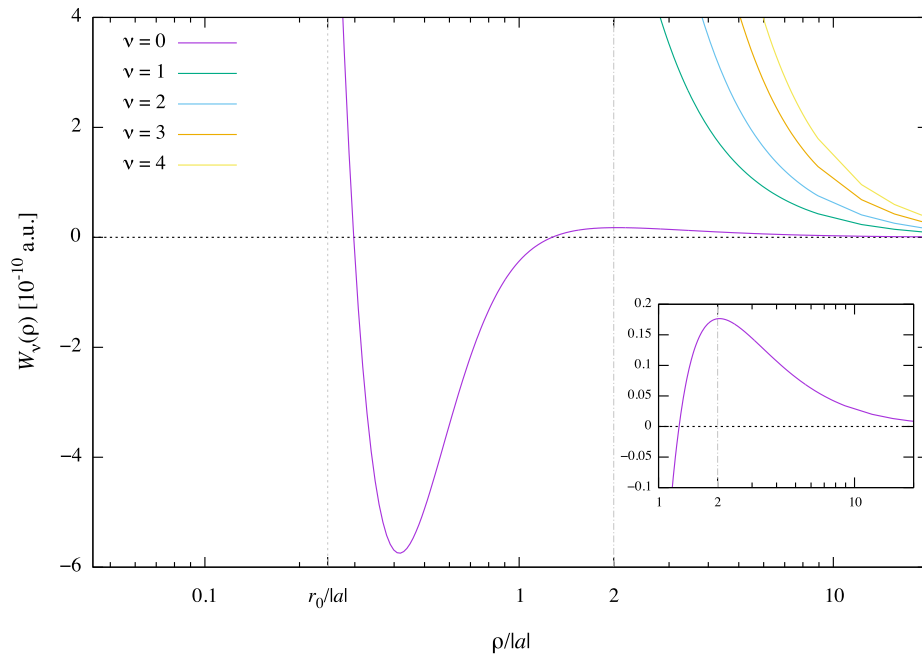formation of atom-dimer states, because the energy conservation during the inelastic collision requires the binding energy released from the molecular formation to transform into kinetic energy of the relative motion between the dimer and the free atom, which subsequently causes them to escape the trap. This resonant enhancement of atom losses thus serves as a fingerprint of the elusive Efimov trimer states.

When d approaches the pole from the left and the value of $|a|$ increases, the position of the barrier in the Efimov channel moves to larger ρ, while the barrier height is reduced. This is illustrated in the upper and lower inset in Fig. 7.11, where we show that as the scattering length is changed, the position of the barrier maxima grows proportional to $|a|$ and moves to infinity when $a \to -\infty$, while the barrier height shrinks proportional to $1/a^2$ and vanishes at infinity. The ideal Efimov effect occurs when the barrier is at infinity, and hence has zero height, and none of the two-body subsystems are bound, or when a two-body subsystem of three particles supports a dimer at zero energy. This scenario is realized for states calculated with values of d very close to the pole.

In Fig. 7.11 we show that our numerically calculated potentials for $a \to \pm\infty$ (the potentials labelled a_3 and a_4 in the figure) are essentially the same, with an attractive $1/\rho^2$ character. After crossing the pole, a further increase in d will result in the typical asymptotic convergence towards the energy of the s-wave state just below the zero energy threshold (the potential labelled a_5), which will be shifted to lower energies as d grows (the potential labelled a_6).

In Fig. 7.12 we show that the repulsive barrier, characteristic for Efimov resonances, is present also in the analytically derived effective potentials $\widetilde{W}_0(\rho)$ for $a < 0$. The numerical and analytical potential curves for $a_1 = -224$ a.u. and $a_2 = -2385$ a.u. are here plotted as functions of ρ. In the inset we show that the barriers for the a_2 potentials are almost identical, with a maximum at $\rho \approx 2a_2$. There is a greater discrepancy for the a_1 potentials, as can be expected, since the analytical results are exact in the unitary limit $|a| \to \infty$.
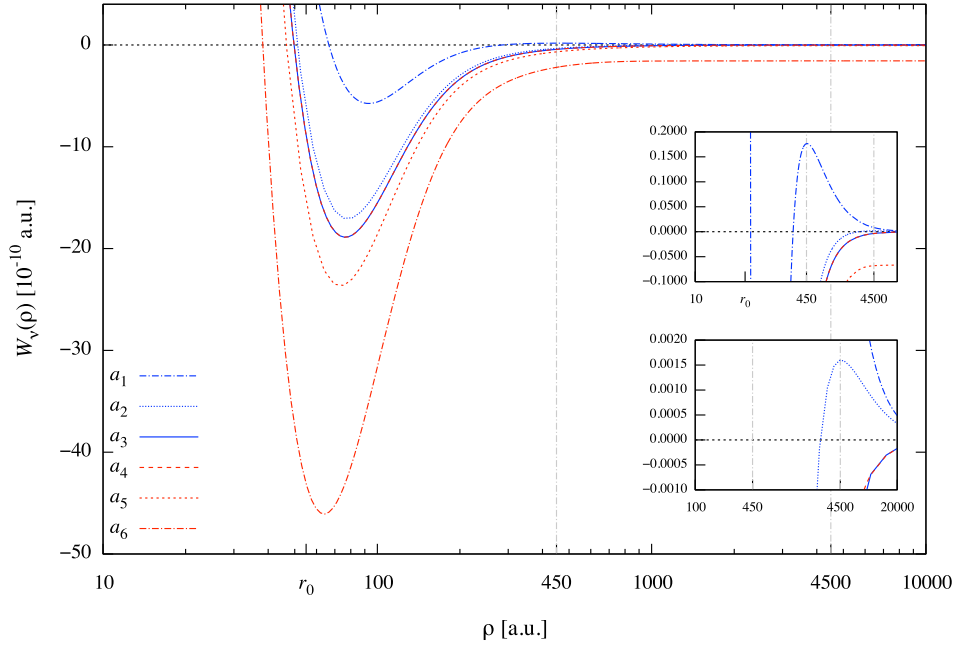
Figure 7.11: Three-body effective potentials calculated near pole I. For $a < 0$ the potentials are shown in blue, with $|a_i| = 224, 2385, 2702020$ a.u., where $i = 1, 2, 3$. For $a > 0$ the potentials are shown in red, with $a_i = 1966590, 1018, 252$ a.u., where $i = 4, 5, 6$. The upper inset shows the potential barrier for a_1 with a maximum located at $\rho \approx 450$ a.u. The lower inset shows the potential barrier for a_2 with a maximum located at $\rho \approx 4500$ a.u.
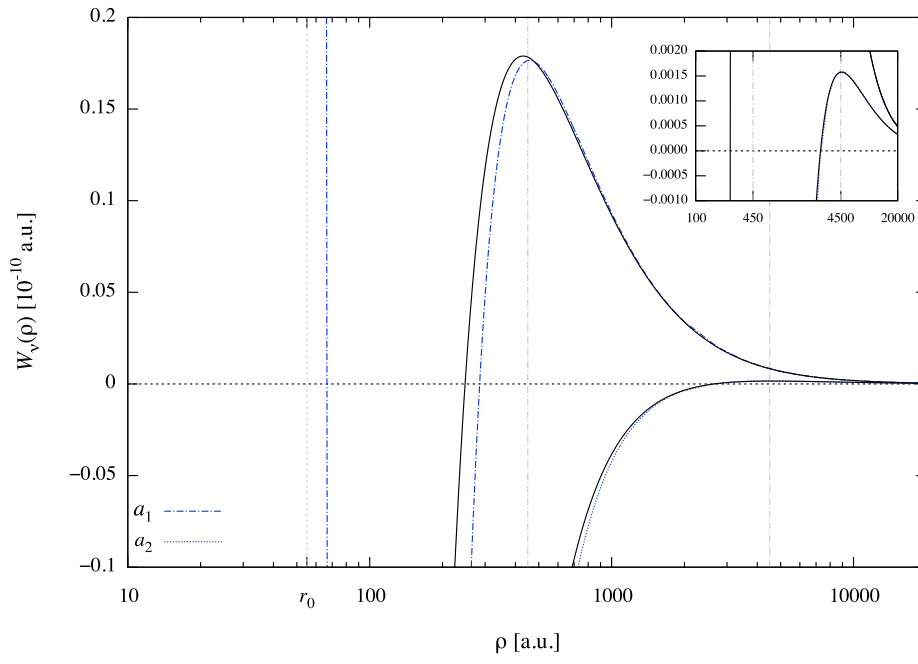
Figure 7.12: Three-body effective potentials $W_0(\rho)$ for $a_1 = -224$ a.u. and $a_2 = -2385$ a.u. are shown in blue together with the corresponding analytic potentials $\widetilde{W}_0(\rho)$, which are shown in black.

Chapter 8

Outlook

Chapter 9

Outlook

Appendix A

Hyperspherical Coordinates

This appendix contains mapping procedures, derivations and implementation details for Chapter 4. Some of the definitions presented in Section 4.1 will be repeated here in order for this appendix to be complete.

Let $\mathbf{x}_i$ and m_i be the position vector and mass of the ith particle in the laboratory frame. If the total mass M, the three particle reduced mass μ, and the normalizing constants d_k $(k = 1, 2, 3)$ are given by

$$M = \sum_{i=1}^{3} m_i, \tag{A.1}$$

$$\mu^2 = \frac{1}{M} \prod_{i=1}^{3} m_i, \tag{A.2}$$

$$d_k^2 = \frac{m_k}{\mu} \frac{(m_i + m_j)}{M}, \tag{A.3}$$

then the set of mass-scaled Jacobi vectors and the center of mass coordinate can be defined as

$$\mathbf{r}_k = d_k^{-1}(\mathbf{x}_j - \mathbf{x}_i), \tag{A.4}$$

$$\mathbf{R}_k = d_k \left[\mathbf{x}_k - \frac{(m_i \mathbf{x}_i + m_j \mathbf{x}_j)}{m_i + m_j} \right], \tag{A.5}$$

$$\mathbf{X}_{CM} = \frac{1}{M} \sum_{i=1}^{3} m_i \mathbf{x}_i, \tag{A.6}$$

in which, the indices i, j, k are cyclic permutations of $(1, 2, 3)$. The center-of-mass is separated out and will not be considered further. Transformations within the set of coordinates is aided by defining the angle β_{ij}, which have the following properties

$$\beta_{ij} = -\beta_{ji}, \quad \beta_{ii} = 0, \tag{A.7a}$$

$$\tan \beta_{ij} = -m_k/\mu, \tag{A.7b}$$

$$d_i d_j \sin \beta_{ij} = 1, \tag{A.7c}$$

$$d_i d_j m_k \cos \beta_{ij} = -\mu, \tag{A.7d}$$

$$\beta_{12} + \beta_{23} + \beta_{31} = 2\pi. \tag{A.7e}$$

Orthogonal transformations are then given by

$$\begin{pmatrix} \mathbf{r}_j \\ \mathbf{R}_j \end{pmatrix} = \begin{pmatrix} \cos \beta_{ij} & \sin \beta_{ij} \\ -\sin \beta_{ij} & \cos \beta_{ij} \end{pmatrix} \begin{pmatrix} \mathbf{r}_i \\ \mathbf{R}_i \end{pmatrix}. \tag{A.8}$$

A.1   Delves Coordinates

This section contains the detailed derivation of the three-body Schrödinger equation written in Delves coordinates. The coordinate definitions are the same as in Section 4.4.1. Here we simply repeat some previously stated definitions for a clearer overview. The Jacobi vectors in each coordinate set are defined by

$$r_k = \rho \sin \alpha_k, \tag{A.9a}$$

$$R_k = \rho \cos \alpha_k \tag{A.9b}$$

and the Delves hyperangle α_k is defined by

$$\alpha_k = \arctan \left(\frac{r_k}{R_k} \right), \quad 0 \leq \alpha_k \leq \frac{\pi}{2}. \tag{A.10}$$

The other angle in this coordinate set is the angle between the two vectors $\mathbf{r}_k$ and $\mathbf{R}_k$, which is given by

$$\cos \theta_k = \frac{\mathbf{r}_k \cdot \mathbf{R}_k}{r_k R_k}, \quad 0 \leq \theta \leq \pi. \tag{A.11}$$

We choose one arbitary set to work in and suppress the indices from hereon. The mass weighted Schrödinger equation for the stationary wavefunction Ψ of a three-body system – with position vectors $\mathbf{x}_i$ and masses m_i, $(i = 1, 2, 3)$ – interacting pairwise through a potential V, is given by

$$-\frac{1}{2} \sum_{i=1}^{3} m_i^{-1} \nabla_i^2 \Psi + V\Psi = E\Psi. \tag{A.12}$$

Where ∇_i^2 is the Laplace operator for particle i, which in spherical coordinates reads

$$\nabla_i^2 = \frac{1}{r_i^2} \frac{\partial}{\partial r_i} \left(r_i^2 \frac{\partial}{\partial r_i} \right) - \frac{L_i^2}{r_i^2}, \tag{A.13}$$

in which L_i is the angular momentum operator associated with the vector $\mathbf{r}_i$.

The kinetic energy for three particles in the mass normalized Jacobi coordinates was given in Eq. (4.8). Thus, after separating out the center-of-mass coordinate, the Schrödinger equation for the internal motion is simply

$$-\frac{1}{2\mu} \left(\nabla_{\mathbf{r}}^2 + \nabla_{\mathbf{R}}^2 \right) \Psi + V\Psi = E\Psi. \tag{A.14}$$

For three identical particles, the squared orbital angular momentum operators associated with the Jacobi vectors are given by

$$L_r^2 = L_R^2 = -\frac{1}{\sin\theta} \frac{\partial}{\partial\theta} \left(\sin\theta \frac{\partial}{\partial\theta} \right). \tag{A.15}$$

Change of coordinates subsequently results in the following transformations for the partial derivatives of the vector $\mathbf{r}$

$$\frac{\partial}{\partial r} = \frac{\partial\alpha}{\partial r} \frac{\partial}{\partial\alpha} + \frac{\partial\rho}{\partial r} \frac{\partial}{\partial\rho} = \frac{1}{\rho} \cos\alpha \frac{\partial}{\partial\alpha} + \sin\alpha \frac{\partial}{\partial\rho}, \tag{A.16}$$

$$\begin{aligned}
\frac{\partial^2}{\partial r^2} &= \left(\frac{1}{\rho} \cos\alpha \frac{\partial}{\partial\alpha} + \sin\alpha \frac{\partial}{\partial\rho} \right) \left(\frac{1}{\rho} \cos\alpha \frac{\partial}{\partial\alpha} + \sin\alpha \frac{\partial}{\partial\rho} \right) \\
&= \frac{1}{\rho^2} \cos^2\alpha \frac{\partial^2}{\partial\alpha^2} - \frac{1}{\rho^2} \sin(2\alpha) \frac{\partial}{\partial\alpha} + \sin^2\alpha \frac{\partial^2}{\partial\rho^2} \\
&\quad + \frac{1}{\rho} \cos^2\alpha \frac{\partial}{\partial\rho} + \frac{1}{\rho} \sin(2\alpha) \frac{\partial^2}{\partial\alpha\partial\rho}.
\end{aligned} \tag{A.17}$$

Similarly, the partial derivatives with respect to the vector $\mathbf{R}$ transform as

$$\frac{\partial}{\partial R} = \frac{\partial \alpha}{\partial R}\frac{\partial}{\partial \alpha} + \frac{\partial \rho}{\partial R}\frac{\partial}{\partial \rho} = -\frac{1}{\rho}\sin\alpha\frac{\partial}{\partial \alpha} + \cos\alpha\frac{\partial}{\partial \rho}, \tag{A.18}$$

$$\begin{aligned}
\frac{\partial^2}{\partial R^2} &= \left(-\frac{1}{\rho}\sin\alpha\frac{\partial}{\partial \alpha} + \cos\alpha\frac{\partial}{\partial \rho}\right)\left(-\sin\alpha\frac{\partial}{\partial \alpha} + \cos\alpha\frac{\partial}{\partial \rho}\right) \\
&= \frac{1}{\rho^2}\sin^2\alpha\frac{\partial^2}{\partial \alpha^2} + \frac{1}{\rho^2}\sin(2\alpha)\frac{\partial}{\partial \alpha} + \cos^2\alpha\frac{\partial^2}{\partial \rho^2} \\
&\quad + \frac{1}{\rho}\sin^2\alpha\frac{\partial}{\partial \rho} - \frac{1}{\rho}\sin(2\alpha)\frac{\partial^2}{\partial \alpha \partial \rho}.
\end{aligned} \tag{A.19}$$

Finally, the sum of the two Laplacian operators now reads

$$\begin{aligned}
\nabla_{\mathbf{r}}^2 + \nabla_{\mathbf{R}}^2 &= \frac{2}{r}\frac{\partial}{\partial r} + \frac{2}{R}\frac{\partial}{\partial R} + \frac{\partial^2}{\partial r^2} + \frac{\partial^2}{\partial R^2} - \frac{L_r^2}{r^2} - \frac{L_R^2}{R^2} \\
&= \frac{4}{\rho^2}\cot(2\alpha)\frac{\partial}{\partial \alpha} + \frac{5}{\rho}\frac{\partial}{\partial \rho} + \frac{1}{\rho^2}\frac{\partial^2}{\partial \alpha^2} + \frac{\partial^2}{\partial \rho^2} \\
&\quad + \frac{4}{\rho^2\sin^2(2\alpha)\sin(\theta)}\frac{\partial}{\partial \theta}\left(\sin(\theta)\frac{\partial}{\partial \theta}\right) \\
&= \frac{1}{\rho^5}\frac{\partial}{\partial \rho}\left(\rho^5\frac{\partial}{\partial \rho}\right) + \frac{1}{\rho^2\sin^2(2\alpha)}\left(\frac{\partial}{\partial \alpha}\sin^2(2\alpha)\frac{\partial}{\partial \alpha} + \frac{4}{\sin\theta}\frac{\partial}{\partial \theta}\right).
\end{aligned} \tag{A.20}$$

The original Hamiltonian operator written in Delves coordinates can thus be expressed as

$$H_0 = T_\rho + T_\alpha + T_\theta + V(\rho, \Omega). \tag{A.21}$$

Anticipating a rescaling of the wave function for subsequent removal of first derivatives with respect to ρ and α warrants us to write the kinetic energy operators in the original Hamiltonian in the following ways: Let the hyperradial kinetic energy operator T_ρ be expressed as

$$\begin{aligned}
T_\rho &= -\frac{1}{2\mu}\left[\frac{1}{\rho^5}\frac{\partial}{\partial \rho}\left(\rho^5\frac{\partial}{\partial \rho}\right)\right] \\
&= -\frac{1}{2\mu}\left[\rho^{-5/2}\left(\rho^{5/2}\frac{5}{\rho}\frac{\partial}{\partial \rho} + \rho^{5/2}\frac{\partial^2}{\partial \rho^2}\right)\rho^{-5/2}\rho^{5/2}\right] \\
&= -\frac{1}{2\mu}\rho^{-5/2}\left[-\frac{15}{4}\frac{1}{\rho^2} + \frac{\partial^2}{\partial \rho^2}\right]\rho^{5/2}
\end{aligned} \tag{A.22}$$

and let the kinetic energy operators for the hyperangles – that is, the kinetic energy operator for the Delves angle T_α and the kinetic energy operator for the angular momentum of the Jacobi vectors T_θ – be expressed as

$$
\begin{aligned}
T_\alpha &= -\frac{1}{2\mu}\frac{1}{\rho^2\sin^2(2\alpha)}\left[\frac{\partial}{\partial\alpha}\sin^2(2\alpha)\frac{\partial}{\partial\alpha}\right] \\
&= -\frac{1}{2\mu}\frac{1}{\rho^2}\left[\frac{\partial^2}{\partial\alpha^2}+4\cot(2\alpha)\frac{\partial}{\partial\alpha}\right] \\
&= -\frac{1}{2\mu}\frac{1}{\rho^2}\left[\sin^{-1}(2\alpha)\left(\sin(2\alpha)\frac{\partial^2}{\partial\alpha^2}+4\cos(2\alpha)\frac{\partial}{\partial\alpha}\right)\sin^{-1}(2\alpha)\sin(2\alpha)\right] \\
&= -\frac{1}{2\mu}\frac{1}{\rho^2}\sin^{-1}(2\alpha)\left[\frac{\partial^2}{\partial\alpha^2}+4\right]\sin(2\alpha),
\end{aligned}
\tag{A.23}
$$

and

$$
\begin{aligned}
T_\theta &= -\frac{1}{2\mu}\left[\frac{4}{\rho^2\sin^2(2\alpha)\sin\theta}\frac{\partial}{\partial\theta}\left(\sin\theta\frac{\partial}{\partial\theta}\right)\right] \\
&= -\frac{1}{2\mu}\left[\frac{1}{\rho^2\sin^2\alpha\cos^2\alpha\sin\theta}\frac{\partial}{\partial\theta}\left(\sin\theta\frac{\partial}{\partial\theta}\right)\right]
\end{aligned}
\tag{A.24}
$$

respectively. Removal of first derivatives with respect to ρ and α is now possible by rescaling the total wave function such that $\Psi = \rho^{-5/2}(\sin(2\alpha))^{-1}\psi$. The corresponding transformation of the Hamiltonian is then

$$
\begin{aligned}
H &= \rho^{5/2}\sin(2\alpha)H_0\rho^{-5/2}(\sin(2\alpha))^{-1} \\
&= -\frac{1}{2\mu}\left[\frac{\partial^2}{\partial\rho^2}-\frac{15}{4\rho^2}+\frac{1}{\rho^2}\left(\frac{\partial^2}{\partial\alpha^2}+4+\frac{1}{\sin^2\alpha\cos^2\alpha\sin\theta}\frac{\partial}{\partial\theta}\left(\sin\theta\frac{\partial}{\partial\theta}\right)\right)\right] \\
&= -\frac{1}{2\mu}\left[\frac{\partial^2}{\partial\rho^2}+\frac{1}{\rho^2}\left(\frac{\partial^2}{\partial\alpha^2}+\frac{1}{\sin^2\alpha\cos^2\alpha\sin\theta}\frac{\partial}{\partial\theta}\left(\sin\theta\frac{\partial}{\partial\theta}\right)\right)+\frac{1}{4\rho^2}\right] \\
&= -\frac{1}{2\mu}\frac{\partial^2}{\partial\rho^2}+\frac{\Lambda^2-1/4}{2\mu\rho^2},
\end{aligned}
\tag{A.25}
$$

where Λ^2 contains all the hyperangular kinetic energy variables. The squared grand angular momentum is in this case given by

$$\Lambda^2 = -\frac{\partial^2}{\partial \alpha^2} - \frac{1}{\sin^2 \alpha \cos^2 \alpha \sin \theta} \frac{\partial}{\partial \theta} \left(\sin \theta \frac{\partial}{\partial \theta} \right). \qquad (A.26)$$

The Schrödinger equation can thus be written

$$\left(-\frac{1}{2\mu} \frac{\partial^2}{\partial \rho^2} + \frac{\Lambda^2 - 1/4}{2\mu\rho^2} + V(\rho, \alpha, \theta) \right) \psi(\rho, \alpha, \theta) = E\psi(\rho, \alpha, \theta), \qquad (A.27)$$

where E is the internal energy. The corresponding volume element is proportional to $\rho^5 \sin^2 \alpha \cos^2 \alpha \sin \theta \, d\rho \, d\alpha \, d\theta$. Since the rescaled wavefunction needs to be square-integrable for a bound state, the boundary conditions are given by

$$\psi(0, \alpha, \theta) = 0, \qquad (A.28)$$

$$\psi(\rho, 0, \theta) = \psi(\rho, \frac{\pi}{2}, \theta) = 0, \qquad (A.29)$$

$$\left. \frac{\partial \psi}{\partial \theta} \right|_{\theta=0} = \left. \frac{\partial \psi}{\partial \theta} \right|_{\theta=\pi} = 0. \qquad (A.30)$$

A.2 Modified Smith–Whitten Coordinates

A.2.1 Coordinate Mapping

Johnson has given a detailed description of how the three-body system can be represented in a symmetric way [34]. In this section we present the main procedures used to retrieve a mapping for the three-dimensional triatomic potential energy surface to a point in configuration space. This mapping will treat the different arrangement channels equally, which enables permutation symmetries for three identical particles to be imposed exactly. Performing a second mapping of the original representation presented in [26, 35] yields the resulting set of modified Smith-Whitten coordinates. The derivation of the Hamiltonian for this representation is then described in Appendix A.2.2.

To define a symmetric coordinate system, one starts by separating the external and internal coordinates of the configuration. For the external coordinates we use the Euler angles, these are used to relate rotations of the three-body system in space. Since the potential energy only depends on the internal coordinates we will focus on them here. The internal coordinates ρ,

Θ, and Φ_k determine the size, shape and particle arrangement of the triangle formed by the three-body system, respectively. Starting from the definition for the internal coordinates given by Smith and Whitten [35]

$$
\begin{aligned}
(\mathbf{r}_k)_x &= \rho \cos \Theta \cos \Phi_k, \\
(\mathbf{r}_k)_y &= -\rho \sin \Theta \sin \Phi_k, \\
(\mathbf{r}_k)_z &= 0 \\
(\mathbf{R}_k)_x &= \rho \cos \Theta \sin \Phi_k, \\
(\mathbf{R}_k)_y &= \rho \sin \Theta \cos \Phi_k, \\
(\mathbf{R}_k)_z &= 0,
\end{aligned}
\tag{A.31}
$$

where Φ_k is in the range $0 \leq \Phi_k < 2\pi$ and Θ is in the range $0 \leq \Theta \leq \pi/4$. The distances between the particles ij are related through

$$
r_{ij} = |\mathbf{x}_j - \mathbf{x}_i| = d_k |\mathbf{r}_k| = \frac{d_k \rho}{\sqrt{2}} \left[1 + \cos(2\Theta) \cos(2\Phi_k) \right]^{1/2}.
\tag{A.32}
$$

The kinematic rotations (A.8) correspond to the following transformation in hyperspherical space

$$
\Phi_j = \Phi_i - \beta_{ij}.
\tag{A.33}
$$

This is easily shown by performing transformations within the coordinate set. From now on, we choose $k = 3$ and transform all r_{ij} to the coordinates (ρ, Θ, Φ_3).

$$r_{12} = d_3 \mid \mathbf{r}_3 \mid = \frac{\rho d_3}{\sqrt{2}} \left[1 + \cos(2\Theta) \cos(2\Phi_3) \right]^{1/2}$$

$$r_{23} = d_1 \mid \mathbf{r}_1 \mid = \frac{d_1 \rho}{\sqrt{2}} \left[1 + \cos(2\Theta) \cos(2\Phi_1) \right]^{1/2}$$

$$= d_1 \left[\cos^2 \beta_{31} \mathbf{r}_3^2 + \sin^2 \beta_{31} \mathbf{R}_3^2 + 2 \sin \beta_{31} \cos \beta_{31} \mathbf{r}_3 \cdot \mathbf{R}_3 \right]^{1/2}$$

$$= \frac{d_1 \rho}{\sqrt{2}} \left[1 + \cos(2\Theta) \big(\cos(\Phi_3) \cos(2\beta_{31}) + \sin(2\Phi_3) \sin(2\beta_{31}) \big) \right]^{1/2}$$

$$= \frac{d_1 \rho}{\sqrt{2}} \left[1 + \cos(2\Theta) \cos(2\Phi_3 - 2\beta_{31}) \right]^{1/2}$$

$$r_{31} = d_2 \mid \mathbf{r}_2 \mid = \frac{d_2 \rho}{\sqrt{2}} \left[1 + \cos(2\Theta) \cos(2\Phi_2) \right]^{1/2}$$

$$= d_2 \left[\cos^2 \beta_{23} \mathbf{r}_3^2 + \sin^2 \beta_{23} \mathbf{R}_3^2 - 2 \sin \beta_{23} \cos \beta_{23} \mathbf{r}_3 \cdot \mathbf{R}_3 \right]^{1/2}$$

$$= \frac{d_2 \rho}{\sqrt{2}} \left[1 + \cos(2\Theta) \big(\cos(\Phi_3) \cos(2\beta_{23}) - \sin(2\Phi_3) \sin(2\beta_{23}) \big) \right]^{1/2}$$

$$= \frac{d_2 \rho}{\sqrt{2}} \left[1 + \cos(2\Theta) \cos(2\Phi_3 + 2\beta_{23}) \right]^{1/2}.$$

$$(A.34)$$

By defining

$$\epsilon_1 = -2 \tan^{-1}(-m_2/\mu)$$
$$\epsilon_2 = 2 \tan^{-1}(-m_1/\mu). \tag{A.35}$$

These the distances are given by

$$r_{12} = \frac{d_3 \rho}{\sqrt{2}} \left[1 + \cos(2\Theta) \cos(2\Phi) \right]^{1/2}$$

$$r_{23} = \frac{d_1 \rho}{\sqrt{2}} \left[1 + \cos(2\Theta) \cos(2\Phi + \epsilon_1) \right]^{1/2} \tag{A.36}$$

$$r_{31} = \frac{d_2 \rho}{\sqrt{2}} \left[1 + \cos(2\Theta) \cos(2\Phi + \epsilon_2) \right]^{1/2}$$

where the indice 3 is surpressed.

Kuppermann pointed out that there are some disadvantages with this representation [41]. For the mapping of the triatomic potential energy surface to configuration space, we require that every internal configuration corresponds to one point only and that a transformation of Φ_k and Θ should rotate, but not distort, the equipotential surface about the z-axis. Because each particle arrangement corresponds to two points in the hyperspherical

coordinate space within the range of the hyperangles, we perform a second mapping

$$\theta = \pi/2 - 2\Theta,$$
$$\tilde{\phi}_k = \pi/2 - 2\Phi_k, \tag{A.37}$$

where the ranges of these new coordinates are

$$0 \le \theta \le \pi/2,$$
$$-7\pi/2 \le \tilde{\phi}_k < \pi/2, \tag{A.38}$$

and the distances are subsequently given by

$$r_{ij} = \frac{d_k \rho}{\sqrt{2}} \left[1 + \sin\theta \sin\tilde{\phi}_k \right]^{1/2}. \tag{A.39}$$

To get a more conveinient range we redefine $\phi_k = \tilde{\phi}_k + 7\pi/2$, so that the range is $0 \le \phi_k < 4\pi$. Then we finally get

$$r_{ij} = \frac{d_k \rho}{\sqrt{2}} \left[1 + \sin\theta \cos\phi_k \right]^{1/2}, \tag{A.40}$$

where the corresponding kinetic rotations are $\phi_j = \phi_i - 2\eta_{ij}$, in which the angle η_{ij} $(2\eta_{ij} = -2\beta_{ij})$ is in the range $0 \le \eta_{ij} \le \pi/2$ and have the properties

$$\eta_{ij} = -\eta_{ji}, \quad \eta_{ii} = 0, \tag{A.41a}$$

$$\tan\eta_{ij} = m_k/\mu, \tag{A.41b}$$

$$\eta_{12} + \eta_{23} + \eta_{31} = \pi. \tag{A.41c}$$

If the cartesian coordinates of this point in configuration space is defined to be the regular spherical polar coordinates, then all configurations will map to the upper half-space $z \ge 0$ (since $z_k = \rho\cos\theta$ and $0 \le \theta \le \pi/2$). Since ϕ_k and $\phi_k + 2\pi$ represent the same internal configuration and also points to the same point in configuration space, each point in the upper half-space represent a unique arrangement of the three-body system. Exchanging two of the particles will generate a new arrangement, which corrseponds to a new point in configuration space.

We can choose one of the branches of ϕ_k by restricting the range to $0 \le \phi_k < 2\pi$. Finally, we choose the Jacobi coordinates where $k = 3$ and

subsequently get the expression for our hyperspherical coordinates

$$
\begin{aligned}
r_{12} &= \frac{d_3 \rho}{\sqrt{2}} \left[1 + \sin\theta \cos\phi \right]^{1/2} \\
r_{23} &= \frac{d_1 \rho}{\sqrt{2}} \left[1 + \sin\theta \cos(\phi - \varphi_1) \right]^{1/2} \\
r_{31} &= \frac{d_2 \rho}{\sqrt{2}} \left[1 + \sin\theta \cos(\phi + \varphi_2) \right]^{1/2},
\end{aligned}
\tag{A.42}
$$

where

$$
\begin{aligned}
\varphi_1 &= 2\tan^{-1}(m_2/\mu), \\
\varphi_2 &= 2\tan^{-1}(m_1/\mu),
\end{aligned}
\tag{A.43}
$$

which for three identical particles is $\varphi_1 = \varphi_2 = 2\pi/3$.

In Fig. A.1 the triatomic potential energy surface for the model potential used in Section 4.4.2, see Eqs. (6.1) and (6.2), is shown for three identical particles. As seen in the figure, the translation and reflection symmetries reduce the range of ϕ once more to $0 \le \phi < \pi/3$ for identical particles.
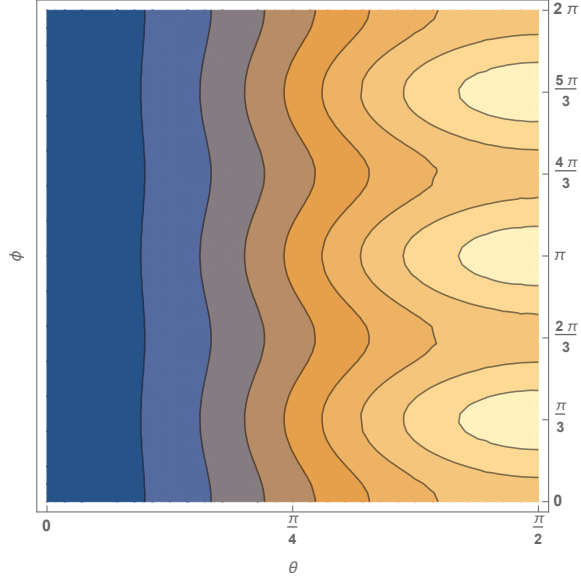

Figure A.1: Potential surface for three identical particles. Symmetries due to translations and reflections are seen at $\phi = n\pi/3$, $(n = 1 - 5)$.

A.2.2 Transformation of the Kinetic Energy Operator

The kinetic energy operator of a particle with mass μ in a curvilinear coordinate system of N dimensions is given by [42]

$$T = -\frac{1}{2\mu} \sum_{i=1}^{N} \sum_{j=1}^{N} \frac{1}{\sqrt{g}} \frac{\partial}{\partial q_i} \left(\sqrt{g} g^{ij} \frac{\partial}{\partial q_j} \right), \tag{A.44}$$

where g^{ij} is the inverse, or contravariant, metric tensor and g is the determinant of the covariant metric tensor $g = \det(g_{ij}) \neq 0$. The metric tensor g_{ij} describes the relationship between the set of curvilinear coordinates $\mathbf{q}$ and the set of regular Cartesian coordinates $\mathbf{x}$ through

$$g_{ij} = \sum_{\lambda=1}^{N} \frac{\partial x_\lambda}{\partial q_i} \frac{\partial x_\lambda}{\partial q_j}, \tag{A.45}$$

where $x_\lambda = x_\lambda(q_1, \ldots, q_N)$. The metric is usefull for generalizing the concept of distance to general curvilinear coordinate frames and hence maintain the invariance of distance in different coordinate systems. Invariance of the square of the line element ds^2 under coordinate transformations can also be considered to define the metric itself since

$$ds^2 = d\mathbf{x} \cdot d\mathbf{x} = \sum_{i,j}^{N} g_{ij} dq_i dq_j = g. \tag{A.46}$$

Here the displacement differential vector is given by

$$d\mathbf{x} = \frac{\partial \mathbf{x}}{\partial q_i} dq_i, \tag{A.47}$$

where $\mathbf{x}$ is the position vector.

The tranformation of interest for us is that from the mass weighted Jacobi coordinates $\mathbf{r}_k$ and $\mathbf{R}_k$ to a set of symmetric coordinates. Here we choose to work with one of the pair of the Jacobi coordinate sets $(i, j, k) = (1, 2, 3)$ and surpress the subscript 3. Since the three-body system has $N = 6$ dimensions after separating out the center-of-mass we collect the Cartesian components of the mass-weighted Jacobian vectors into the 6-position

$$\mathbf{x} = \begin{pmatrix} \mathbf{r} \\ \mathbf{R} \end{pmatrix} = \begin{pmatrix} r_x \\ r_y \\ r_z \\ R_x \\ R_y \\ R_z \end{pmatrix}. \tag{A.48}$$

At any instant, three particles form a plane in $\mathbb{R}^3$. If we consider this plane to be the xy-plane – and define the internal motion of the particles within this plane in terms of hyperspherical coordinates (ρ, Θ, Φ) – our coordinate system must rotate in this plane. That is, we use a body-fixed axis system xyz, which rotates with respect to the space-fixed axis system $x'y'z'$. The orientation of the body-fixed frame is related to the space-fixed frame by the Euler angles. With the z-axis perpendicular to the plane and with the positive axis in the direction of the vector $\mathbf{r} \times \mathbf{R}$, Smith and Whitten [35] defined these as

$$\begin{aligned} r_x &= \rho \cos \Theta \cos \Phi, \\ r_y &= -\rho \sin \Theta \sin \Phi, \\ r_z &= 0 \\ R_x &= \rho \cos \Theta \sin \Phi, \\ R_y &= \rho \sin \Theta \cos \Phi, \\ R_z &= 0. \end{aligned} \tag{A.49}$$

To describe how rotations of the body-fixed frame affects the derivatives in the space-fixed frame it is enough to consider infinitesimal rotations. Let $d\mathbf{\Omega}$ be the angular displacement differential vector of the rotating axes xyz with respect to the fixed axes $x'y'z'$

$$d\mathbf{\Omega} = \begin{pmatrix} d\Omega_x \\ d\Omega_y \\ d\Omega_z \end{pmatrix}. \tag{A.50}$$

Then the displacement differential vectors in the space-fixed frame transform

like

$$d\mathbf{r}' = d\mathbf{r} + d\mathbf{\Omega} \times \mathbf{r}, \tag{A.51a}$$

$$d\mathbf{R}' = d\mathbf{R} + d\mathbf{\Omega} \times \mathbf{R}, \tag{A.51b}$$

which is given explicitly by

$$
\begin{pmatrix} dr'_x \\ dr'_y \\ dr'_z \\ dR'_x \\ dR'_y \\ dR'_z \end{pmatrix} =
\begin{pmatrix}
\partial_\rho r_x & \partial_\Theta r_x & \partial_\Theta r_x & 0 & r_z & -r_y \\
\partial_\rho r_y & \partial_\Theta r_y & \partial_\Theta r_y & -r_z & 0 & r_x \\
\partial_\rho r_z & \partial_\Theta r_z & \partial_\Theta r_z & r_y & -r_x & 0 \\
\partial_\rho R_x & \partial_\Theta R_x & \partial_\Theta R_x & 0 & R_z & -R_y \\
\partial_\rho R_y & \partial_\Theta R_y & \partial_\Theta R_y & -R_z & 0 & R_x \\
\partial_\rho R_z & \partial_\Theta R_z & \partial_\Theta R_z & R_y & -R_x & 0
\end{pmatrix}
\begin{pmatrix} d\rho \\ d\Theta \\ d\Phi \\ d\Omega_x \\ d\Omega_y \\ d\Omega_z \end{pmatrix}
$$

$$
=
\begin{pmatrix}
\text{cc} & -\text{sc} & -\text{cs} & 0 & 0 & \text{ss} \\
-\text{ss} & -\text{cs} & -\text{sc} & 0 & 0 & \text{cc} \\
0 & 0 & 0 & -\text{ss} & -\text{cc} & 0 \\
\text{cs} & -\text{ss} & \text{cc} & 0 & 0 & -\text{sc} \\
\text{sc} & \text{cc} & -\text{ss} & 0 & 0 & \text{cs} \\
0 & 0 & 0 & \text{sc} & -\text{cs} & 0
\end{pmatrix}
\begin{pmatrix} d\rho \\ \rho d\Theta \\ \rho d\Phi \\ \rho d\Omega_x \\ \rho d\Omega_y \\ \rho d\Omega_z \end{pmatrix}, \tag{A.52}
$$

where the abbreviations are cc $= \cos\Theta\cos\Phi$, ss $= \sin\Theta\sin\Phi$, cs $= \cos\Theta\sin\Phi$ and sc $= \sin\Theta\cos\Phi$. In matrix notation (A.52) may be expressed as

$$d\mathbf{x}' = \mathbf{A}d\mathbf{q}, \tag{A.53}$$

in which

$$
d\mathbf{q} =
\begin{pmatrix} d\rho \\ d\Theta \\ d\Phi \\ d\Omega_x \\ d\Omega_y \\ d\Omega_z \end{pmatrix}. \tag{A.54}
$$

The squared line element ds^2 is then given by

$$ds^2 = d\mathbf{x}' \cdot d\mathbf{x}' = d\mathbf{q}^\mathrm{T} \mathbf{A}^\mathrm{T} \mathbf{A} d\mathbf{q} = d\mathbf{q}^\mathrm{T} \mathbf{g} d\mathbf{q}. \tag{A.55}$$

Here the metric tensor

$$\mathbf{g} = \mathbf{A}^\mathrm{T}\mathbf{A} = \begin{pmatrix} \mathbf{G} & \mathbf{C} \\ \mathbf{C}^\mathrm{T} & \mathbf{K} \end{pmatrix} \tag{A.56}$$

is partitioned into the submatrices $\mathbf{G}$, $\mathbf{K}$ and $\mathbf{C}$, which are given by

$$\mathbf{G} = \begin{pmatrix} 1 & 0 & 0 \\ 0 & \rho^2 & 0 \\ 0 & 0 & \rho^2 \end{pmatrix}, \tag{A.57}$$

$$\mathbf{K} = \rho^2 \begin{pmatrix} \sin^2\Theta & 0 & 0 \\ 0 & \cos^2\Theta & 0 \\ 0 & 0 & 1 \end{pmatrix}, \tag{A.58}$$

and

$$\mathbf{C} = -\rho^2 \sin^2(2\Theta) \begin{pmatrix} 0 & 0 & 0 \\ 0 & 0 & 0 \\ 0 & 0 & 1 \end{pmatrix}, \tag{A.59}$$

respectively. The determinant of the metric tensor is then

$$g = \mid \mathbf{g} \mid = \begin{vmatrix} \mathbf{G} & \mathbf{C} \\ \mathbf{C}^T & \mathbf{K} \end{vmatrix} = \frac{\rho^{10}}{16} \sin^2(4\Theta) \tag{A.60}$$

and subsequently the square root of the metric reads

$$\sqrt{g} = \frac{\rho^5}{4} \sin(4\Theta). \tag{A.61}$$

The inverse of the metric tensor $\mathbf{g}^{-1}$ is then given by

$$\mathbf{g}^{-1} = \begin{pmatrix} \mathbf{V} & \mathbf{W} \\ \mathbf{W}^\mathrm{T} & \mathbf{U} \end{pmatrix}, \tag{A.62}$$

where the submatrices $\mathbf{V}$, $\mathbf{W}$ and $\mathbf{U}$ are given by

$$\mathbf{V} = \begin{pmatrix} 1 & 0 & 0 \\ 0 & 1/\rho^2 & 0 \\ 0 & 0 & 1/\rho^2\cos^2(2\Theta) \end{pmatrix}, \tag{A.63}$$

$$\mathbf{U} = \frac{1}{\rho^2} \begin{pmatrix} 1/\sin^2\Theta & 0 & 0 \\ 0 & 1/\cos^2\Theta & 0 \\ 0 & 0 & 1/\cos^2(2\Theta) \end{pmatrix}, \tag{A.64}$$

and

$$\mathbf{W} = \frac{\sin(2\Theta)}{\rho^2\cos^2(2\Theta)} \begin{pmatrix} 0 & 0 & 0 \\ 0 & 0 & 0 \\ 0 & 0 & 1 \end{pmatrix}, \tag{A.65}$$

respectively. Now, if the momentum vector is given by

$$\mathbf{p} = i \begin{pmatrix} \partial/\partial q_1 \\ \vdots \\ \partial/\partial q_N \end{pmatrix} \tag{A.66}$$

we can express the kinetic energy operator given in (A.44) in terms of this vector and the metric

$$-T = -\frac{1}{2\mu\sqrt{g}}\mathbf{p}^{\mathrm{T}}\sqrt{g}\mathbf{g}^{-1}\mathbf{p}$$

$$= \frac{1}{2\mu\rho^5\sin(4\Theta)}\left[\frac{\partial}{\partial\rho}\left(\rho^5\sin(4\Theta)\frac{\partial}{\partial\rho}\right) + \frac{\partial}{\partial\Theta}\left(\rho^3\sin(4\Theta)\frac{\partial}{\partial\Theta}\right)\right.$$

$$+ \frac{\partial}{\partial\Phi}\left(2\rho^3\tan(2\Theta)\frac{\partial}{\partial\Phi} + 2\tan^2(2\Theta)\cos(2\Theta)\frac{\partial}{\partial\Omega_z}\right)$$

$$+ \frac{\partial}{\partial\Omega_x}\left(4\rho^3\cot(\Theta)\cos(2\Theta)\frac{\partial}{\partial\Omega_x}\right)$$

$$+ \frac{\partial}{\partial\Omega_y}\left(4\rho^3\tan(2\Theta)\cos(2\Theta)\frac{\partial}{\partial\Omega_y}\right)$$

$$\left.+ \frac{\partial}{\partial\Omega_z}\left(2\rho^3\tan^2(2\Theta)\frac{\partial}{\partial\Phi} + 2\rho^3\tan(2\Theta)\frac{\partial}{\partial\Omega_z}\right)\right]$$

$$= \frac{1}{2\mu\rho^5}\frac{\partial}{\partial\rho}\left(\rho^5\frac{\partial}{\partial\rho}\right) + \frac{1}{2\mu\rho^2}\left[\frac{1}{\sin(4\Theta)}\frac{\partial}{\partial\Theta}\left(\sin(4\Theta)\frac{\partial}{\partial\Theta}\right)\right.$$

$$\left.+ \frac{1}{\cos^2(2\Theta)}\frac{\partial^2}{\partial\Phi^2}\right] + \frac{1}{2\mu\rho^2}\left[\frac{1}{\sin^2(\Theta)}\frac{\partial^2}{\partial\Omega_x^2} + \frac{1}{\cos^2(\Theta)}\frac{\partial^2}{\partial\Omega_y^2} + \frac{1}{\cos^2(2\Theta)}\frac{\partial^2}{\partial\Omega_z^2}\right.$$

$$\left.+ \frac{2\sin(2\Theta)}{\cos^2(2\Theta)}\frac{\partial}{\partial\Phi}\frac{\partial}{\partial\Omega_z}\right].$$

$$(A.67)$$

Now, as have been mentioned previously, we use the Euler angles α, β, γ to relate the body-fixed axes xyz with the space-fixed axes $x'y'z'$. Any coordinate frame that coincide with the space-fixed frame can be made to coincide with the body-fixed frame by performing a series of three basic rotations (right-handed). There are several ways for defining the Euler angles, the convention used by Johnson [43] is adopted here and the method is decribed in detail in [44]. If the line of nodes ξ are the intersection of the planes $x'y'$ and xy, then α is the angle between the y'-axis and the line of nodes. The operational sequence are the following:

(i) First rotate the coordinates $x'y'z'$ counterclockwise through an angle α in the range $0 \le \alpha < 2\pi$ about the z'-axis, using $\mathbf{S}_\alpha$, into the new coordinates $\bar{x}'\xi z'$.

(ii) Then rotate the coordinates $\bar{x}'\xi z'$ counterclockwise through an angle β

$(0 \leq \beta \leq \pi)$ about the line of nodes, using $\mathbf{S}_\beta$, into the new coordinates $\bar{x}\xi z$.

(iii) Finally rotate the coordinates $\bar{x}\xi z$ counterclockwise by an angle γ ($0 \leq \gamma < 2\pi$) about the z-axis (the former z'-axis) using $\mathbf{S}_\gamma$, into the body-fixed coordinates xyz.

The total rotation matrix is then the triple matrix product of the basic rotation matrices $\mathbf{S} = \mathbf{S}_\alpha \mathbf{S}_\beta \mathbf{S}_\gamma$, in which

$$\mathbf{S}_\alpha = \begin{pmatrix} \cos\alpha & \sin\alpha & 0 \\ -\sin\alpha & \cos\alpha & 0 \\ 0 & 0 & 1 \end{pmatrix}, \tag{A.68}$$

$$\mathbf{S}_\beta = \begin{pmatrix} \cos\beta & 0 & -\sin\beta \\ 0 & 1 & 0 \\ \sin\beta & 0 & \cos\beta \end{pmatrix}, \tag{A.69}$$

$$\mathbf{S}_\gamma = \begin{pmatrix} \cos\gamma & \sin\gamma & 0 \\ -\sin\gamma & \cos\gamma & 0 \\ 0 & 0 & 1 \end{pmatrix}, \tag{A.70}$$

and

$$\mathbf{S} = \begin{pmatrix} \cos\gamma\cos\beta\cos\alpha - \sin\gamma\sin\alpha & \cos\gamma\cos\beta\sin\alpha\sin\gamma\cos\alpha & -\cos\gamma\sin\beta \\ -\sin\gamma\cos\beta\cos\alpha - \cos\gamma\sin\alpha & \sin\gamma\cos\beta\sin\alpha + \cos\gamma\cos\alpha & \sin\gamma\sin\beta \\ \sin\beta\cos\alpha & \sin\beta\sin\alpha & \cos\beta \end{pmatrix}. \tag{A.71}$$

The cartesian coordinates $\mathbf{x}$ and $\mathbf{x}'$ of a point P in the two frames are thus related through

$$\mathbf{x} = \mathbf{S}\mathbf{x}'. \tag{A.72}$$

Now, the general angular displacement differential $d\mathbf{\Omega}$ can be considered as consisting of three consecutive infinitesimal rotations where $d\Omega_\alpha = d\alpha$, $d\Omega_\beta = d\beta$ and $d\Omega_\gamma = d\gamma$. The vector $d\mathbf{\Omega}$ can be obtained as the sum of three different angular displacement differential vectors; $d\mathbf{\Omega}_\alpha$ is along the space-fixed z'-axis, $d\mathbf{\Omega}_\beta$ is along the line of nodes and $d\mathbf{\Omega}_\gamma$ is along the body-fixed z-axis [45]. Since $d\mathbf{\Omega}_\alpha$ is along the z'-axis, its components are obtained by

the applying the total rotation matrix. Thus, if the total rotation matrix is written

$$\mathbf{S} = [\mathbf{S}_1 \quad \mathbf{S}_2 \quad \mathbf{S}_3], \tag{A.73}$$

then the body-fixed displacement differential angles $d\mathbf{\Omega}_\alpha$ are related to the Euler angles through

$$(\mathbf{\Omega}_\alpha)_\mathbf{x} = \mathbf{S}_3 d\alpha = \begin{pmatrix} -\sin\beta\cos\gamma \\ \sin\beta\sin\gamma \\ \cos\beta \end{pmatrix} d\alpha. \tag{A.74}$$

Next, because $d\mathbf{\Omega}_\beta$ is along the line of nodes, we only need to apply the last transformation $\mathbf{S}_\gamma$ to retreive

$$(\mathbf{\Omega}_\beta)_\mathbf{x} = \mathbf{S}_{\gamma_2} d\beta = \begin{pmatrix} \sin\gamma \\ \cos\gamma \\ 0 \end{pmatrix} d\beta. \tag{A.75}$$

No transformation is needed for $d\mathbf{\Omega}_\gamma$ since it is already directed along the body-fixed z-axis. The transformations are finally summarized into the total transformation matrix, which relates the body-fixed infinitesimal rotations to the Euler angles through

$$\begin{pmatrix} d\Omega_x \\ d\Omega_y \\ d\Omega_z \end{pmatrix} = \tilde{\mathbf{S}} \begin{pmatrix} d\alpha \\ d\beta \\ d\gamma \end{pmatrix}, \tag{A.76}$$

where

$$\tilde{\mathbf{S}} = \begin{pmatrix} -\sin\beta\cos\gamma & \sin\gamma & 0 \\ \sin\beta\sin\gamma & \cos\gamma & 0 \\ \cos\beta & 0 & 1 \end{pmatrix}. \tag{A.77}$$

Thus, a transformation of coordinates

$$d\mathbf{q} = \begin{pmatrix} d\rho \\ d\Theta \\ d\Phi \\ d\Omega_x \\ d\Omega_y \\ d\Omega_z \end{pmatrix} \longrightarrow d\mathbf{q}' = \begin{pmatrix} d\rho \\ d\Theta \\ d\Phi \\ d\alpha \\ d\beta \\ d\gamma \end{pmatrix} \tag{A.78}$$

correspond to a transformation of the metric, which is easily derived from the squared line element, where

$$ds^2 = d\mathbf{q}^{\mathrm{T}} \mathbf{g} d\mathbf{q} = (d\mathbf{q}')^{\mathrm{T}} \mathbf{g}' d\mathbf{q}'. \tag{A.79}$$

The metric thus transform as

$$\mathbf{g}' = \mathbf{B}^{\mathrm{T}} \mathbf{g} \mathbf{B}, \tag{A.80}$$

in which

$$\mathbf{B} = \begin{pmatrix} \mathbf{I} & 0 \\ 0 & \tilde{\mathbf{S}} \end{pmatrix}. \tag{A.81}$$

Subsequently, the square root of the determinant transform into

$$g'^{1/2} = (|\mathbf{B}|^2 |\mathbf{g}|)^{1/2} = (|\tilde{\mathbf{S}}|^2 |\mathbf{g}|)^{1/2} = \frac{\rho^5}{4} \sin(4\Theta) \sin\beta. \tag{A.82}$$

Since a general curvilinear coordinate system of N dimensions have a volume element

$$d^N v = g^{1/2} \prod_{i=1}^{N} dq_i, \tag{A.83}$$

the sought volume element is

$$d^6 v = g^{1/2} \prod_{i=1}^{6} dq_i = \frac{\rho^5}{4} \sin(4\Theta) \sin\beta \, d\rho \, d\Theta \, d\Phi \, d\alpha \, d\beta \, d\gamma. \tag{A.84}$$

Lastly, to produce a representation of the entire internal configuration space that is unbiased by the particular choice of the three Jacobi coordinate sets,

we follow Kuppermann's mapping procedure [41] and make the following modification of the internal angles

$$\begin{aligned}
\Theta &= \frac{\pi}{4} - \frac{\theta}{2} \implies \frac{\partial}{\partial \Theta} = -2\frac{\partial}{\partial \theta}, \\
\Phi &= \frac{\pi}{4} - \frac{\phi}{2} \implies \frac{\partial}{\partial \Phi} = -2\frac{\partial}{\partial \phi}.
\end{aligned} \tag{A.85}$$

Now, define

$$\mathbf{P} = -i \begin{pmatrix} \partial/\partial \rho \\ \partial/\partial \theta \\ \partial/\partial \phi \end{pmatrix} = \begin{pmatrix} P_\rho \\ P_\theta \\ P_\phi \end{pmatrix} \tag{A.86}$$

and

$$\mathbf{J} = -i \begin{pmatrix} \partial/\partial \Omega_x \\ \partial/\partial \Omega_y \\ \partial/\partial \Omega_z \end{pmatrix} = \begin{pmatrix} J_x \\ J_y \\ J_z \end{pmatrix}, \tag{A.87}$$

where the operators J_x, J_y, and J_z are the total angular momentum operators in the body-fixed frame, which can be expressed in terms of the Euler angle coordinates by the relation

$$\begin{pmatrix} J_x \\ J_y \\ J_z \end{pmatrix} = \begin{pmatrix} -\cos\gamma/\sin\beta & \sin\gamma & \cot\beta\cos\gamma \\ \sin\gamma/\sin\beta & \cos\gamma & -\cot\beta\sin\gamma \\ 0 & 0 & 1 \end{pmatrix} \begin{pmatrix} P_\alpha \\ P_\beta \\ P_\gamma \end{pmatrix}. \tag{A.88}$$

This can be shown using the chain rule for partial differentiation

$$P_\sigma = \sum_\lambda \frac{\partial \Omega_\lambda}{\partial \sigma} J_\lambda, \tag{A.89}$$

where $\sigma = (\alpha, \beta, \gamma)$ and $\lambda = (x, y, z)$. The partial derivatives are calculated using the inverse of (A.77), which is given by

$$\tilde{\mathbf{S}}^{-1} = \begin{pmatrix} -\cos\gamma/\sin\beta & \sin\gamma/\sin\beta & 0 \\ \sin\gamma & \cos\gamma & 0 \\ \cot\beta\cos\gamma & -\cot\beta\sin\gamma & 1 \end{pmatrix}. \tag{A.90}$$

Now, using the relations

$$\sin 4\Theta = \sin 2\theta$$
$$\cos^2 2\Theta = \sin^2 \theta$$
$$\sin^2 2\Theta = \cos^2 \theta \qquad (A.91)$$
$$\cos^2 \Theta = \frac{1}{2}(1 + \sin \theta)$$
$$\sin^2 \Theta = \frac{1}{2}(1 - \sin \theta)$$

in conjunction with (A.87) the kinetic energy operator (A.67) becomes

$$T = -\frac{\hbar^2}{2\mu}\left[\frac{1}{\rho^5}\frac{\partial}{\partial\rho}\rho^5\frac{\partial}{\partial\rho} + \frac{4}{\rho^2}\left(\frac{1}{\sin(2\theta)}\frac{\partial}{\partial\theta}\sin(2\theta)\frac{\partial}{\partial\theta} \right.\right.$$
$$\left.\left. + \frac{1}{\sin^2(\theta)}\frac{\partial^2}{\partial\phi^2} \right) \right] - \frac{1}{\mu\rho^2}\left[\frac{J_x^2}{(1 - \sin\theta)} + \frac{J_y^2}{(1 + \sin\theta)} + \frac{J_z^2}{2\sin^2\theta} \right] \qquad (A.92)$$
$$+ \frac{4i\hbar\cos\theta\, J_z}{2\mu\rho^2\sin^2\theta}\frac{\partial}{\partial\phi},$$

with the corresponding volume element

$$d^6 v = \frac{1}{8}\rho^5 \sin\theta\cos\theta\sin\beta\, d\rho\, d\theta\, d\phi\, d\alpha\, d\beta\, d\gamma. \qquad (A.93)$$

If we only consider $J = 0$ states, the Hamiltonian reduces to

$$H_0 = -\frac{1}{2\mu}\left[\frac{1}{\rho^5}\frac{\partial}{\partial\rho}\rho^5\frac{\partial}{\partial\rho} + \frac{4}{\rho^2}\left(\frac{1}{\sin(2\theta)}\frac{\partial}{\partial\theta}\sin(2\theta)\frac{\partial}{\partial\theta} + \frac{1}{\sin^2(\theta)}\frac{\partial^2}{\partial\phi^2} \right) \right] + V(\rho, \theta, \phi). \qquad (A.94)$$

By rescaling the wave function $\psi = \rho^{5/2}\Psi$ the Schrödinger equation becomes

$$H\psi = E\psi, \qquad (A.95)$$

where the transformed Hamiltonian operator is given by

$$H = \rho^{5/2} H_0 \rho^{-5/2}. \qquad (A.96)$$

This transformation removes the first derivative in the hyper radial kinetic-energy operator and we get the final expression for the Hamiltonian

$$H = -\frac{\hbar^2}{2\mu}\left[-\frac{15}{4}\frac{1}{\rho^2} + \frac{\partial^2}{\partial\rho^2} + \frac{4}{\rho^2}\left(\frac{1}{\sin(2\theta)}\frac{\partial}{\partial\theta}\sin(2\theta)\frac{\partial}{\partial\theta} + \frac{1}{\sin^2(\theta)}\frac{\partial^2}{\partial\phi^2} \right) \right] + V(\rho,\theta,\phi)$$

$$\text{(A.97)}$$

$$= -\frac{\hbar^2}{2\mu}\frac{\partial^2}{\partial\rho^2} + \frac{\hbar^2}{2\mu\rho^2}\left(\Lambda^2 + \frac{15}{4} \right) + V(\rho,\theta,\phi), \qquad\qquad \text{(A.98)}$$

where Λ^2 is the grand angular momentum operator.

Appendix B

Basis Splines

A basis spline, or B-spline, of order k is a piecewise polynomial function of degree $(k-1)$ defined on a collection of points, t_i, called *knot points*. The array formed by these knot points are refered to as *knot sequence*, or knot vector, where $t_i \leq t_{i+1}$. B-splines of order k can be defined recursively by the Cox-de Boor formula. With a given knot sequence, the B-splines of order $k = 1$ is defined as

$$B_{i,k=1}(x) \doteq \begin{cases} 1, & \text{if} \quad t_i \leq x < t_{i+1} \\ 0, & \text{otherwise} \end{cases} \tag{B.1}$$

and if $k > 1$

$$B_{i,k}(x) \doteq \frac{x - t_i}{t_{i+k-1} - t_i} B_{i,k-1}(x) + \frac{t_{i+k} - x}{t_{i+k} - t_{i+1}} B_{i+1,k-1}(x). \tag{B.2}$$

The B-splines are local in the sense that they will be non-zero only in a limited region of space. If the numbering is such that the first knot point is t_1 and the first B-spline is $B_{1,k}$, then the B-spline $B_{i,k}$ is non-zero within the region $t_i \leq x \leq t_{i+k}$. On a given knot sequence $(t_1, \ldots, t_P)$ the B-splines form a complete set

$$\sum_{i=1}^{P} B_{i,k}(x) = 1. \tag{B.3}$$

By placing $(k-1)$ additional points, called ghost points, at the end-points, the B-splines will be confined within the region $t_1 \leq x \leq t_P$. This means

that P knot points correspond to $N = P - 2(k-1)$ physical points. B-splines of orders $k = 1 - 4$ are shown in Fig. B.1. The first derivative of a B-spline of order k is given by

$$\frac{\partial}{\partial x} B_{i,k}(x) = (k-1)\left(\frac{B_{i,k-1}(x)}{t_{i+k-1} - t_i} + \frac{B_{i+1,k-1}(x)}{t_{i+k} - t_{i+1}} \right), \qquad \text{(B.4)}$$

and the second derivative

$$\frac{\partial^2}{\partial x^2} B_{i,k}(x) = \frac{(k-1)(k-2)B_{i,k-2}(x)}{(t_{i+k-1} - t_i)(t_{i+k-2} - t_i)} - \frac{(k-1)(k-2)B_{i+1,k-2}(x)}{(t_{i+k-1} - t_i)(t_{i+k-1} - t_{i+1})}$$
$$- \frac{(k-1)(k-2)B_{i+1,k-2}(x)}{(t_{i+k} - t_{i+1})(t_{i+k-1} - t_{i+1})} + \frac{(k-1)(k-2)B_{i+2,k-2}(x)}{(t_{i+k} - t_{i+1})(t_{i+k} - t_{i+2})}.$$
$$\text{(B.5)}$$

The approach of placing the ghost points in the end-points is common because at the first physical point only the first B-spline non-zero and only the first two B-splines will have non-zero derivatives. Likewise, at the last physical point only the last B-spline will be non-zero and only the two last B-splines will have non-zero derivatives. Consequently, this choice favors implementation of boundary conditions which require the function or it's derivative to be zero at the boundary.
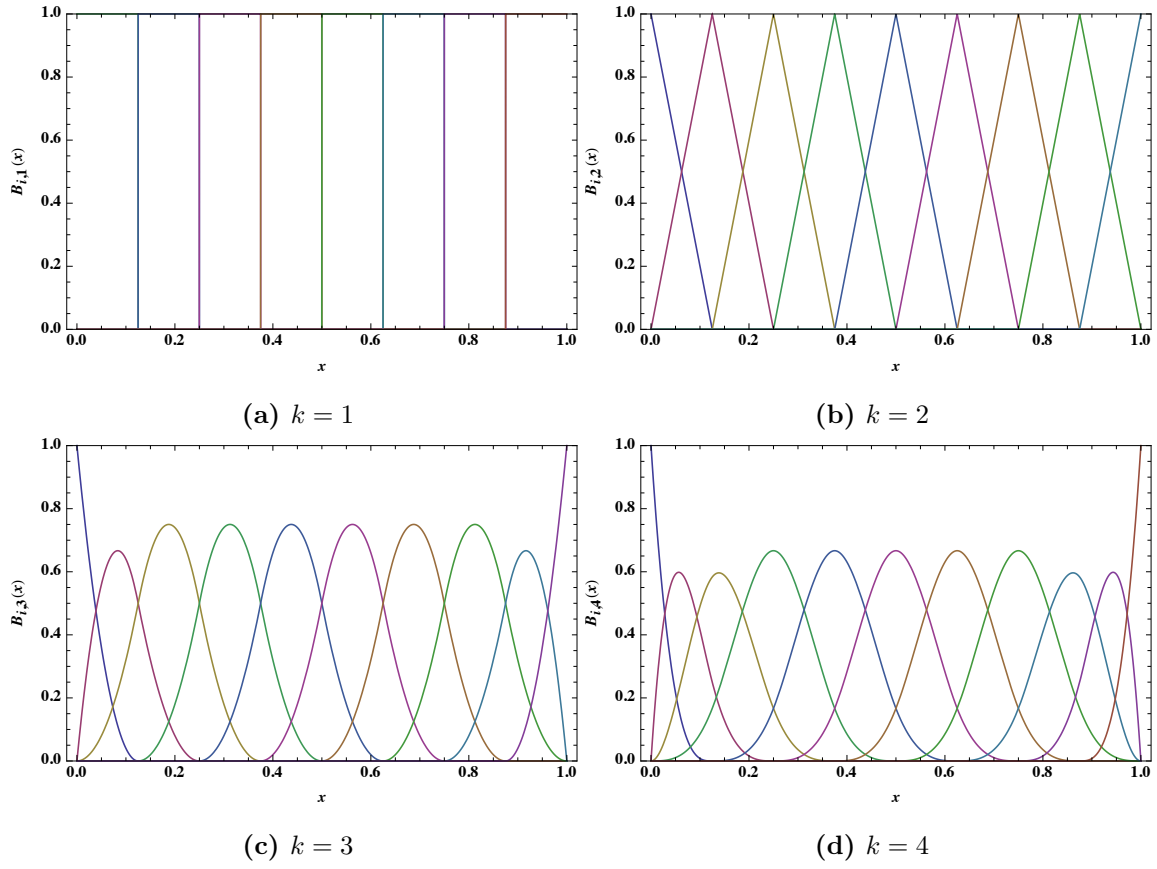
Figure B.1: The subfigures above show the B-splines $B_{i,k}(x)$ of different orders k on a one dimensional mesh.

Bibliography

[1] Alain Chenciner. 'Poincaré and the Three-Body Problem'. In: *Henri Poincaré, 1912–2012: Poincaré Seminar 2012*. Ed. by Bertrand Duplantier and Vincent Rivasseau. Basel: Springer Basel, 2015, pp. 51–149. ISBN: 978-3-0348-0834-7. DOI: `10.1007/978-3-0348-0834-7_2`. URL: `https://doi.org/10.1007/978-3-0348-0834-7_2`.

[2] Vitaly Efimov. 'Is a qualitative approach to the three-body problem useful?' In: *Comments Nucl. Part. Phys.* 19 (1990), pp. 271–293.

[3] L. D. Faddeev. 'Scattering theory for a three particle system'. In: *Sov. Phys. JETP* 12 (1961). [Zh. Eksp. Teor. Fiz.39,1459(1960)], pp. 1014–1019.

[4] Alexander L. Zubarev and Victor B. Mandelzweig. 'Exact solution of the four-body Faddeev-Yakubovsky equations for the harmonic oscillator'. In: *Phys. Rev. C* 50 (1 July 1994), pp. 38–47. DOI: `10.1103/PhysRevC.50.38`. URL: `https://link.aps.org/doi/10.1103/PhysRevC.50.38`.

[5] V. Efimov. 'Energy levels arising form the resonant two-body forces in a three-body system'. In: *Phys. Lett.* 33B (1970), pp. 563–564. DOI: `10.1016/0370-2693(70)90349-7`.

[6] V. N. Efimov. 'WEAKLY-BOUND STATES OF 3 RESONANTLY-INTERACTING PARTICLES'. In: *Sov. J. Nucl. Phys.* 12 (1971), p. 589.

[7] Cheng Chin et al. 'Feshbach resonances in ultracold gases'. In: *Rev. Mod. Phys.* 82 (2 Apr. 2010), pp. 1225–1286. DOI: `10.1103/RevModPhys.82.1225`. URL: `https://link.aps.org/doi/10.1103/RevModPhys.82.1225`.

[8]   Kajsa-My Blomdahl. 'Numerical Calculations of Efimov States in Ultracold Atomic Systems'. MA thesis. http://www.diva-portal.org: KTH, 2016.

[9]   Cheng Chin et al. 'Feshbach resonances in ultracold gases'. In: *Rev. Mod. Phys.* 82 (2 Apr. 2010), pp. 1225–1286. DOI: 10.1103/RevModPhys.82.1225. URL: https://link.aps.org/doi/10.1103/RevModPhys.82.1225.

[10]   S. Virulh. *Condensed Matter Theories, Volume 23 - Proceedings Of The 31st International Workshop.* World Scientific Publishing Company, 2008, pp. 86–87. ISBN: 9789814469371. URL: https://books.google.se/books?id=cPLFCgAAQBAJ.

[11]   T. Kraemer et al. 'Evidence for Efimov quantum states in an ultracold gas of caesium atoms'. In: *Nature* 440 (Mar. 2006), URL: http://dx.doi.org/10.1038/nature04626.

[12]   Bo Huang et al. 'Observation of the Second Triatomic Resonance in Efimov's Scenario'. In: *Phys. Rev. Lett.* 112 (19 May 2014), p. 190401. DOI: 10.1103/PhysRevLett.112.190401. URL: https://link.aps.org/doi/10.1103/PhysRevLett.112.190401.

[13]   Catherine E. Klauss et al. 'Observation of Efimov Molecules Created from a Resonantly Interacting Bose Gas'. In: *Phys. Rev. Lett.* 119 (14 Oct. 2017), p. 143401. DOI: 10.1103/PhysRevLett.119.143401. URL: https://link.aps.org/doi/10.1103/PhysRevLett.119.143401.

[14]   M. Zaccanti et al. 'Observation of an Efimov spectrum in an atomic system.' In: *NATURE PHYSICS* 8 (2009), p. 586. ISSN: 1745-2473. URL: https://ezp.sub.su.se/login?url=http://search.ebscohost.com/login.aspx?direct=true&db=edsbl&AN=RN255515896&site=eds-live&scope=site.

[15]   Noam Gross et al. 'Observation of Universality in Ultracold Li-7 Three-Body Recombination'. In: *Physical review letters* 103 (Oct. 2009), p. 163202. DOI: 10.1103/PHYSREVLETT.103.163202.

[16]   J. R. Williams et al. 'Evidence for an Excited-State Efimov Trimer in a Three-Component Fermi Gas'. In: *Phys. Rev. Lett.* 103 (13 Sept. 2009), p. 130404. DOI: 10.1103/PhysRevLett.103.130404. URL: https://link.aps.org/doi/10.1103/PhysRevLett.103.130404.

[17] R. A. W. Maier et al. 'Efimov Resonance and Three-Body Parameter in a Lithium-Rubidium Mixture'. In: *Phys. Rev. Lett.* 115 (4 July 2015), p. 043201. DOI: 10.1103/PhysRevLett.115.043201. URL: https://link.aps.org/doi/10.1103/PhysRevLett.115.043201.

[18] J. Ulmanis et al. 'Universality of weakly bound dimers and Efimov trimers close to Li-Cs Feshbach resonances'. In: *New Journal of Physics* 17.5, 055009 (May 2015), p. 055009. DOI: 10.1088/1367-2630/17/5/055009. arXiv: 1501.04799 [cond-mat.quant-gas].

[19] T. K. Lim, Sister Kathleen Duffy and William C. Damer. 'Efimov State in the ^{4}He Trimer'. In: *Phys. Rev. Lett.* 38 (7 Feb. 1977), pp. 341–343. DOI: 10.1103/PhysRevLett.38.341. URL: https://link.aps.org/doi/10.1103/PhysRevLett.38.341.

[20] Q. Guan and D. Blume. 'Electric-field-induced helium-helium resonances'. In: *Phys. Rev. A* 99 (3 Mar. 2019), p. 033416. DOI: 10.1103/PhysRevA.99.033416. URL: https://link.aps.org/doi/10.1103/PhysRevA.99.033416.

[21] E. Hiyama and M. Kamimura. 'Linear correlations between ^{4}He trimer and tetramer energies calculated with various realistic ^{4}He potentials'. In: *Phys. Rev. A* 85 (6 June 2012), p. 062505. DOI: 10.1103/PhysRevA.85.062505. URL: https://link.aps.org/doi/10.1103/PhysRevA.85.062505.

[22] Maksim Kunitski et al. 'Three-body physics. Observation of the Efimov state of the helium trimer'. In: *Science* 348 (May 2015), pp. 551–555. DOI: 10.1126/science.aaa5601.

[23] Francesca Ferlaino et al. 'Evidence for Universal Four-Body States Tied to an Efimov Trimer'. In: *Physical review letters* 102 (May 2009), p. 140401. DOI: 10.1103/PHYSREVLETT.102.140401.

[24] L. D. Landau and L. M. Lifshitz. *Quantum Mechanics Non-Relativistic Theory, Second Edition: Volume 3*. 2nd ed. Pergamon Press, 1965, pp. 72–74. ISBN: 0750635398.

[25] H R Sadeghpour et al. 'Collisions near threshold in atomic and molecular physics'. In: *Journal of Physics B: Atomic, Molecular and Optical Physics* 33.5 (Feb. 2000), R93–R140. DOI: 10.1088/0953-4075/33/5/201. URL: https://www.cfa.harvard.edu/~hrs/PubList/

JPBThresholdReviw2000.pdhttps://doi.org/10.1088%2F0953-
4075%2F33%2F5%2F201.

[26] Felix T. Smith. 'A Symmetric Representation for Three Body Prob-
      lems. I. Motion in a Plane'. In: *Journal of Mathematical Physics* 3.4
      (1962), pp. 735–748. DOI: 10.1063/1.1724275. eprint: https://doi.
      org/10.1063/1.1724275. URL: https://doi.org/10.1063/1.
      1724275.

[27] D. Blume and Chris H. Greene. 'Three particles in an external trap:
      Nature of the complete $J = 0$ spectrum'. In: *Phys. Rev. A* 66 (1 July
      2002), p. 013601. DOI: 10.1103/PhysRevA.66.013601. URL: https:
      //link.aps.org/doi/10.1103/PhysRevA.66.013601.

[28] H. Hellmann. 'Zur Rolle der kinetischen Elektronenenergie für die
      zwischenatomaren Kräfte'. In: *Zeitschrift für Physik* 85.3 (Mar. 1933),
      pp. 180–190. ISSN: 0044-3328. DOI: 10.1007/BF01342053. URL: https:
      //doi.org/10.1007/BF01342053.

[29] R. P. Feynman. 'Forces in Molecules'. In: *Phys. Rev.* 56 (4 Aug. 1939),
      pp. 340–343. DOI: 10.1103/PhysRev.56.340. URL: https://link.
      aps.org/doi/10.1103/PhysRev.56.340.

[30] Cristina Sanz-Sanz et al. 'Non-adiabatic couplings and dynamics in
      proton transfer reactions of Hn+ systems: Application to H2+H2+
      → H+H3+ collisions'. In: *The Journal of Chemical Physics* 143.23
      (2015), p. 234303. DOI: 10.1063/1.4937138. eprint: https://doi.
      org/10.1063/1.4937138. URL: https://doi.org/10.1063/1.
      4937138.

[31] Yujun Wang, Jose P. D' Incao and Brett D. Esry. 'Chapter 1 - Ul-
      tracold Few-Body Systems'. In: *Advances in Atomic, Molecular, and
      Optical Physics*. Ed. by Ennio Arimondo, Paul R. Berman and Chun
      C. Lin. Vol. 62. Advances In Atomic, Molecular, and Optical Physics.
      Academic Press, 2013, pp. 1–115. DOI: https://doi.org/10.1016/
      B978-0-12-408090-4.00001-3. URL: http://www.sciencedirect.
      com/science/article/pii/B9780124080904000013.

[32] *Advances In Atomic, Molecular, and Optical Physics*. URL: https:
      //www.sciencedirect.com/bookseries/advances-in-atomic-
      molecular-and-optical-physics/vol/62/suppl/C.

[33] D. V. Fedorov and A. S. Jensen. 'Efimov effect in coordinate space Faddeev equations'. In: *Phys. Rev. Lett.* 71 (25 Dec. 1993), pp. 4103–4106. DOI: 10.1103/PhysRevLett.71.4103. URL: https://link.aps.org/doi/10.1103/PhysRevLett.71.4103.

[34] B. R. Johnson. 'On hyperspherical coordinates and mapping the internal configurations of a three body system'. In: *The Journal of Chemical Physics* 73.10 (1980), pp. 5051–5058. DOI: 10.1063/1.439983. eprint: https://doi.org/10.1063/1.439983. URL: https://doi.org/10.1063/1.439983.

[35] R. C. Whitten and F. T. Smith. 'Symmetric Representation for Three-Body Problems. II. Motion in Space'. In: *Journal of Mathematical Physics* 9.7 (1968), pp. 1103–1113. DOI: 10.1063/1.1664683. eprint: https://doi.org/10.1063/1.1664683. URL: https://doi.org/10.1063/1.1664683.

[36] H. Suno et al. 'Three-body recombination of cold helium atoms'. In: *Phys. Rev. A* 65 (4 Apr. 2002), p. 042725. DOI: 10.1103/PhysRevA.65.042725. URL: https://link.aps.org/doi/10.1103/PhysRevA.65.042725.

[37] B. D. Esry, Chris H. Greene and H. Suno. 'Threshold laws for three-body recombination'. In: *Phys. Rev. A* 65 (1 Dec. 2001), p. 010705. DOI: 10.1103/PhysRevA.65.010705. URL: https://link.aps.org/doi/10.1103/PhysRevA.65.010705.

[38] Brett Esry. 'MANY-BODY EFFECTS IN BOSE-EINSTEIN CONDENSATES OF DILUTE ATOMIC GASES'. PhD thesis. University of Colorado, 1997.

[39] William H. Press et al. *Numerical Recipes 3rd Edition: The Art of Scientific Computing.* 3rd ed. New York, NY, USA: Cambridge University Press, 2007. ISBN: 0521880688, 9780521880688.

[40] B. D. Esry, Chris H. Greene and James P. Burke. 'Recombination of Three Atoms in the Ultracold Limit'. In: *Phys. Rev. Lett.* 83 (9 Aug. 1999), pp. 1751–1754. DOI: 10.1103/PhysRevLett.83.1751. URL: https://link.aps.org/doi/10.1103/PhysRevLett.83.1751.

[41]   Aron Kuppermann. 'A useful mapping of triatomic potential energy surfaces'. In: *Chemical Physics Letters* 32.2 (1975), pp. 374–375. ISSN: 0009-2614. DOI: `https://doi.org/10.1016/0009-2614(75)85148-7`. URL: `http://www.sciencedirect.com/science/article/pii/0009261475851487`.

[42]   Boris Podolsky. 'Quantum-Mechanically Correct Form of Hamiltonian Function for Conservative Systems'. In: *Physical Review* 32.5 (1928), pp. 812–816. DOI: `10.1103/physrev.32.812`.

[43]   B. R. Johnson. 'The classical dynamics of three particles in hyperspherical coordinates'. In: *The Journal of Chemical Physics* 79.4 (1983), pp. 1906–1915. DOI: `10.1063/1.445969`. eprint: `https://doi.org/10.1063/1.445969`. URL: `https://doi.org/10.1063/1.445969`.

[44]   George B. Arfken, Hans J. Weber and Frank E. Harris. *Mathematical methods for physicists a comprehensive guide*. 7th ed. Elsevier, 2013.

[45]   Herbert Goldstein, Charles Poole and John Safko. *Classical mechanics*. Addison Wesley, 2000. URL: `https://detritus.fundacioace.com/pub/books/Classical_Mechanics_Goldstein_3ed.pdf`.